LARGE VEGETATIVE ROUGHNESS CONTROLS ON AEOLIAN PROCESSES

A Thesis

Presented to

The Faculty of Graduate Studies

of

The University of Guelph

by

JEFFREY L. ORD

In partial fulfilment of requirements

for the degree of

Master of Science

October, 2010

Your file Votre référence
ISBN: 978-0-494-71434-8
Our file Notre référence
ISBN: 978-0-494-71434-8

ABSTRACT

LARGE VEGETATIVE ROUGHNESS CONTROLS

ON AEOLIAN PROCESSES

Jeffrey L. Ord
University of Guelph, 2010

Advisor:
Professor W.G. Nickling

The semi-arid rangelands of southern New Mexico are important areas for active sand movement because of the mesquite-dominated desert ecosystem. Accelerated wind erosion in the mesquite shrublands is attributed to the development of elongated patches of bare soil ("streets") that create a complex distribution of the nabkhas on the surface. Research was undertaken to understand the relationship between surface roughness, wind flow and sediment transport. To understand the effects of wind properties, measurements were taken for near surface wind speed, shear stress and saltation flux. Measurements of near surface wind speed and shear stress were ratioed to regional wind speeds (at 18 m) to make comparisons of wind data between wind directions. Measurements of saltation flux were ratioed to the largest value of flux for comparison purposes. Results show that as winds change direction λ values also change. Lower λ, associated with mesquite streets, show higher near surface wind speeds and sediment movement. Higher λ values show lower near surface wind speeds and reduced sediment movement. Average shear stress values show no significant difference as λ values change; however, detailed inspection of shear stress on a sensor-by-sensor basis show that winds flowing over the roughness with low λ values create more widespread shear stresses. The results suggest that the width of the roughness, orientation and distribution affect the shelter areas in the lee of the roughness, which in turn affect sediment transport.

ACKNOWLEDGMENTS

I would like to thank Dr. W.G. Nickling and Dr. J.A. Gillies for their guidance, support and encouragement throughout my degree. Thank you to Mike Tilson for our countless conversations, your intellectual support and sound perspective. I would also like to thank Dr. G. Drewitt and Dr. J.S. Warland for their enthusiasm, and guidance with technical problem solving.

I am very grateful to those that lent a hand in the many stages of my degree. Specifically, Irgrid Vloet and Ashley St Hilaire for their intellectual support and for a memorable field season. My appreciations are extended to Mario Finoro and Sandy McLaren for their logistical support and lasting kindness.

I am grateful for the financial assistance from an Arthur D. Latornell Travel Scholarship and the N.S.F grant to Dr. J.A. Gillies.

Thank you to my family and friends who provided balance and encouragement, guidance and distraction throughout my degree. I would also like to finally thank Britt for her continual support and patience throughout my degree and research.

CONTENTS

LIST OF FIGURES

LIST OF TABLES

LIST OF SYMBOLS

A_t	element frontal area
A_p	porous frontal area
b	element basal width
C_R	drag coefficient of roughness element
C_S	drag coefficient of surface
d	displacement height
F_c	interparticle cohesive force
F_d	drag force
F_g	gravitational force
F_i	impact force
F_0	aerodynamic lift
h	height; element height
m	surface shearing stress heterogeneity parameter
n	number of roughness elements
R	average shear stress ratio
R''	maximum shear stress ratio
Re	Reynolds number
S	ground area over which roughness elements are distributed
u	mean wind velocity
u_z	horizontal wind velocity at height z
u_*	shear velocity
z	reference height
z_0	roughness length
β	ratio of the drag coefficient of a roughness element to that of the surface
γ	saltation intermittency
κ	von Kármán's constant
λ	roughness density
σ	ratio of the element basal area to frontal area
μ	dynamic viscosity
ρ	fluid density
τ	shear stress
τ_0	total shear stress
τ_0'	threshold shear stress
τ_R	roughness element shear stress
τ_S	surface shear stress
τ_S'	average shear stress on the intervening surface between roughness elements
τ_S''	maximum shear stress on the intervening surface between roughness elements

CHAPTER 1

INTRODUCTION

Sediment transport is an significant driver of landscape change and desertification that can be initiated naturally or anthropogenically from overgrazing, water budget changes, and climate change. Vegetation on the surface is considered 'surface roughness'; surface roughness has the capacity to protect the surface from wind erosion processes by trapping moving sediment in the lee of roughness, covering the surface, and extracting momentum from the air. Research has been undertaken to understand the relationship that surface roughness has with wind flow and sediment movement, with the goal of developing practical applications of land resource management in arid and semi-arid environments to reduce wind erosion. Research by Marshall (1971) established the first dataset on how surface roughness can abate wind erosion processes. The later-developed Raupach et al. (1993) model has acted as a framework to evaluate how effective surface roughness is at reducing wind erosion processes by applying the theory of shear stress partitioning.

The Raupach et al. (1993) model uses shear stress partitioning theory to explain the effectiveness of surface roughness to protect surfaces from wind erosion. This approach divides the stress of the wind into the component of stress that is imparted on the surface and the component of stress that is imparted on the roughness elements. Research by a number of authors (e.g., Musick and Gillette, 1990; Wolfe and Nickling, 1996; Musick et al., 1996; Wyatt and Nickling, 1997; Lancaster and Baas, 1998; Al-Awadhi and Willetts, 1999; Gillies et al., 2000; Okin and Gillette, 2001; Crawley and Nickling, 2003; Gillette and Pitchford, 2004; King et al., 2005; Okin, 2005; King et al., 2006; Gillies et al., 2006, 2007; Brown et al., 2008; Saaliste, 2008) has evaluated the effects of surface roughness on wind erosion processes, and has found general agreement with Raupach et al. (1993) or similar models. Despite this general agreement, there are some uncertainties about

how effective theses models are at predicting the protective role of sparse, heterogeneous distributions of vegetation in natural environments. Some authors (e.g., Okin and Gillette, 2001; Gillette et al., 2006; King et al., 2006) have observed greater stresses at the surface and larger sediment movement in mesquite-vegetated landscapes, which could be explained by limitations in the Raupach et al. (1993) model (Crawley and Nickling, 2003; King et al., 2005; Gillies et al., 2006; Brown et al., 2008; Saaliste, 2008). This recent research has called for more detailed analysis of wind flow and sediment transport through heterogeneously vegetated surfaces.

One example of a vegetative community that experiences sediment transport are mesquite dominated lands in southern New Mexico in the Jornada del Muerto plane near Las Cruces. Mesquite communities develop elongated patches of bare soil that are oriented in the direction of the strongest winds called 'streets' (Gillette et al., 2006). Streets develop in a synergistic relationship between sediment transport, deposition, vegetation structure and, mesquite's competitive growing advantage (Langford, 2000). The mesquite streets are a component of the mesquite nabkhas dune community in the semi-arid rangelands of the U.S. southwest. The dunes are large (2-7 m across and 2 m tall) vegetative sand mounds that are heterogeneously distributed over the surface (Langford, 2000). Despite extensive vegetative cover in the mesquite communities sediment transport (Okin and Gillette, 2001; Gillette et al., 2006; Bowker et al., 2006) and land degradation has been observed by Peters et al. (2006). Most semi-arid landscapes and rangelands are dominated by some type of complex vegetation distribution, particularly in southern New Mexico (Langford, 2000). Complex distributions of surface roughness, such as the mesquite nabkhas communities are not well represented in current wind erosion models. These communities are an important source of dust emissions (Okin, 2005) and are a result of, and contributing to, land degradation (Langford, 2000; Okin, 2005; Peters et al., 2006).

This research is part of a larger study that is investigating the effects of vegetation on sediment transport in semi-arid rangelands with the goal of creating a regional wind erosion model. The larger study aims to investigate a range of vegetative communities in

southern New Mexico ranging from newly colonized areas of rangeland to mature nabkha communities. This research was an empirical based field study to investigate the effects of mesquite community structure on aeolian sediment transport. The aim of this study was to quantify and describe wind flow and sediment transport with respect to the structure (i.e., porosity and flexibility) and distribution of large, complex vegetative roughness elements. To address the aim of the research the following objectives were developed:

1. Calculate what the differences in roughness densities (λ) are based on wind direction.
2. Quantify and describe aeolian processes the near surface wind field at a scaled height throughout the vegetated area.
3. Determine if there are different near surface wind speeds when wind changes direction as a result of the structure and distribution of the mesquite vegetation.
4. Determine if there are different ratioed surface shear stresses, and ratioed sediment fluxes from different wind directions.

To address the aim and objectives, field measurements were made for transport rates, regional and near surface wind speed and direction, surface shear stresses, and key surface aerodynamic parameters of the plant community. These measurements provided data to quantify the aerodynamics and sand transport capacity of the nabkha community.

The proceeding chapters will cover background information that is necessary to understand the large complex surface roughness, the research methods for this study, a presentation of key results, a discussion of results within the context of previous research and conclusions.

CHAPTER 2

AEOLIAN SEDIMENT TRANSPORT AND EFFECTS OF SURFACE ROUGHNESS

Sediment transport is a major driving force for landscape change in arid and semi-arid regions. Understanding the relationship between wind flow and the surface is critical for the predictive capacity of sediment transport models. Wind flowing over the surface creates a shearing stress that can mobilize sand and dust and initiate landscape change. Surface characteristics such as moisture, crusts, and surface roughness affect the interaction of the wind with the surface. The presence of non-erodible roughness elements, such as gravel, rocks, and vegetation, disrupt the wind flow and modulate sediment movement. The effect of surface roughness has been widely investigated (e.g., Marshall, 1971; Raupach et al., 1993; Gillies et al., 2000; Brown et al., 2008) using a shear stress partitioning approach. The shear stress partitioning approach assumes that the stress from the wind can be divided into two components, the stress that is imparted to the surface roughness and the stress that is imparted to the intervening surface. Results from studies using this approach indicate that sediment movement, and hence landscape change, decreases with increasing amounts of roughness. Understanding this relationship is important for wind erosion modelling and semi-arid rangeland management. Because semi-arid rangelands support vegetation, the management of that vegetation could attenuate the effects of desertification processes. Furthermore, a comprehensive understanding of the surface and wind interaction is critical for wind erosion modelling (Fryrear et al., 2001). Wind erosion modelling can help identify areas susceptible to desertification. This chapter outlines the need for understanding wind erosion, and presents information on the interactions between surface roughness and wind.

2.1 The Need for Understanding Sediment Transport

Sediment transport can be a dominant driver of landscape change in arid and semiarid regions, leading to desertification. Desertification is the process by which an arid, semiarid, or sub-humid landscape becomes degraded, making it less productive for human use (UNCCD definition from Véron et al., 2006). Dryland environments cover 40% of the global land surface (Deichmann and Eklundh, 1991) and are populated by approximately a billion people (Reynolds and Stafford-Smith, 2002). Desertification has major implication for humans and the natural environment including loss of biodiversity, spread of invasive species, changes in hydrological budgets, and wind and water erosion (Peters et al., 2006). Wind erosion is a driver of desertification because it moves sediment, particularly soil nutrients on the surface, (Okin and Gillette, 2001) which reduces the capacity of the landscape to sustain vegetation (Okin and Gillette, 2001; Li et al., 2007).

A prime example of desertification is the degradation of natural rangelands, once dominated by grasses, to shrub dominated landscapes. This results in a reduction in the biodiversity and number of species on the landscape. In the semiarid regions of the U.S Southwest sediment transport has been identified as an important component of desertification, which has transformed productive rangeland covered in grasses to a landscape dominated by mesquite nabkhas (Peters et al., 2006). The nabkhas form in a synergistic relationship between vegetation growth and wind and water erosion. As the vegetation in the nabkhas grows it has the capacity to trap more sediment and nutrients around it giving it a competitive advantage over other vegetation and allowing it to penetrate its roots deeper into the soil to capture more water and grow rapidly (Langford, 2000).

In addition to exacerbating desertification, wind erosion is also responsible for dust emissions from land surfaces in arid and semiarid regions (Okin, 2005), which affects human health (Johnson and Graham, 2005; Kuylenstierna et al., 2002). Dust emissions can also affect cloud nucleation (Dentener et al., 1996); iron from surface minerals can play a role in the CO_2 uptake in the ocean (Piketh et al., 2000) and affect downwind nutrient cycling in

soils (Okin et al., 2004). Most natural semi-arid areas have surface roughness on them, such as vegetation. Efforts have focused on modelling sediment transport and dust emissions over these surfaces (Okin, 2005), however some aeolian scholarship (e.g., Okin and Gillette, 2001; Brown et al., 2008; Crawley and Nickling, 2003; King et al., 2005; Okin, 2005) argues that the relationship between vegetated surfaces and wind flow is not well quantified because of plant aerodynamic properties and vegetation distribution effects.

Given the size of arid and semiarid regions and the scale at which humans interact with these environments it is imperative that managers and policy makers have the necessary information to understand desertification and its processes, including wind erosion and sediment transport throughout vegetation.

2.2 The Boundary Layer

Wind flowing over the surface of the earth is affected by the surface creating a zone of airflow called the boundary layer (Oke, 1987). On a planetary scale the boundary layer can be 1-2 kilometres thick, although aeolian geomorphology is interested in the bottom 10 percent. Over a flat surface the boundary layer can be visualized by a vertical wind speed profile as seen Fig. 2.1A. Under the ideal flow conditions the logarithmic wind speed profile can be described by the Prandtl-von-Kármán equation:

$$\frac{u_z}{u_*} = \frac{1}{\kappa} ln\left(\frac{z}{Z_0}\right) , \tag{2.1}$$

where u_z is wind velocity at height z, κ is the von Kármán constant equal to 0.4, u_* is the shear velocity, and Z_0 is the roughness length. The term u_* is a surrogate for the shear stress, τ, which is the streamwise momentum that is imparted on the surface by the wind. This is the force that drives sediment movement and entrainment. The term Z_0 is a measure of the magnitude of the aerodynamic drag on the surface (King et al., 2005). The Prandtl-von-Kármán equation is used to determine shear stress on a surface by way of the u_* term; however, this value is just an estimate of what the shear on the surface is. The u_* term is a product of the interpolated stress that the logarithmic portion of the velocity profile

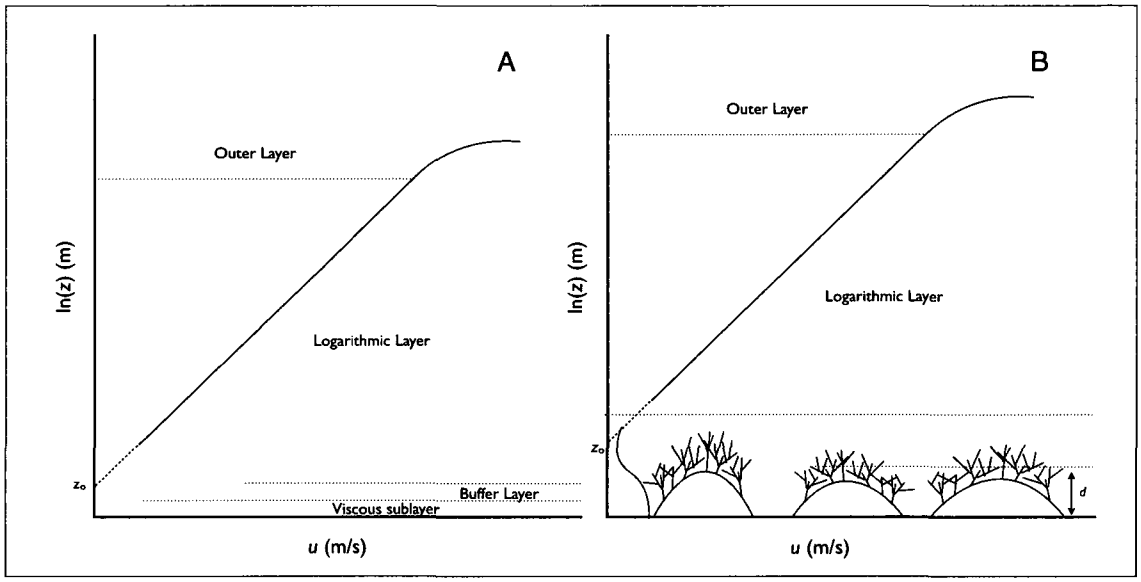

Figure 2.1 Idealized mean velocity profiles over smooth and rough surfaces.

is imparting on the surface. In natural settings the areas under the logarithmic portion of the velocity profile are dominated by flow perturbations and hence, are difficult to define and measure thereby making measurements of shear stress this way questionable (Walker, 2005).

Under most flow conditions the surface has some type of roughness on it such as vegetation, rocks or buildings. Figure 2.1B shows the boundary layer velocity profile over a rough surface with mesquite nabkhas on it. This velocity profile can be described by two separate layers of wind flow, the internal sublayer and the roughness sublayer. The internal sublayer is described by the logarithmic portion of the profile; however, this portion is displaced upwards by the surface roughness. To account for this the Prandtl-von-Kármán equation has the addition of the d term, representing the upward displacement by the mean momentum sink (Wolfe and Nickling, 1993; Dong et al., 2001). The modified Prandtl-von-Kármán equation takes the form:

$$\frac{u_z}{u_*} = \frac{1}{\kappa} ln\left(\frac{z-d}{Z_0}\right), \tag{2.2}$$

where Z_0 represents the roughness length imposed by the roughness elements. Both Z_0 and

d vary as a function of the spacing, height, and shape of the roughness elements and wind direction speed (Wolfe and Nickling, 1993) . In practice the value of Z_0 should be greater over a rough surface, however if a surface is sufficiently sparse it may not be (King et al., 2005).

In Fig. 2.1B the layer of air adjacent to the surface is completely influenced by the surface roughness elements. Roughness interacts with the mean flow extracting momentum from it and creating turbulent wakes behind individual roughness elements (Wolfe and Nickling, 1993). If the surface roughness is sufficiently dense then the roughness sublayer may have spatially uniform flow characteristics, but if there is great surface roughness heterogeneity then there may also be heterogeneity in the surface shear stresses, creating points of shear stress greater than on surfaces with homogeneous distributions of roughness (Crawley and Nickling, 2003).

The spacing, height, width, shape and distribution (or arrangement) of the surface roughness create different types of flow regimes (Morris, 1955; Lee and Soliman, 1977). A single roughness element inserted into flow (Fig. 2.2) will create a wake region that develops downwind of the element; this wake region is dominated by turbulence, and wind speeds are sufficiently less than the mean wind flow, therefore creating an area of protection behind the element. To the side of the the object, flow is accelerated around it creating horseshoe vortices (Raupach et al., 1980; Wolfe and Nickling, 1993).

There are different types of flow regimes that develop as a function of increasing roughness densities. Roughness density, λ is a dimensionless representation of the surface roughness described by:

$$\lambda = \frac{nbh}{S} , \tag{2.3}$$

where n is the number of roughness elements on the surface, b is the average width of the elements, h is average height of the element and S is the total surface area the elements occupy. Fig. 2.3 illustrates the three types of flow regimes and the effects of increasing λ on Z_0. As λ increases there is a sharp increase in Z_0 through isolated roughness flow and wake

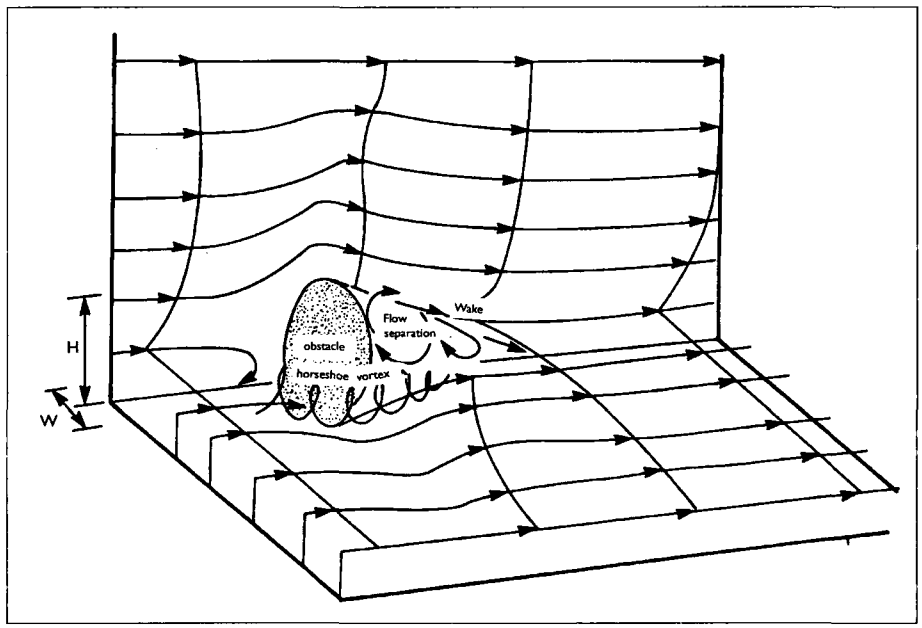

Figure 2.2 Flow visualization around a solid roughness element from Wolfe and Nickling (1993).

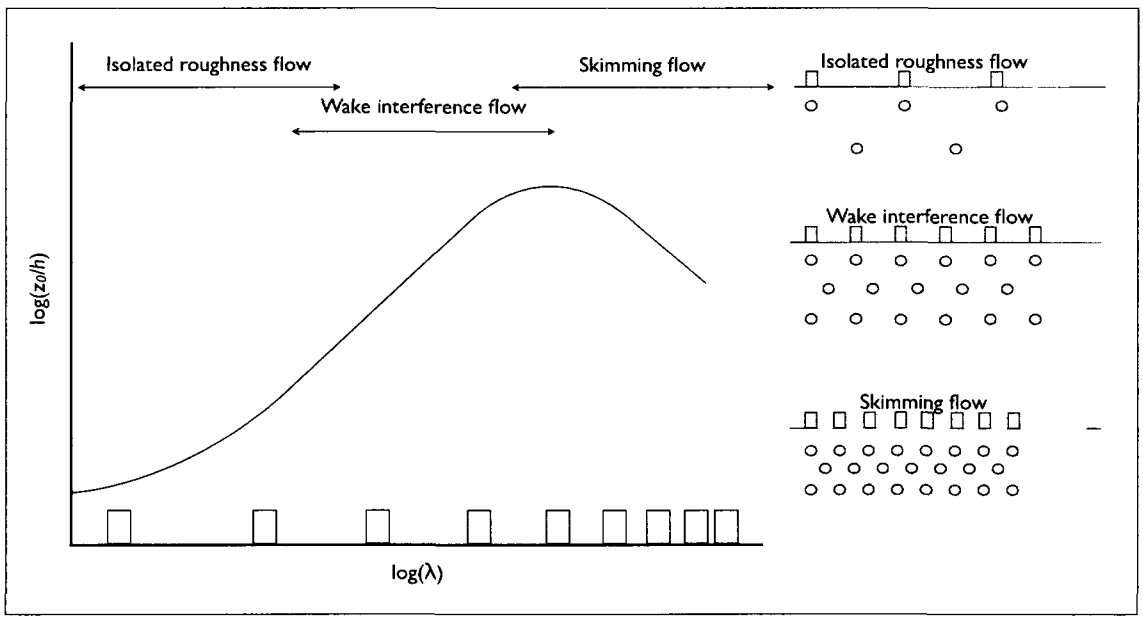

Figure 2.3 Flow regimes through roughness elements and the theoretical wake regions Wolfe and Nickling (1993).

interference flow until λ is high enough to create skimming flow, where Z_0 starts to decrease (Jia et al., 1998). This relationship is a result of the different sheltering associated with the different flow regimes. In Fig. 2.3 the light grey areas behind the elements are a schematic representation of the wake regions that provide sheltering to the surface. Isolated roughness flow is when the wake region is able to develop behind the individual roughness elements on a surface and shearing forces from the wind are able to reach the surface between the wakes. Wake interference flow is when the wake regions of elements upwind are disrupted by downwind elements, and in this case there is more flow disruption and greater sheltering of the surface by the wake regions. Skimming flow occurs when the wake region behind an object is not able to develop and the surface has a major reduction in shear stresses from the development of an internal sublayer. In the last case, flow is skimming along the top of the roughness elements resulting in decreased momentum transfer from the internal sublayer to the surface (Wolfe and Nickling, 1993; Jia et al., 1998; King et al., 2005). The effects of surface roughness are covered in more detail in section 2.4.5.

2.3 Fluid Forces

Surface shear stress τ_0 is the streamwise force imparted on the surface by the wind and it is responsible for sediment movement if it's of sufficient strength (Bagnold, 1941). τ_0 is defined by:

$$\tau_0 = \rho u_*^2 \,, \tag{2.4}$$

where ρ is the air density ($\mathrm{kg \cdot m^{-3}}$), and u_*^2 ($\mathrm{m^2 \cdot s^{-2}}$) is the shear velocity. τ_0 is difficult to measure directly so u_* is used as a surrogate, which is often measured from the law-of-the-wall. u_* can then be calculated from the slope of the log-linear portion of the boundary layer from the law-of-the-wall (Eq. 2.2). τ_0 then can be calculated using Eq. 2.4.

Threshold shear stress, τ_0' occurs when τ_0 reaches a critical level and particle entrainment occurs. Threshold is defined when the shear and lift forces exceed the retarding forces of the particles on the surface (Zhen-shan et al., 2008). The forces acting on a particle include

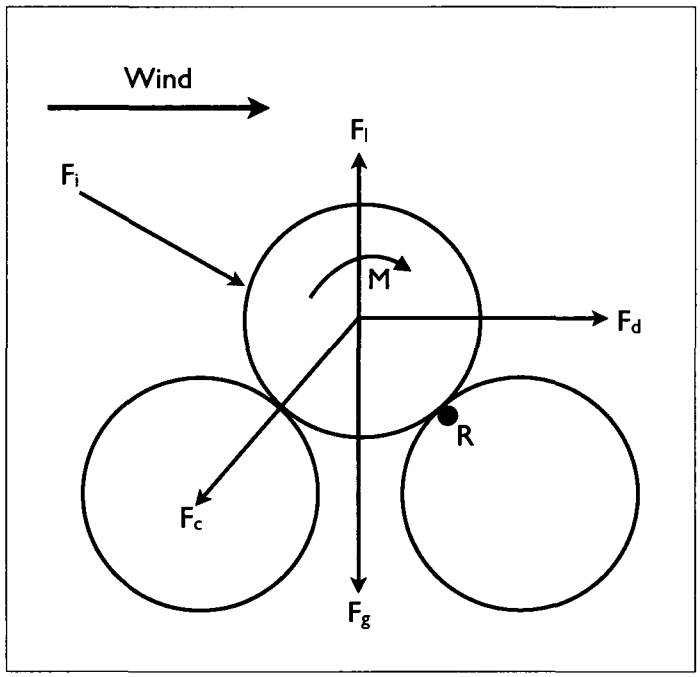

Figure 2.4 Particle force system at threshold of motion, adapted from Iversen et al. (1987).

the aerodynamic lift (F_0) and drag (F_d) forces, aerodynamic movement (force accounting for a center of pressure location difference from the center of the sphere) (M), gravity (F_g), inter-particle cohesive forces (F_c), and impact forces (F_i) from other moving particles. All of these forces move around the point R, as shown in Fig. 2.4 (Iversen et al., 1987).

Bagnold (1941) suggests that τ_0' is associated with a finite u_* that will initiate sediment movement. Nickling (1988) conducted extensive wind tunnel tests examining the initiation of movement for particles of varying sizes and shapes. Nickling (1988) concluded that the threshold should be defined by a range of shear velocities rather then a finite value and that there is a random component to the movement of the first grains on the surface. Similarly, Raupach et al. (1993) argues that threshold shear stress should be represented by the maximum shear stress (τ_0'') on the surface at any instant, rather than a time-averaged shear stress (τ_0'). Zhen-shan et al. (2008), in agreement with Nickling (1988), created a stochastic model to represent the initial movement of spherical grains, and argued that the

threshold shear stress is better expressed as a probability distribution based on statistical analysis. The idea is that that there are fluctuations in the forces of the wind acting near the surface that make threshold shear stress and the initial particle motions random; this is well reasoned by Raupach et al. (1993). The threshold for sediment movement varies in time and over space making it difficult to predict. Adding to these complexities there are a number of other factors that can affect the τ_0' such as the presence of saltation (Bagnold, 1941), development of surface crusts (Rice and McEwan, 2001), presence of moisture Davidson-Arnott et al. (2008), lag surfaces (Nickling and McKenna Neuman, 1995), and surface roughness (Raupach et al., 1993).

2.4 Sediment Transport in the Natural Environment

Reviewing Fig. 2.4 there are a number of forces acting on a particle, such as lift and drag forces, inter-particle cohesive forces and impact forces that all affect the τ_0'. The threshold of sediment movement decreases when there is saltation because of the impact of grains ejecting others off the surface (Bagnold, 1941). Inter-particle cohesive forces increase the u_{*t} and can result from electrostatic forces, van der Waal forces, surface crusts and moisture (Iversen et al., 1987; Rice and McEwan, 2001). The presence of lag surfaces and surface roughness can also increase the τ_0' of a surface because they extract momentum from the air that would otherwise be imparted on the surface (Gillette et al., 1982; Raupach, 1992).

2.4.1 Saltation

Saltation is the movement of sand hopping over the surface resulting from strong winds. Saltating grains create a positive feedback with impacts on the surface ejecting more particles into saltation, causing an increase in sediment flux (Bagnold, 1941). Fig. 2.4 displays the impact driving force of grains on an individual particle, by the arrow labelled F_i. Saltation is initiated when u_{*t} of the surface is met, and sediment movement begins. Once saltation is occurring the u_{*t} is lower because impacting grains on the surface eject more into saltation, this is termed impact threshold for u_{*t} (Bagnold, 1941; Chepil, 1959).

The presence of a saltation cloud near the surface extracts momentum from the lower boundary layer, increasing u_* and Z_0 (Bagnold, 1941; McEwen, 1993). This can be described by the Owen effect, where the ratio of u_* to mean u over a saltating cloud increases (Gillette, 1997). Wind speeds near the surface are dampened by the movement of the grains; however, there is an increase in sediment flux downwind because of this effect (Gillette et al., 1996). The increase in Z_0 means that the surface drag coefficient is larger and the wind profile behaves as if it was flowing over a rougher surface.

2.4.2 Crusts

The potential for sediment transport can be decreased by the presence of physical and biological bonding agents that create surface crusts. Crusts create cohesion of the surface particles, making it less susceptible to sediment transport and increase the τ_0' (Nickling and Ecclestone, 1981). Physical (or mineral) crusts form as moisture evaporates from soil or sediment typically with the presence of sodium salts or calcium carbonate (Gillette et al., 1982). Biological crusts are common in arid environments and can form as a result of fungal growth or organic secretions that act to cement particles together (McKenna Neuman and Maxwell, 1999). Rice and McEwan (2001) argue that the stage of crust development as well as soil moisture can have varying effects on τ_0' reduction.

2.4.3 Moisture

Soil moisture near the surface has been shown to decrease sediment transport and increasing τ_0' (Logie, 1982; McKenna Neuman and Nickling, 1989; Dong et al., 2002). Moisture in the soil has capillary forces that act to bond particles together, therefore increasing the strength of the surface. In wind tunnel tests McKenna Neuman and Nickling (1989) showed that increasing soil moisture by 4-6 per cent required an increase in wind speed to initiate sediment movement. Further increases of 8-10 per cent will fully stop sediment transport (McKenna Neuman and Nickling, 1989). Davidson-Arnott et al. (2008) argue that wind tunnel tests have homogeneous moisture conditions and do not account for the complex spatial

patterns of moisture found in field conditions. In the field, moisture effects can change spatially and temporally therefore the threshold for sediment movement also changes.

2.4.4 Lag Surfaces

Lag surfaces are somewhat similar to surface crusts because they create a layer of sediment on the surface that increases the τ_0'. Lag surfaces develop in areas composed of normally graded sand as well as a smaller portion of immovable sediment such as gravel. Through time the smaller sands are removed by wind erosion leaving behind the larger gravel. This is a deflation lag surface (Nickling and McKenna Neuman, 1995). Depending on the size, shape and concentration of lag elements on the surface there are different effects on wind erosion and sediment transport. Generally, lag surfaces act to protect the surface by absorbing momentum that would otherwise be imparted on transportable particles. Lag surfaces decrease the τ_0', increase Z_0 and therefore tend to decrease saltation and sediment transport (Nickling and McKenna Neuman, 1995). In series of wind tunnel tests McKenna Neuman (1998) concluded that on lag surfaces most of the movement of sand particles is a result of impacting sand grains ejecting sediment into flow and not the effects of τ_0'.

2.4.5 Surface Roughness

Surface roughness is a function of the amount and distribution of non-erodible elements on the surface that affect the wind flow. Surface roughness can affect sediment movement in three ways: it covers part of the surface, extracts momentum from the air, and traps soil particles in the lee of the object.

An object extracts momentum from the air because of the drag that it imparts on the moving air. Momentum is extracted from the moving air as it encounters the roughness. The roughness drag coefficient, C_R, quantifies the degree to which a surface roughness element extracts force from the wind. The drag coefficient can be defined as:

$$C_R = \frac{F}{\rho A_t u_z^2} , \tag{2.5}$$

where F is the total force on the element (N), ρ is air density (kg· m^{-3}), A_t is element frontal area (m^2), and u_z is the wind speed (m· s^{-1}) at height z (m). Element drag is dynamic and is dependent on the shape and size of the object (Taylor, 1988; Wyatt and Nickling, 1997), wind speed and direction (Okin, 2008), and Reynolds numbers (Marshall, 1971; Taylor, 1988; Gillies et al., 2002). Drag coefficients from a number of studies are presented in Table 2.1, where the variability of roughness drag is obviously displayed. Raupach (1992) suggested a value of 0.6 for the C_R of a porous plant; however, experimentation has demonstrated these values to be much lower (Table 2.1).

Drag from vegetation is larger than that of solid objects. The porosity and flexibility of the plant allow for greater momentum extraction from the air. Flexibility in the structure of the plant allows for energy to dissipate in the bending of vegetation. Dissipation of energy may also occur with the development of turbulent structures in plant branches. The larger the C_R the greater ability for momentum extraction and hence decreases in surface shear stress. Gillies et al. (2002) reported a range of values for drag coefficients of different species of plants, they demonstrated that plant drag has dependence on optical porosity. Optical porosity is calculated as a ratio of the total porous area on a roughness object over the total frontal area of a plant:

$$OP = \frac{(A_p)}{(A_t) + (A_p)}, \tag{2.6}$$

where A_p is the total pore area and A_t is the total frontal area of the solid plant.

Surface roughness can protect the surface by cover part of the erodible area and by extracting momentum from the air. The third way that surface roughness protects the surface from shear stresses is in the shelter area behind an object. Section 2.2 outlined the wake effects that develop as air encounters surface roughness, which is visually represented in Figs. 2.2 and 2.3. Okin (2008) argues that under ideal conditions with the presence of a single roughness element the wake region creates a zone of low τ_0 in the immediate lee of the object. As distance increases downwind from the object τ_0 increases until the wake dissipates and flow resumes to what it was before it encountered the object. Conceptually

Table 2.1 Reported C_R values for varying types of roughness

Author	Object	C_R
Taylor (1988)	solid cylinder	0.19
-	solid sphere	0.30
-	solid cube	0.40
Wyatt and Nickling (1997)	creosote shrub	0.485
Grant and Nickling (1998)	porous artificial tree	0.400
Gillies et al. (2000)	small greasewood (0.6 by 0.5 m)	1.425±0.103
-	large greasewood (1.6 by 1.3m)	0.435±0.200
Gillies et al. (2002)	Burning Bush	0.420±0.030
-	Colorado Spruce	0.390±0.040
-	Fountian Grass	0.340±0.060

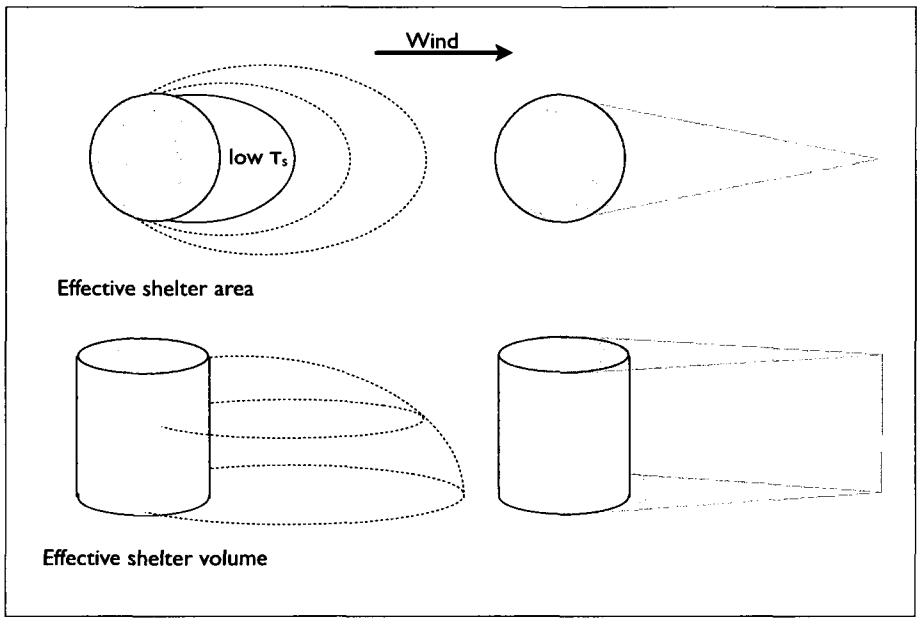

Figure 2.5 Effective shelter area and volume as conceptualized by Raupach (1992). The left of the figure represents real shelter area and volume. The right of the figure demonstrates the modelled area and volume.

the wake region is represented by a wedge-shaped zone, based on contours of τ_0 produced by the interaction of the object with fluid flow; this region is called the effective shelter area (Raupach, 1992). Fig. 2.5 displays the shelter area as conceived by Raupach (1992) and volume behind a cylindrical roughness element. For modelling purposes it is assumed that in the effective shelter area $\tau_s = 0$. The effective shelter area of a roughness object can serve as a region of sediment deposition and no sediment transport, hence the presence of roughness on a surface can abate sediment movement, particularly if the λ is great enough to produce wake interference flow or skimming flow (Wolfe and Nickling, 1993). Logie (1982) found that although surface roughness can protect the surface, if it is sparse enough (i.e., isolated roughness flow) flow acceleration around the objects, (Fig. 2.2) can create horseshoe vortices that can localize shear and initiate sediment movement, hence enhancing sediment transport.

2.5 Surface Roughness Experimentation

The effects of surface roughness on τ_0 are complex, with the development of turbulent wake regions that can both increase or decrease τ_0 depending on its size, spacing, distribution, and type of roughness. Many experiments have been conducted to better understand the role that roughness plays on the surface.

Schlichting (1936) developed the shear stress partitioning approach as a method to determine the protective role that surface roughness has on the surface, which he describes as:

$$\tau_0 = \tau_R + \tau_S \ , \tag{2.7}$$

where τ_0 is the total shear stress acting on an area, τ_R is the portion of the shear stress that is acting on the roughness elements over the area, and τ_S is the shear stress that is acting on the intervening surface between the roughness elements.

Marshall (1971) conducted a series of comprehensive shear stress partitioning experiments in a wind tunnel using varying sizes, shapes and distributions of roughness on the

surface. Major findings from this research indicated that as λ approaches zero the drag on an element in an array will approach the drag that is felt on an individual roughness element standing alone. Additionally, as λ increases there is a decrease in the τ_S, and if element spacing is very close there is a decrease in the drag on individual elements in the array of roughness. Therefore there are shelter effects that occur when elements are in close proximity to each other. Another important finding of Marshall (1971)'s work was that roughness configuration on the surface (including random distributions) produced no significant difference in the protective role of roughness for any given λ. This indicated that in a shear stress partitioning relationship τ_S is dependent upon λ and has little dependancy on spacing shape and arrangement of the roughness. This contradicts more recent work in natural settings suggesting that roughness shape, arrangement and size all have effects on surface protection (Gillies et al., 2000; Okin and Gillette, 2001; Gillies et al., 2002; Gillette and Pitchford, 2004).

Musick and Gillette (1990) carried out shear stress partitioning experiment in the field measuring average surface shear stress, $\tau_0^{'}$, in the presence of vegetation using vertical wind profiles and a saltation probe for detecting impacts of sand grains. They calculated field threshold shear stress measurements and compared them to threshold shear stresses determined for the same soils in a wind tunnel. A critical finding of their work was that sediment transport was occurring at λ values predicted by Marshall (1971) for which no sediment movement should occur. This suggests that the fraction of shear stress acting on the intervening surface was large enough to cause erosion at natural wind speeds when Marshall (1971) predicted that they would not.

In 1992, Raupach developed a model that used the superimposition of effective shelter area (see Fig. 2.5) to describe the protective role of surface roughness on sediment transport. The model uses a ratio of the threshold velocity for a bare surface to the threshold velocity of that same surface with the roughness on it. The model includes measurable parameters describing the size and spacing aerodynamic properties of roughness. Raupach et al. (1993)

revised the Raupach (1992) model to this form:

$$R_t = \left(\frac{\tau_S''}{\tau}\right)^{1/2} = \left[\frac{1}{(1 - m\sigma\lambda)(1 + m\beta\lambda)}\right]^{1/2}, \tag{2.8}$$

where τ_S'' is the maximum surface shear stress over the area in question, σ is the ratio of basal area to frontal area, λ is roughness density and β is the ratio of drag coefficients for the roughness elements (C_R) to the surface (C_S) expressed by:

$$\beta = \frac{C_R}{C_S} \tag{2.9}$$

Equation 2.8 includes the m parameter that represents the surface surface shear stress heterogeneity. Mulhern and Finnigan (1978) found great τ_S heterogeneity in a wind tunnel investigation of wind flow and τ_0 over a distribution of random roughness elements. Raupach et al. (1993) realized that this spatial heterogeneity of surface shear stress must be accounted for in the model, citing that non-uniform erosion patterns around roughness elements indicates inhomogeneity in the τ_S in the streamwise velocity field throughout roughness elements. The inclusion of the m parameter required the empirical assumption the τ_S'' is equivalent to the τ_S' of a surface with a lower λ such that:

$$\tau_S''(\lambda) = \tau_S'(m\lambda) , \tag{2.10}$$

where τ_S'' is the maximum surface shear stress throughout the roughness, and τ_S' is the average surface shear stress. The m parameter varies between 0 and 1 and scales the maximum shear stress to the average shear stress acting on the surface with a lower λ.

Wolfe and Nickling (1996) studied shear stress partitioning in the field when wind speeds are below transport threshold. Results of Wolfe and Nickling (1996) agree with Musick and Gillette (1990) and the model of Raupach et al. (1993), but indicate that shear stress ratios vary with wind speeds, and that shear stress can vary spatially and temporally through vegetative communities. Wolfe and Nickling (1996) also indicate that at high λ, increased wake interactions increase the drag coefficient on vegetation at low wind speeds and underestimate threshold shear velocity ratios.

Musick et al. (1996) examined the relationship between sediment transport threshold and varying parameters of roughness elements, including porosity, element aspect ratio (height/diameter), and λ in a wind tunnel study. Results from their study indicate that increases in λ increase the saltation threshold and are also described well by the Raupach et al. (1993) shear stress partitioning model. Musick et al. (1996) indicate that low-porosity elements are $\approx$ 50 % more effective at increasing saltation threshold than solid roughness elements, or elements with high-porosity. Their results also indicate that as element aspect ratio increases there is an increase in saltation threshold. Musick et al. (1996) stress that the most important finding of their research is that vegetation structure strongly influences aeolian sediment transport; however, current methods of describing vegetation are inadequate and fail to characterize aspects of plant structure that could be critical for understanding aeolian processes.

Wyatt and Nickling (1997) measured the shear stress partitioning relationship on creosote vegetated surfaces with varying λ. Measurements of drag were made on creosote vegetation and were determined to be greater than solid roughness elements of similar size. The results from this study agree with the Raupach et al. (1993) model; however, the computed value of m was 0.16, which is much lower then suggested by Raupach et al. (1993), or the calculated values ranging from 0.50 - 0.60 reported by Musick and Gillette (1990) and Musick et al. (1996).

Lancaster and Baas (1998) conducted a field study to determine the effects that saltgrass communities have on τ'_S. Measurements of vertical wind profiles and saltation flux using BSNE (Big Spring Number Eight)(see Fryrear, 1986) traps were taken over four different λs. Results indicate that as λ increases there is a decrease in τ_0' and exponential decrease in sediment flux with the potential for sediment transport to be eliminated at 15 % surface cover ($\lambda \approx 0.01$). The values of the shear stress ratio, R, are higher than predicted by Raupach et al. (1993) and higher than values reported from Musick and Gillette (1990) and Wolfe and Nickling (1996) with similar λ. Results of this study lie within the range of the shear stress ratio predicted by Musick et al. (1996) for porous roughness elements.

This supports the result of Musick et al. (1996) that found the Raupach et al. (1993) model over-estimates the effects of vegetation on protecting natural surfaces.

Al-Awadhi and Willetts (1999) conducted a wind tunnel experiment to examine how roughness affects sediment transport. Results from this study observed that sediment transport occurred up to $\lambda = 0.369$. Marshall (1971) suggested that surface roughness may provide adequate protection to stop sediment transport at $\lambda = 0.03$. Their results found agreement in deposition patterns of sediment and also agree with shape of shelter areas in the lee of roughness elements (Wolfe and Nickling, 1993; Raupach, 1992); however, sediment transport did not stop at unexpectedly high λs.

Gillies et al. (2000) measured drag on greasewood plants in an open field with a force balance and determined that the drag on the plants was much greater than drag exerted on solid roughness elements of the same size. The effectiveness of greasewood for surface protection was then assessed using varying drag coefficients for different surfaces with the Raupach et al. (1993) model, with values of m assumed to be 0.5. Results suggest that 3 to 6 % cover, or $\lambda \approx 0.032 - 0.06$ would be effective to reduce shear stress so that no sediment transport would occur. Gillies et al. (2000) assert that such low λ values can result in complete surface protection because of the very high drag coefficients measured for the vegetation. These values are much lower than Musick and Gillette (1990) who estimate the critical λ should be 0.13, or 15 % cover suggested by Lancaster and Baas (1998).

In a wind tunnel study Crawley and Nickling (2003) found a consistent proportional relationship between τ''_S and τ'_S. Crawley and Nickling (2003) found that values of m are much higher in studies with solid roughness than observed in Wyatt and Nickling (1997), which suggests that sparse vegetation arrays have values of τ''_S exceeding τ'_S at much greater proportions than solid roughness arrays (Crawley and Nickling, 2003). This means that flow and vegetation interaction create higher variations of shear, potentially leading to greater sediment transport.

In naturally vegetated rangelands some arrangements and types of vegetation on the surface have demonstrated significant variations in sediment transport (Gillette and Pitch-

ford, 2004). Measurements of sand flux within different vegetation communities by Gillette and Pitchford (2004) demonstrated that areas of mesquite coppice dunes had higher erosion rates than other vegetation types with similar λ values. The higher rates of flux could be a result of a larger than expected variation in shear stress over the surface. Okin and Gillette (2001) identified that mesquite-dominated landscapes are characterized by a heterogeneous arrangement of vegetation on the surface with elongated areas of bare soil, termed 'streets'. The streets form as a result of a synergistic relationship between sediment transport in the dominant wind direction, sediment deposition and vegetation structure. The street formations have been used to partially explain the discrepancies between observed and predicted wind erosion rates (Okin and Gillette, 2001). In a comprehensive examination of all the shear stress partitioning data available King et al. (2005) conclude that the Raupach et al. (1993) model has excellent agreement with wind tunnel studies, but is "less favourable" for modelling the field environment. Okin (2005) argues that sediment transport is a stochastic process and the Raupach et al. (1993) model relies on average values of u_{*ts}, C, R, β to predict the protective role of vegetation; however, these values are not useful for determining sediment transport rates in places such as mesquite streets because erosion is only happening in specific locations and not over the entire surface.

In a mesquite-dominated landscape King et al. (2006) made shear stress partitioning measurements of in-situ surface shear stress with Irwin sensors, and surface shear stress over the entire surface with a vertical array of anemometers. They found a directional dependency of Z_0 with the wind direction and that the lowest values of Z_0 are associated with the dominant wind direction and the alignment of the mesquite streets. This indicates that more shear stress from the momentum generated in the logarithmic portion of the boundary layer profile acts on the surface when winds are aligned with streets. Measurements of shear stress also showed positive skewness as fetch distance increased along the 'streets' suggesting that there is greater potential for sediment transport processes in these areas. The relationship between Z_0 and wind direction was not observed for immature mesquite communities with a homogeneous distribution of roughness, and shear stress distributions

were not skewed. Surface shear stress measurements from King et al. (2006) were twice as high as those measured in the wind tunnel (Crawley and Nickling, 2003) with comparable λ values and this was attributed to the structure and distribution of vegetation on the surface. Stout and Zobeck (1997) conceptualize sediment movement as a function of maximum shear stress that initiate and drive the system, not averages. The results of King et al. (2006) demonstrate that the streets in the nabkhas consistently have higher than average shear stresses. Coupling the results of King et al. (2006) and the Stout and Zobeck (1997) conceptualization it could be hypothesized that greater sediment transport will be occurring in these areas. Gillette et al. (2006) have identified these areas as having greater sediment transport than areas on the same surface that are more protected.

Gillies et al. (2006) found that the larger sized roughness in the field setting was much more efficient at trapping sediment movement than smaller sized roughness in a wind tunnel setting. Results from Gillies et al. (2007) support the notion that wake effects from elements interact and roughness elements downwind will have less drag on them than upwind elements. The implication of this is that the downwind surface is also protected, therefore reducing sediment transport.

Brown et al. (2008) conducted wind tunnel experiments with different arrangements of surface roughness, measuring surface shear stress, drag and wind conditions. Results indicated that surface roughness protection is independent of the arrangement of the surface roughness, which is similar to the finding of Marshall (1971). That is, measurements of average and maximum surface shear stress indicate that there is no significant difference between homogeneous and heterogeneous (including streets) distributions of roughness. Raupach et al. (2006) examined the relationship between Z_0 and λ on varying arrangements of roughness in the wind tunnel, and found that there is no significant difference in this relationship between Z_0 and λ over hetero and homogeneous surfaces. What can be inferred from these results is that the distribution of surface shear stress may also not be affected by changes in the arrangement of λ on a surface, which is substantiated by the results of Brown et al. (2008). The results of Raupach et al. (2006) are contrary to results of King et al.

(2006) who found that as wind direction changed the Z_0 also changed. However, the values of λ in Raupach et al. (2006) did not change, but the values of λ in King et al. (2006) were directionally dependent. The arrangement of roughness on the surface is different relative to how the wind is encountering it, but the λ remained the same. Despite the results of Raupach et al. (2006) and Brown et al. (2008), field studies have demonstrated that roughness arrangement has an effect on sediment flux (Gillette et al., 2006; Okin et al., 2004). However, there is little understanding about the relationship between surface roughness arrangement and actual sediment entrainment, transport and deposition. These obvious discrepancies between the laboratory and field setting expose that there may be a scaling problem of modelling and measuring the effects of surface roughness in wind tunnels.

Saaliste (2008) made comprehensive measurements of shear stress throughout varying arrangements and λ's of solid roughness and it was found that values of skewness and variation can be used to identify areas of sediment transport potential over complex surfaces (Saaliste, 2008). Saaliste (2008) also found that at lower λ's clumps of roughness acted as single roughness elements with varying wake effects and that with this arrangement of surface roughness multiple flow regimes existed over the heterogeneous surface. Given this information, values of shear stress (King et al., 2006), and sediment flux (Gillette et al., 2006; Okin et al., 2004) over areas of heterogeneous vegetative roughness (e.g., mesquite nabkhas dunes and 'streets'), it could be suggested that these areas are experiencing skimming flow over vegetation, sheltering each other, and simultaneously experiencing isolated roughness flow in and around the 'streets', which could be driving the sediment transport over these areas with high values of λ otherwise predicted to completely protect the surface from sediment transport.

A number of conclusions can be drawn from the work that has been reviewed above:

1. Surface roughness will decrease sediment movement by protecting the surface.

2. Wake regions in the lee of surface roughness are areas of the highest protection.

3. The Raupach et al. (1993) model describes the effects of shear stress partitioning very

well in wind tunnel testing and less so when used under natural settings in the field. However, adjustments can be made to the m and β parameters, through estimation, that make the model fit under all conditions.

4. Drag coefficients for porous roughness elements such as natural vegetation vary but are generally higher than drag coefficients for solid roughness elements of the same size. This means that vegetation would be better at abating the effects of wind on the surface than other solid roughness elements.

5. Distribution of roughness on the surface is important in field settings, particularly in the presence of mesquite 'streets'. Random or clumped distributions in laboratory settings have proven to be less important to the distribution of surface shear stress and sediment movement than in the field.

6. Modelling of sediment transport processes in natural settings is complex; however, it is necessary to better understand dust emissions, desertification and ecological changes.

2.6 Conclusions

The region of windflow directly adjacent to the Earth's surface will impart momentum on the surface, which can result in sediment movement. Understanding how wind imparts momentum on the surface is imperative for understanding landscape change in arid and semi-arid environments. Extensive experimentation and modelling have been used to try to understand the wind's interaction with the surface, particularly when surface roughness is present. Surface roughness can reduce sediment transport; however, the processes involved are not completely understood. Wind tunnel studies of roughness have clear and consistent results. These results do not translate perfectly to natural environments, particularly in areas dominated by heterogeneous distributions of vegetation. A number of authors have called for more detailed experimentation in vegetative rangelands (Musick et al., 1996; Okin and Gillette, 2001; Okin, 2005; King et al., 2006; Brown et al., 2008; Saaliste, 2008)

CHAPTER 3

RESEARCH METHODS

A field study was undertaken to measure wind flow through a complex, heterogeneous distribution of mesquite nabkhas examining the relationship between surface shear stress, wind flow dynamics, and sediment transport in these environments. This investigation is part of a larger study with the overall goal of creating a regional wind erosion model for the complex semi-arid rangeland landscape of southern New Mexico. To satisfy the specific goals of this study, outlined in Chapter 1, and contribute to the development of the regional wind erosion model measurements were made of near surface wind speeds and direction, regional wind speeds and direction, surface shear stress, saltation flux, and vegetative parameters. Data collection was carried out in the spring of 2009 at the U.S. Department of Agriculture Jornada Experimental Range(USDA-JER) near Las Cruces, New Mexico. Early spring was chosen for the experiment because this coincides with the windiest times of the year (Okin and Gillette, 2001). During the study period 13 sediment transport events were observed.

3.1 Study Area and Site Selection

A mature mesquite nabkha site, which is representative of the nabkha dunes in this region, was chosen as the study location (at 106°43'11.546W 32°41'3.784N) because it is a large heterogeneous distribution of complex roughness. The dunes at the site vary in size from 1 to 3 m in height. Figure 3.1 is an aerial view of the vegetation cover on this surface. In Fig 3.1A the arrow is pointing from the southwest to the northeast demonstrating the presence of 'streets' at the site. Figure 3.1B is the view to the south of the site. The truck in the image provides scale to the largest sized nabkhas in the study area.

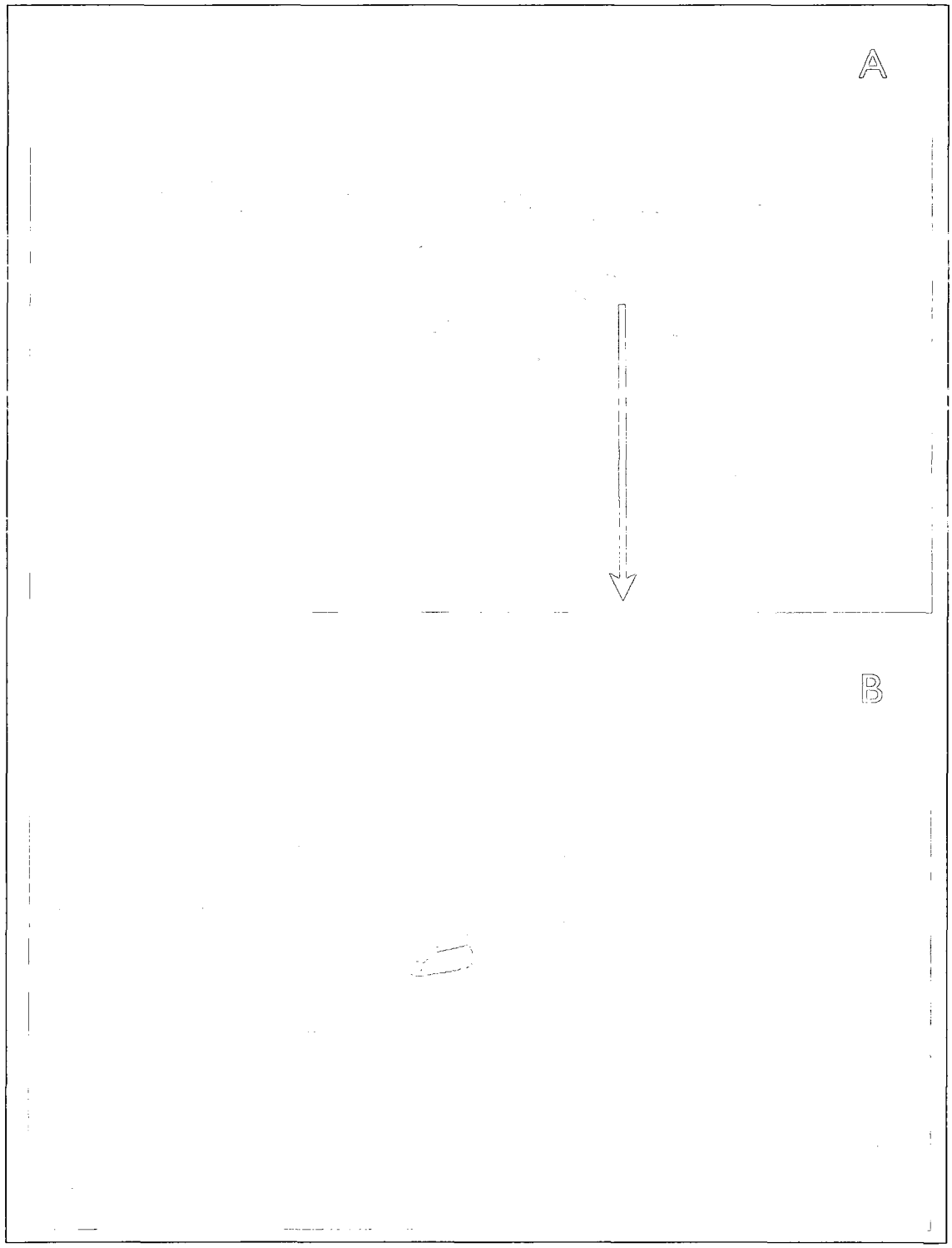

Figure 3.1 Images of the study site looking southwest displaying a 'street' in A, and large mesquite nabkha dunes with a truck for scale, looking south in B.

3.2 Wind Direction Bins

All of these data collected were divided into 16 bins based on wind direction at the time measurements were taken. Each direction consisted of a 22.5° segment of azimuth, with a total of 16 directions shown in Table 3.1. If the wind was recored as blowing from the south by the regional wind vane then all these data that corresponded to that same time period were flagged as data from the south. These data were divided into wind directions for comparison of the wind characteristics between wind directions.

Table 3.1 The 16 wind directions used in the study to segregate these data.

Bin	Mean direction	Direction range (°)
1	N	348.76 - 11.25
2	NNE	11.26 - 33.75
3	NE	33.76 - 56.25
4	ENE	56.26 - 78.75
5	E	78.76 - 101.25
6	ESE	101.26 - 123.75
7	SE	123.76 - 146.25
8	SSE	146.26 - 168.75
9	S	168.76 - 191.25
10	SSW	191.26 - 213.75
11	SW	213.76 - 236.25
12	WSW	236.26 - 258.75
13	W	258.76 - 281.25
14	NW	281.26 - 303.75
15	WNW	303.76 - 326.25
16	NNW	326.26 - 348.75

3.3 Vegetation Measurements

The height of individual nabkhas and the height of the vegetation on them were measured using a survey level and stadia rod. Measurements of the nabkha perimeters were made using Differential GPS to map the areal coverage and orientation of the nabkhas over the

Figure 3.2 Sample raster image used to estimate optical porosity.

study site. These vegetation measurements were then used to calculate λ based on 16 cardinal wind directions. As the wind changes direction it encounters the nabkhas on different faces therefore changing the effective frontal area which is used to calculate λ. Arc GIS 9.2 software was used for for the calculation of roughness density as a function of wind direction by measuring b, in Eq. 2.3, perpendicular to azimuths for each roughness element in the study site. The product of b and h in Eq. 2.3 is the frontal area of the roughness object.

Estimations of optical porosity were also made for the site from digital images of the vegetation structure against a white backdrop. Optical Porosity measurements were made for the plants to gain an understanding of the plant structure. The images of the plants were analyzed using Arc GIS 9.2 software. To minimize error, images were cropped to exclude edges of the plant. Any white cell in the image was considered open space and cells that were black were treated as solid. Optical porosity was then calculated using Eq. 2.6; a sample image can be seen in Fig. 3.2. Optical porosity is a surrogate for the volumetric porosity because light rays travel through vegetation differently than the way wind flows through the vegetations' porous space. Grant and Nickling (1998) demonstrated that there is a strong relationship between volumetric porosity and optical porosity.

Frontal area of the roughness objects are affected by the porosity and hence porosity values were added to the calculation of λ. As an example, if a nabkha had a total height of 2 m and was 2 m wide and the vegetative component was 0.5 m tall (i.e., the top 1/4 of the plant) then the OP measurement would be used to estimate the frontal area of just the

solid vegetation. In this example, if the plant had an OP of 0.2 then the frontal area of the vegetative component would be (2 m × 0.5 m × 0.2 =) 0.2 m^2 and the frontal area of the sand component of the roughness would be (2 m × 1.5 =) 3 m^2. This would equal total frontal area for the object of (3 m^2 + 0.2 m^2 =) 3.2 m^2.

3.4 Wind Speed and Direction Measurements

The driving force for aeolian sediment transport is shear stress. Shear stress at the surface can be estimated by the Prandtl-von-Kármán equation (Eq. 2.1) where measurements of the vertical wind speed gradient are taken to obtain the friction velocity (u_*) (Dong et al., 2001; King et al., 2006). A sparsely vegetated and highly heterogeneous surface, such as the study site will have a high degree of spatial variability in the near-surface wind field. To adequately characterize the mean vertical wind speed gradient in and above a vegetated canopy of this type would be very difficult because of the dynamic nature of wind flow. Raupach (1989) and King et al. (2006) suggest that to appropriately measure u_* would require the installation of multiple meteorological towers throughout the dune field with vertical arrays of anemometers measuring the vertical wind profile. Furthermore, the application of the Prandtl-von-Kármán equation in complex vegetation is inaccurate for prediction of friction velocity and shear stress because of the development of separated wind flow patterns (Gillies et al., 2006), which create multiple internal boundary layers (Raupach, 1992). Hence, logistical considerations with set-up and maintenance of multiple meteorological towers prohibit this style of investigation. These two considerations led to adopting a different approach to quantify the role of wind on the sediment transport.

With the goal of creating a regional wind erosion model, a new method of quantifying the wind that drives sediment transport is used by measuring free-stream wind speed at 18 m above the surface while simultaneously measuring near-surface wind speeds throughout the vegetation. An 18 m meteorological tower was erected to measure regional wind speed and direction that is well above the wind flow affected by the friction and flow separation created

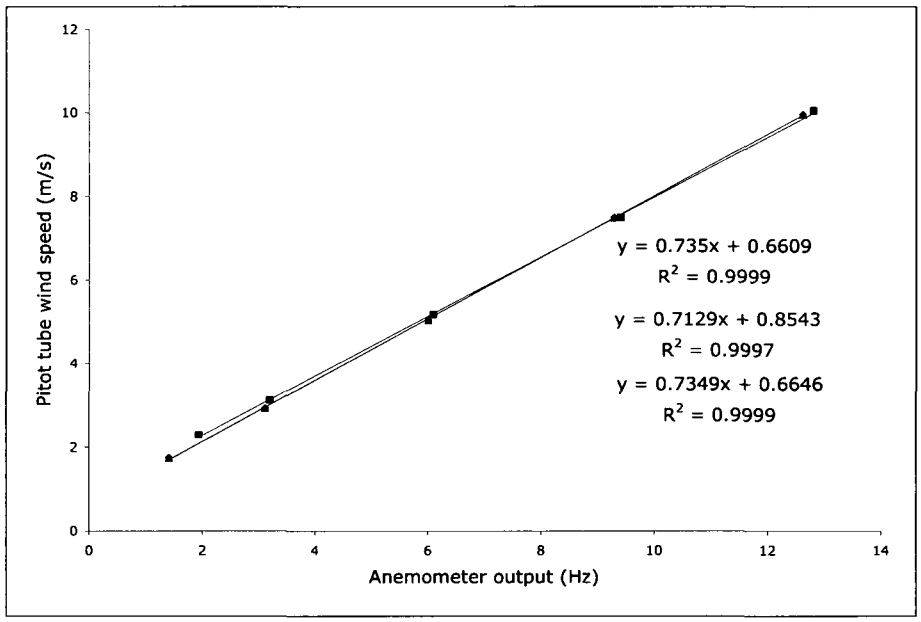

Figure 3.3 Three sample calibration curves of cup anemometers.

by the roughness at the surface. Raupach et al. (1980) suggests that wind flow is typically only affected at 2 to 5 times the height of the roughness elements. Measurements of wind speed and direction were taken throughout the vegetation community at 35 locations. Wind vanes and cup anemometers were mounted on 35 separate 'mini-towers' and set at a height of 0.38 times the mean nabkah height (h) at the site. A ratio of wind speed measurements at $0.38h$ to that measured at 18 m are used to characterize the relative strength of the winds near the surface and are also used to evaluate the spatial and directional variability of the wind within the vegetation. An image of a mini-tower can be seen in Figure 3.4. Labels A and B correspond to the cup anemometer and wind vane, respectively.

The array of meteorological instrumentation included: a RM Young 5103 wind vane and anemometer to measure the regional wind speed at 18 m; 28 RM Young WindSentry cup anemometers and 7 NRG #40C cup anemometers to measure surface wind speeds on the mini-towers; 13 RM Young WindSentry wind vanes and 22 NRG#200P wind vanes to measure near surface wind direction on the mini-towers. All wind measurements were recorded at 1 Hz with Campbell Scientific CR10X or CR1000 dataloggers, onboard computer

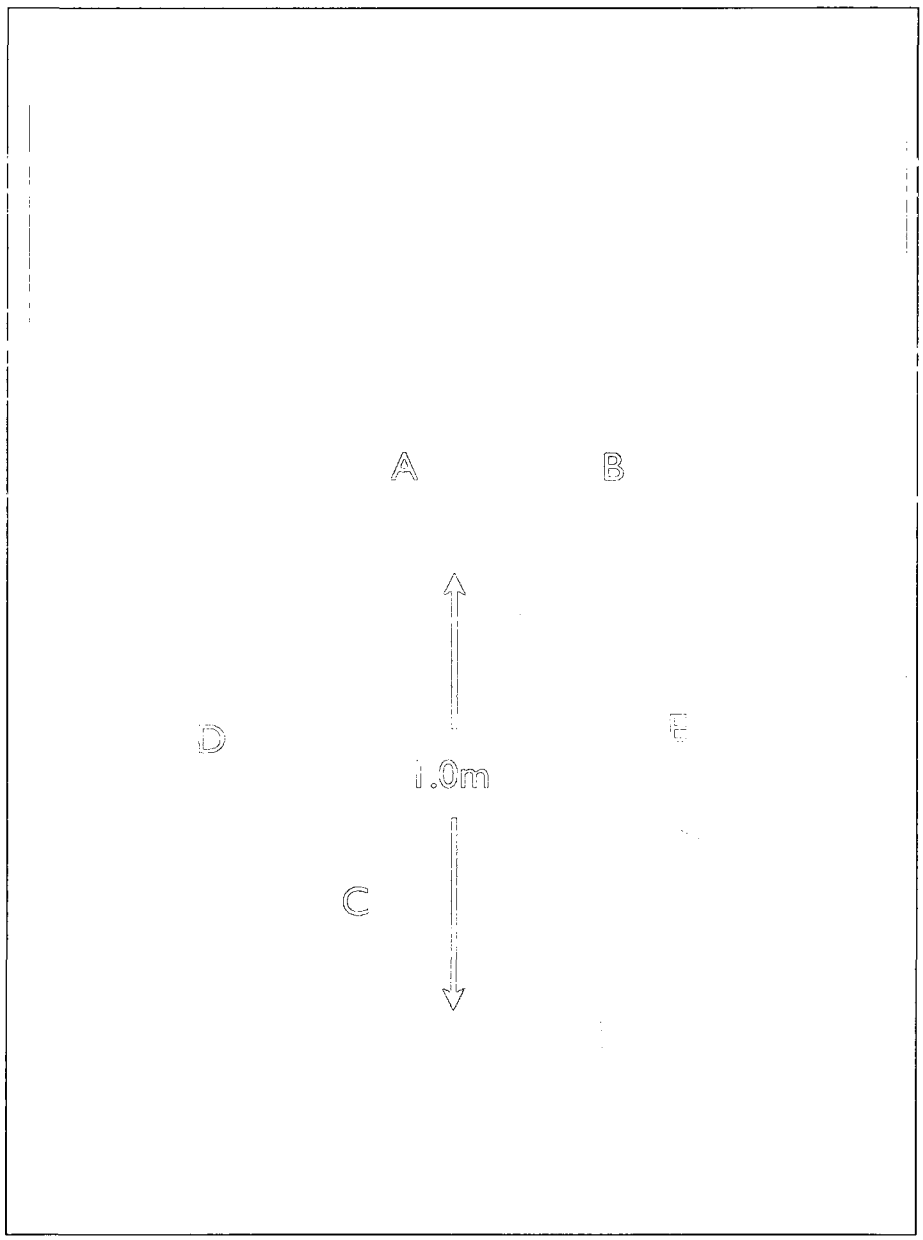

Figure 3.4 A mini-tower at the field site, with a cup anemometer, A, a wind vane, B, a Safire, C, an Irwin sensor, D, and a BSNE trap, E.

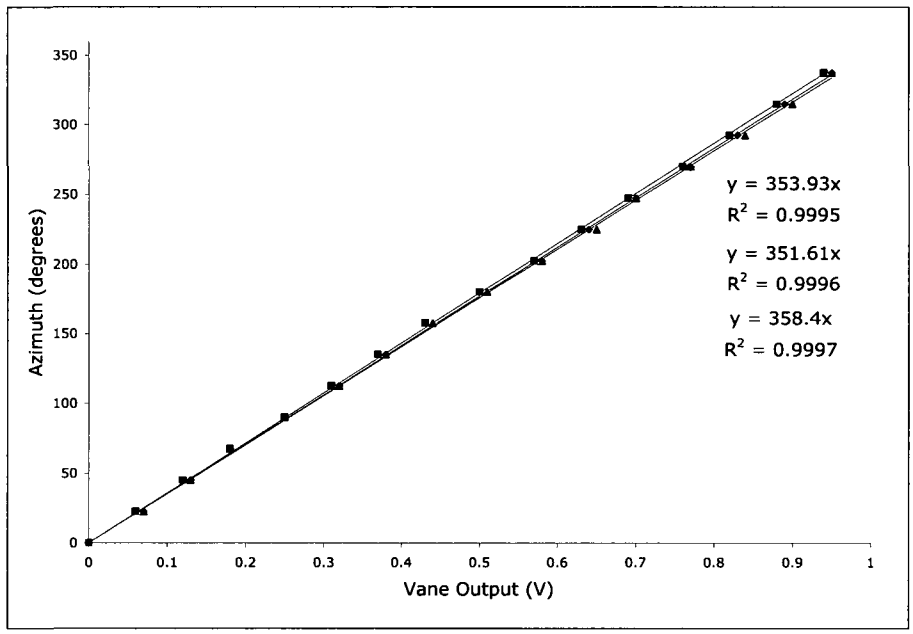

Figure 3.5 Three sample calibration curves of wind vanes.

programs converted raw input data to wind speeds in $m \cdot s^{-1}$ or direction in degrees based on individual calibration relationships. Calibrations of the anemometers were carried out in the University of Guelph's recirculating wind tunnel. Sample calibration curves and equations for the anemometer are presented in Figure 3.3. Raw voltage outputs from the wind vanes were calibrated against azimuth; sample calibration curves are shown in Figure 3.5. Reduction of wind speed data included the calculation of 10 minute averages for wind speed and direction, including standard deviation of both. Wind direction means were calculated using the method proposed by Mori (1986).

To assess the effect of wind direction on the near surface wind speeds a ratio of the 10 minute average wind speeds from the mini-towers to the 10 minute averages of the regional tower were calculated. The near surface wind speed ratio will henceforth be referred to as RWS. Values of RWS ranged from 0 to 1, where a value of zero signifies that the near surface anemometer is not moving and a value of 1 indicated that the near surface wind speed is exactly the same as regional wind speed.

Only the near surface wind speeds greater then 1 $m \cdot s^{-1}$ were used for the analysis.

When the 10 minute average near surface wind speed fell below 1 m/s there is a risk that any 1 second that comprised that average could be 0; when that happens the wind speed ratio breaks down.

These RWS data were then flagged and divided into their respective wind directions. These data were then displayed on RWS maps. For each direction the map indicates the magnitude of the RWS at each mini-tower location. These RWS data were also reduced further to site means for each direction. These data were then used for comparison with λ values and between wind directions.

3.5 Surface Shear stress Measurements

To accompany wind speed and direction measurements, 28 Irwin sensors were deployed to measure surface shear stresses and surface wind characteristics. Irwin sensors are simple, omni-directional skin friction meters that measure the near surface vertical pressure gradient (Irwin, 1981). The dynamic pressure differential is measured between two ports, one at the surface and the other at a height of 1.75 mm above the surface. Irwin sensors can sample at frequencies greater then 10 Hz (Irwin, 1981) and have been successfully deployed in the field (Wyatt and Nickling, 1997; Gillies et al., 2006, 2007) and in wind tunnel testing (Crawley and Nickling, 2003; Brown et al., 2008; Saaliste, 2008).

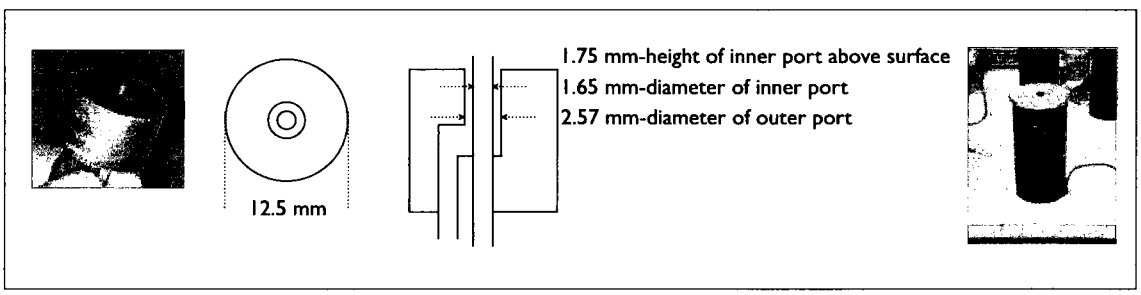

Figure 3.6 Picture, plain view, cross section, and field housing of an Irwin sensor.

An Irwin sensor consists of a brass cylinder, 12.5 mm in diameter, with a 2.57 mm center tap, which acts as a surface pressure port. A 1.65 mm diameter stainless steel tube is located in the center of the center tap, and measures pressure at 1.75 mm above the

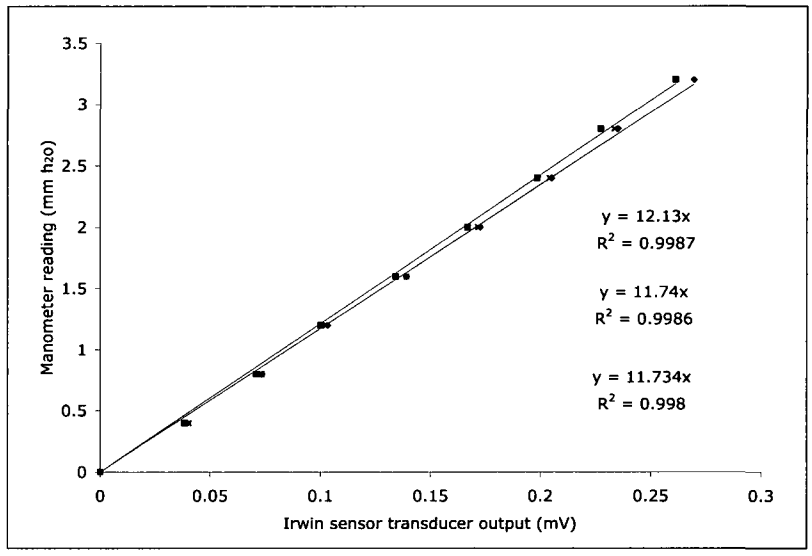

Figure 3.7 Three representation calibration curves of Irwin sensors.

surface. The difference in pressure between the stainless steel tube and the center tap is transmitted to a Honeywell 0.0254 m (1") Differential Pressure Sensor through 0.04 m of 1.59 mm Tygon tubing.

The Irwin sensors were placed in close proximity to 28 randomly selected anemometer/wind vane towers. The Irwin sensors were buried flush with the surface, seen in Fig. 3.4. Irwin sensors were placed close to their assigned mini-towers to ensure that they would not be buried by mobile sand sheets. A thin layer of a sand/concrete mix was placed around each Irwin sensor to ensure that saltating grains would not clog the measurement ports. Irwin sensor data were measured at 1 Hz and recorded at 0.1 Hz averages to Onset HOBO dataloggers.

Raw 0.1 Hz mV Irwin sensor values from the field required the application of the calibration information developed at the University of Guelph's wind tunnel laboratory. Sample curves are displayed in Fig. 3.7.

Day-to-day changes in atmospheric pressure required the calculation of daily field offset values. Daily field offset values were calculated by regression relationship estimated by the least of squares method for 10 minute average regional wind speed squared ($m^2 \cdot s^{-2}$) values

and the associated 10 minute average mV output from the pressure transducer, a method that follows Gillies et al. (2007). The Irwin sensors require a minimum wind velocity to properly activate the pressure transducer (p.comm, Nickling), and hence only values from the storm events were used in the analysis for this study.

The raw mV were then reduced to 10 minute averages and converted to a wind speed using Eq. 4 in Irwin (1981). These wind speed values were then converted to surface shear stress (τ_s) values using Eq. 2.4. Ten minute average τ_s values for each sensor were ratioed to the associated 10 minute average regional wind speed squared ($m^2 \cdot s^{-2}$). The ratioed surface shear stress values will henceforth be referred to as the RSS. These RSS data were then sorted by their respective wind directions for further analysis.

3.6 Sand Flux Measurements

Saltation flux values in this study were measured using 33 high temporal resolution saltation sensors called SAltation Flux Impact RESponders (SAFIRES). The Safires provide high-frequency omni-directional sand flux data with little obstruction of the wind (Baas, 2003) and have been successfully used in the field (e.g., Stout and Zobeck, 1997; Gillies et al., 2006; Bowker et al., 2006; Davidson-Arnott et al., 2008). Safires use high sensitivity piezoelectric crystals that create a variable voltage output that can be calibrated against a known sand flux, shown in Fig. 3.8. This current study required a high temporal resolution of sediment flux data to study the relationship between wind speed and direction at both regional and near-surface heights. High temporal resolution data were critical to understanding the characteristics of the vegetation that affect the wind field and sediment transport.

Safires were placed within 1 m of 33 mini-towers and the sensors were 8 cm above the surface. Safire locations can be seen in Table 3.2. Measurements made by the Safires were used to determine when aeolian sediment transport is occurring and an estimate of how much is moving. Ten BSNE sediment traps were randomly co-located with ten safires

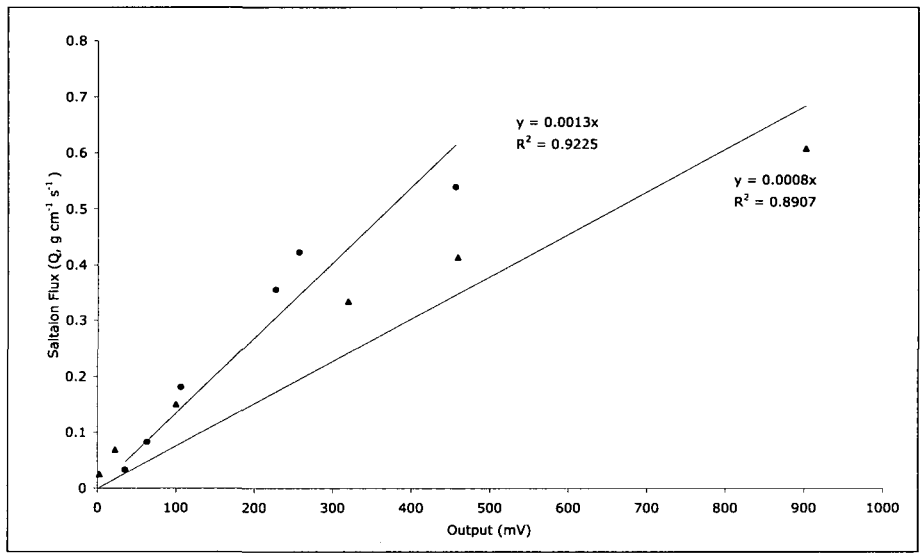

Figure 3.8 Two sample calibration curves of Safires.

collecting sediment samples to test the accuracy of the calibrated flux values from the 13 sediment transport events. These Safire data were collected using 7 Campbell Scientific CR10x dataloggers.

Safires display variation in response depending on azimuth direction, and hence four calibration curves were developed for the four cardinal directions. Ten minute averages for saltation flux were calculated using the calibration curve that was most closely related to the mean wind direction. The values of saltation flux were then sorted by their respective wind directions for further analysis.

To determine the individual field offset values a novel method was developed. Data over a 3 day period, when wind speeds were well below the threshold for sediment movement, were analyzed using an iterative calculation for saltation intermittency over an increasing range of Safire mV offset values. Stout and Zobeck (1997) define saltation intermittency, γ_p, as the fraction of time when saltating particles are detected at a given point during a given time period. Values of γ_p fall between 0 and 1, indicating inactivity and continuous saltation, respectively. According to Stout and Zobeck (1997), the calculation of γ_p requires two parameters: time, t, and particle impacts per second, $p(t)$. Intermittency was calculated

over 10 minute periods that contain 600 lines of data each. Values of γ_p must be constructed from an intermittency signal, $b_p(t)$, defined as

$$\begin{aligned} b_p(t) &= 0 \text{ if } p(t) = 0 \\ b_p(t) &= 1 \text{ if } p(t) > 0 \end{aligned} \tag{3.1}$$

From this the saltation intermittency, γ_p, can be calculated by taking an average of $b_p(t)$ over each ten minute period or

$$\gamma_p = \frac{1}{N} \sum_{i=1}^{N} b_{p_i} = \overline{b_p(t)} \ , \tag{3.2}$$

where N = 600.

The calculation of the Safire offset values, used Eqs. 3.1 and 3.2 over a range of increasing offset values by 0.01 mV for each iteration. The range of offset values went from the mean mV output of the individual Safire data over the 3 days, to the point where $\gamma_p \leq 0.001$. This value gives a one percent leeway in the calculation of offset; decreasing the γ_p any further would increase the offset values too high and would also assume that the instruments offset does not drift at all.

To evaluate the response of the Safires, calculated flux over storm periods was compared against calculated flux from BSNEs at 10 of the Safire locations. Figure 3.9 shows that the saltation flux values measured by the Safire correspond to the measured flux from the BSNE, but the Safires' values are generally an order of magnitude smaller. At all the locations where the BSNEs and Safires were compared a similar trend was observed. The analysis used in this study assumed that individual Safire response to saltation activity did not change through the duration of the study. This assumption allows for comparison of individual safires through time.

3.7 Sample Locations

All the instruments were placed within a 100 m radius surrounding the 18 m meteorological tower (located at 106°43'11.546W 32°41'3.784N), which is represented by the star

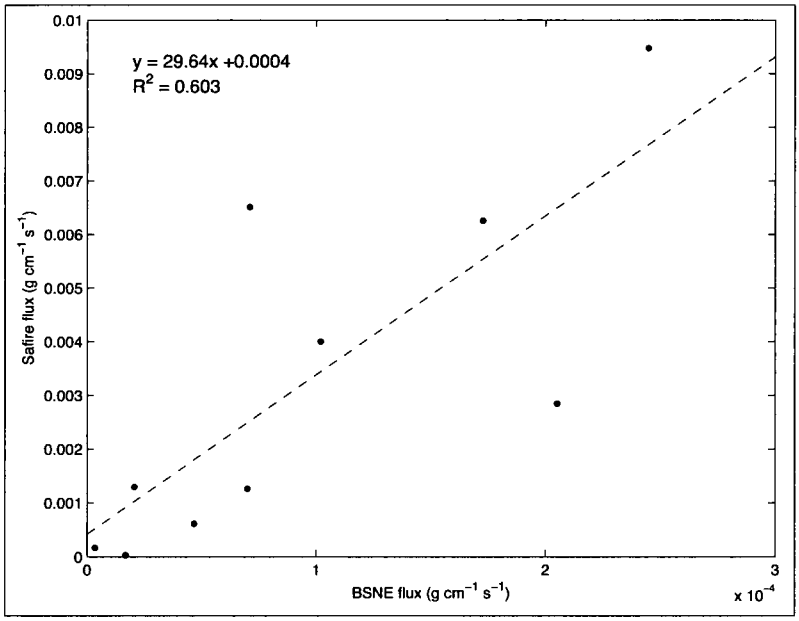

Figure 3.9 Calculated saltation flux from Safire 11 compared against measured saltation flux values from a co-located BSNE.

in the middle of Fig. 3.10. The 35 mini-towers, with wind vanes, anemometers, and Safires were located in the 35 most exposed locations within the study site. Within the study site the 35 sampling locations were determined using GIS software to locate the most exposed areas using the GIS map of nabkhas. The maps were imported into the Arc GIS 9.2 software package where a raster image of vegetation coverage and soil was generated. Then, using the Euclidian distance tool, pixels in the vegetation were assigned values of distances away from vegetation. A user-defined algorithm assesses every pixel in the image to pinpoint local maximum pixels. Thirty-five of the most exposed locations were used for instrument sites; however, some discretion and logistical considerations influenced the placement of instruments. Geographic coordinates of the instrument sites were located in the field using a differential GPS. A map of the study site and the sample locations are displayed in Figure 3.10, and locations of the Irwin sensors, Safires and BSNEs are listed in Table 3.2

For a number of reasons sensors were placed in the most exposed locations, as opposed to sampling in a range of locations within exposed areas (which would measure information

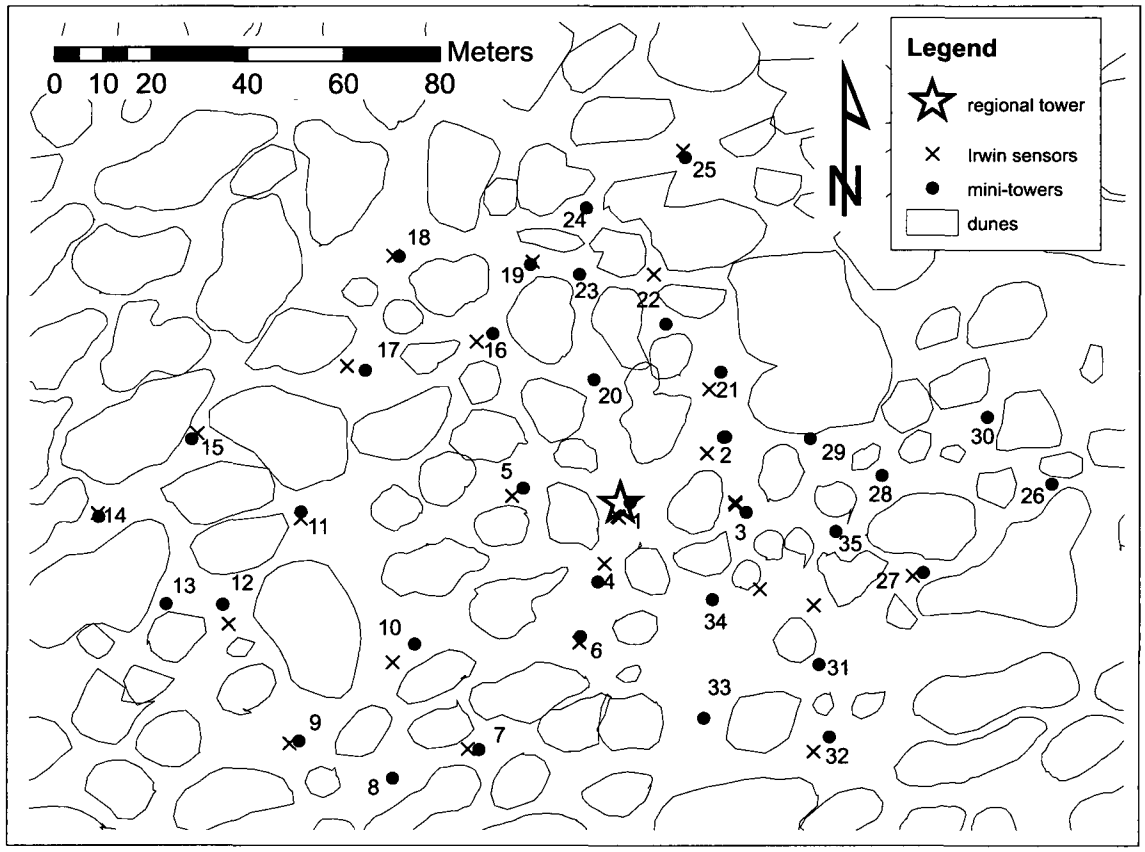

Figure 3.10 Jornada nabkha site map for the March-April 2009 season. Positions of the mini-towers and Irwin sensors are indicated by the symbology in the legend. The number of each mini-tower is next to the sample location.

Table 3.2 Locations of Irwin sensors, safires and BSNEs within the study site.

Tower #	Irwin sensor #	Safire #	BSNE #
1	1 and 6	1	1
2	2	2	–
3	3	3	–
4	4	4	–
5	5	5	–
6	-	6	–
7	7	7	7
8	–	8	–
9	9	9	–
10	20	10	–
11	11	26	–
12	12	12	–
13	–	11	11
14	14	14	–
15	28	15	–
16	16	-	–
17	17	17	17
18	18	18	–
19	23	19	–
20	-	20	–
21	20	21	21
22	-	22	–
23	–	–	–
24	–	24	24
25	25	-	–
26	21	16	–
27	26	23	23
28	–	28	28
29	29	29	–
30	–	30	–
31	15	31	31
32	13	32	–
33	–	33	33
34	27	34	–
35	–	35	–

on the distribution of wind flow and stresses). First, regardless of wind direction the instrumentation will always be in the most exposed location. The areas that are most exposed will be subject to the greatest stresses and should represent the position where the threshold for sediment movement occurs first. The assumption is that if the area under investigation is going to be reaching a critical threshold in landscape modification and undergo sediment movement the most exposed locations will experience this first. One additional Irwin sensor was placed in the middle of a large playa about 2.5 kilometers southwest of the study site to give a reference of shear stress in a completely open space.

CHAPTER 4

RESULTS

Results of the ratioed wind speed (RWS), ratioed shear stress (RSS), saltation flux (Q), saltation intermittency (γ), and near surface wind direction are presented to demonstrate how their parameters change with azimuth. Results of the near surface wind characteristics are compared against λ values for the 16 different wind directions. Additionally, maps are presented for each wind direction to characterize the near surface wind field, surface shear stress and saltation activity. The maps contain the location of each sensor throughout the dune field. In total 56 maps were made, 16 maps for both wind speed and direction, and 12 maps each for surface shear stress and saltation flux. Each map represents the average value for each sensor for each wind direction. For presentation purposes these map data were divided into five classes reflecting magnitudes of the respective measurements. The Natural Breaks (Jenks) algorithm in Arc GIS 9.2 was used to determine the class ranges. Maps from the SE and SW wind directions were chosen to represent the wind characteristics for directions with the second lowest and second highest λ values.

4.1 Vegetation and surface roughness

Vegetation characteristics of the field site are detailed in Table 4.1. The number of nabkhas used to calculate λ was 308 with a mean basal width of 12.7 m, and a mean height (dune plus vegetation) of 2.631 m. The nabkha dunes are covered in vegetation (porous), however this vegetation is growing on a sand mound (non-porous) that is on average 1.69 m tall. The average vegetative component of the dunes is 0.941 m or $\approx 1/3$ of the total roughness height, which can be seen in Fig. 4.1. The optical porosity calculations were only applied to the portion of the dune (i.e., the vegetative porous component) that was vegetation. The average optical porosity of the mesquite vegetation is $0.171(\pm 0.041)$, which

indicates that the plant structure is not that porous compared to previous studies with porosity values ranging from 0.15-0.53 (Wyatt and Nickling, 1997; Grant and Nickling, 1998; Gillies et al., 2002).

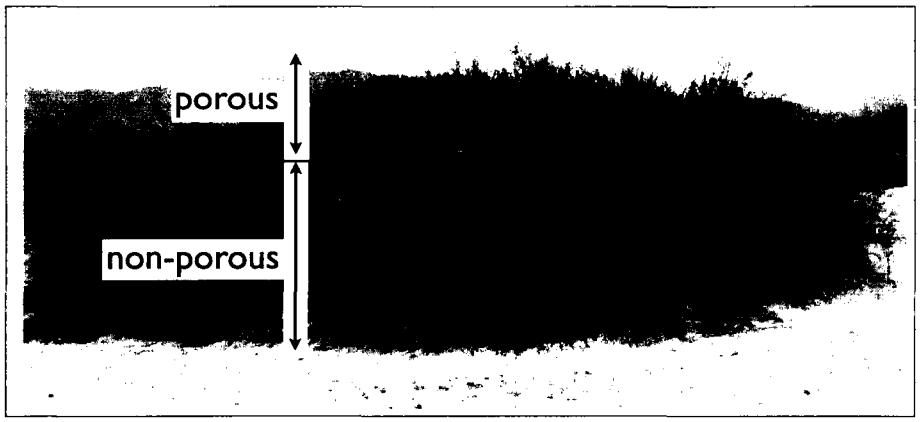

Figure 4.1 Jornada nabkha with porous and non-porous components of the dune.

Table 4.1 Summary of the parameters on which the calculation of λ is based.

Parameter	Value
# of dunes	308
mean basil width	12.7 m
mean dune height - nonporous component	1.69 m
mean dune height - vegetative component	0.941 m
optical porosity	0.171
total surface area	80356.46 m^2
Average λ	0.122

The total vegetative roughness cover over the study site was ~50%. The average λ value on the study site is 0.122. In this study 16 different λ values were calculated ranging from 0.108 to 0.132. Values of λ were calculated for each wind direction and are represented by the dashed lines in Figs. 4.4, 4.10, and 4.18. λ values were calculated to represent the surface roughness as the wind encounters the nabkhas. Nabkhas are not symmetrical and wind from different directions encounters different basal widths of the same dune. The variations in average basal widths result in the variations of the reported λ values. Table

Table 4.2 Mean basal width of the nabkhas for each wind direction.

Direction	mean basal width
N	13.53
NNE	12.54
NE	11.71
ENE	11.42
E	11.87
ESE	12.86
SE	13.70
SSE	13.97
S	13.53
SSW	12.54
SW	11.71
WSW	11.42
W	11.87
NW	12.86
WNW	13.70
NNW	13.97

4.2 shows that winds from the ENE and WSW encounter the dunes when the average basal width is at a minimum; winds from the SSE and NNW encounter the dunes when the average basal width is the greatest. The maximum and minimum basal widths correspond with the maximum and minimum λs. Obviously there is symmetry to calculations of λ, in that opposite cardinal directions will have the same average basal widths and therefore the same λ values.

Gillette and Pitchford (2004) describe nabkhas at the JER as having 'streets', as indicated in Fig. 4.2. The mature nabkha communities have been determined by Okin et al. (2004) to be distinctly organized into linear forms aligned with the dominant wind direction($\sim 225°$). The lower values of λ calculated for the southwesterly directions at this site demonstrate the 'elongated bare streets' discussed by Okin and Gillette (2001).

Basal widths were tested to determine if there were differences in λ values because they are the parameter that results in changes when λ is calculated. Two-tailed t-tests were performed to evaluate if the means of each of the basal widths from each wind direction were

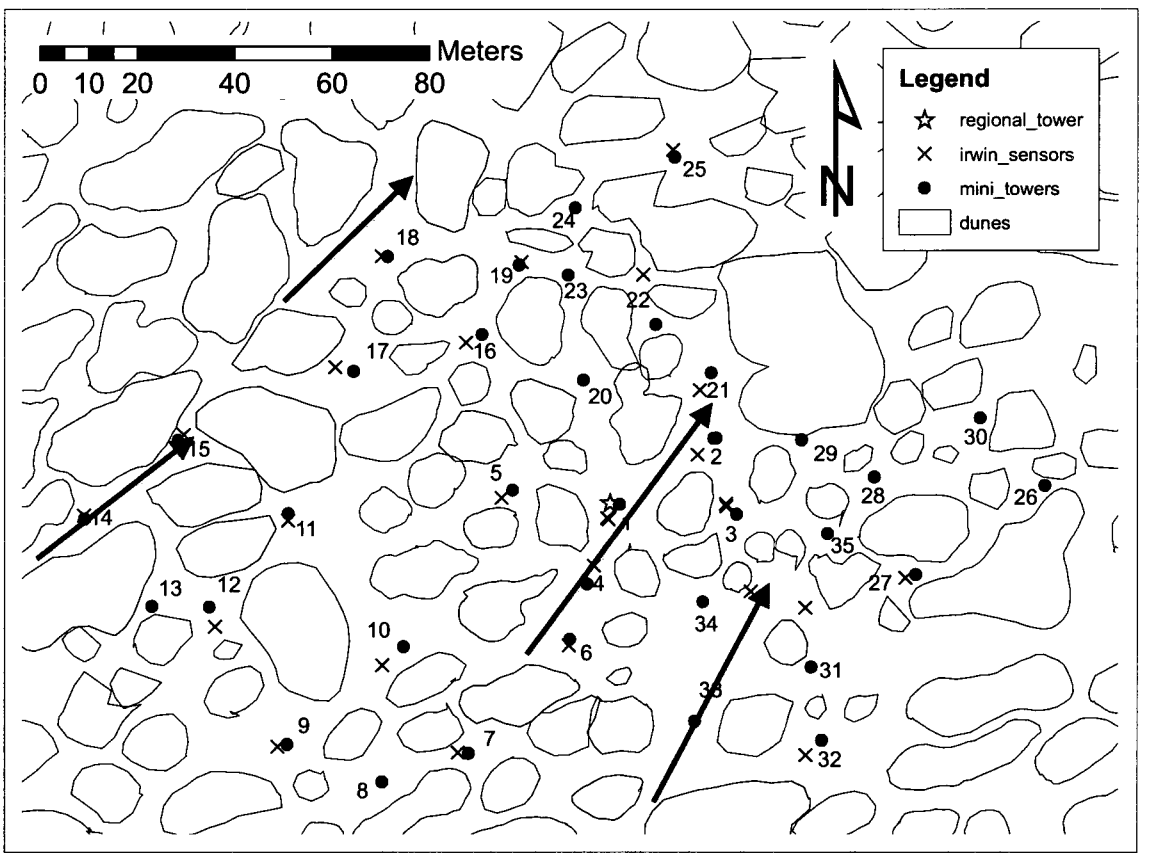

Figure 4.2 Jornada nabkhas with the visual identification of streets indicated by the arrows. The number of each sensor is also displayed.

Table 4.3 P values for two-tailed t-tests performed on the basal widths of the dunes. The highlighted values indicate a significant difference at the 95% confidence interval between the mean basal widths of the dunes from different wind directions, signifying a significant difference in the λ values.

	N	NNE	NE	ENE	E	ESE	SE	SSE
NNE	1.88E-01							
NE	1.61E-02	2.63E-01						
ENE	5.70E-03	1.34E-01	6.96E-01					
E	2.97E-02	3.70E-01	8.34E-01	5.53E-01				
ESE	3.82E-01	6.70E-01	1.28E-01	5.90E-02	1.95E-01			
SE	8.29E-01	1.26E-01	4.95E-03	2.99E-03	1.73E-02	2.78E-01		
SSE	5.78E-01	6.13E-02	3.23E-03	9.86E-04	6.74E-03	1.55E-01	7.33E-01	
S		1.88E-01	1.61E-02	5.70E-03	2.97E-02	3.82E-01	8.29E-01	5.78E-01
SSW	1.88E-01		2.63E-01	1.34E-01	3.70E-01	6.70E-01	1.26E-01	6.13E-02
SW	1.61E-02	2.63E-01		6.96E-01	8.34E-01	1.28E-01	4.95E-03	3.23E-03
WSW	5.70E-03	1.34E-01	6.96E-01		5.53E-01	5.90E-02	2.99E-03	9.86E-04
W	2.97E-02	3.70E-01	8.34E-01	5.53E-01		1.95E-01	1.73E-02	6.74E-03
WNW	3.82E-01	6.70E-01	1.28E-01	5.90E-02	1.95E-01		2.78E-01	1.55E-01
NW	8.29E-01	1.26E-01	8.95E-03	2.99E-03	1.73E-02	2.78E-01		7.33E-01
NNW	5.78E-01	6.13E-02	3.23E-03	9.86E-04	6.74E-03	1.55E-01	7.33E-01	

	S	SSW	SW	WSW	W	WNW	NW
NNE							
NE							
ENE							
E							
ESE							
SE							
SSE							
S							
SSW	1.88E-01						
SW	1.61E-02	2.63E-01					
WSW	5.70E-03	1.34E-01	6.96E-01				
W	2.97E-02	3.70E-01	8.34E-01	5.53E-01			
WNW	3.82E-01	6.70E-01	1.28E-01	5.90E-02	1.95E-01		
NW	8.29E-01	1.26E-01	4.95E-03	2.99E-03	1.73E-02	2.78E-01	
NNW	5.78E-01	6.13E-02	3.23E-03	9.86E-04	6.74E-03	1.55E-01	7.33E-01

significantly different from each other (Table 4.3). The t-tests show that in approximately 16% of cases basal width means are significantly different from each other, indicating that some of the λ values are distinguishably different from each other. Generally, significant differences in λ exist for directions that are perpendicular to each other, such as the SE and SW, NNW and the WSW, and the ENE and SSE. Directions adjacent to each other have basal widths that are too similar to each other and hence do not have significantly different λ values.

4.2 Ratioed wind speed

Ratioed wind speeds (RWS) were used to evaluate the near surface wind field and determine if there are changes with changing wind direction. Figure 4.3 indicates the magnitude of the RWS by the size of the grey circles at each of the mini-tower locations. The black arrow in the center of the map indicates the regional wind direction. Winds from the SW in Fig. 4.3 demonstrate higher overall RWS when the λ is lower; whereas, winds from the SE demonstrate lower overall RWS with a higher λ. Figure 4.3B shows that winds from the SW allow higher near surface wind speeds in the corridors aligned with this direction, shown in Fig. 4.2. Sensors 6, 4, 1, and 2 all show higher RWSs when winds flow from the SW as opposed to the SE. Sensors 14 and 15 also show an increase in RWS when wind flows from the SW because of the alignment of the nabkhas. The areas in the streets experience less sheltering than areas in the lee of nabkhas such as sensors 20, 22, and 23 in Fig. 4.3B. An interpretation of the RWS maps will be presented in §4.7 within the context of the wind direction, Q and RSS maps.

Figure 4.4 shows the average RWS for the entire dataset for each wind direction on the right axis and the values of λ for each wind direction on the left axis. This graphic shows the opposing trends of λ and RWS. Figure 4.4 shows that λ decreases with directions aligned in the SW-NE axis there is an observable increase in the near surface wind speed. This indicates that as the protection created by the nabkhas decreases there was an increase in

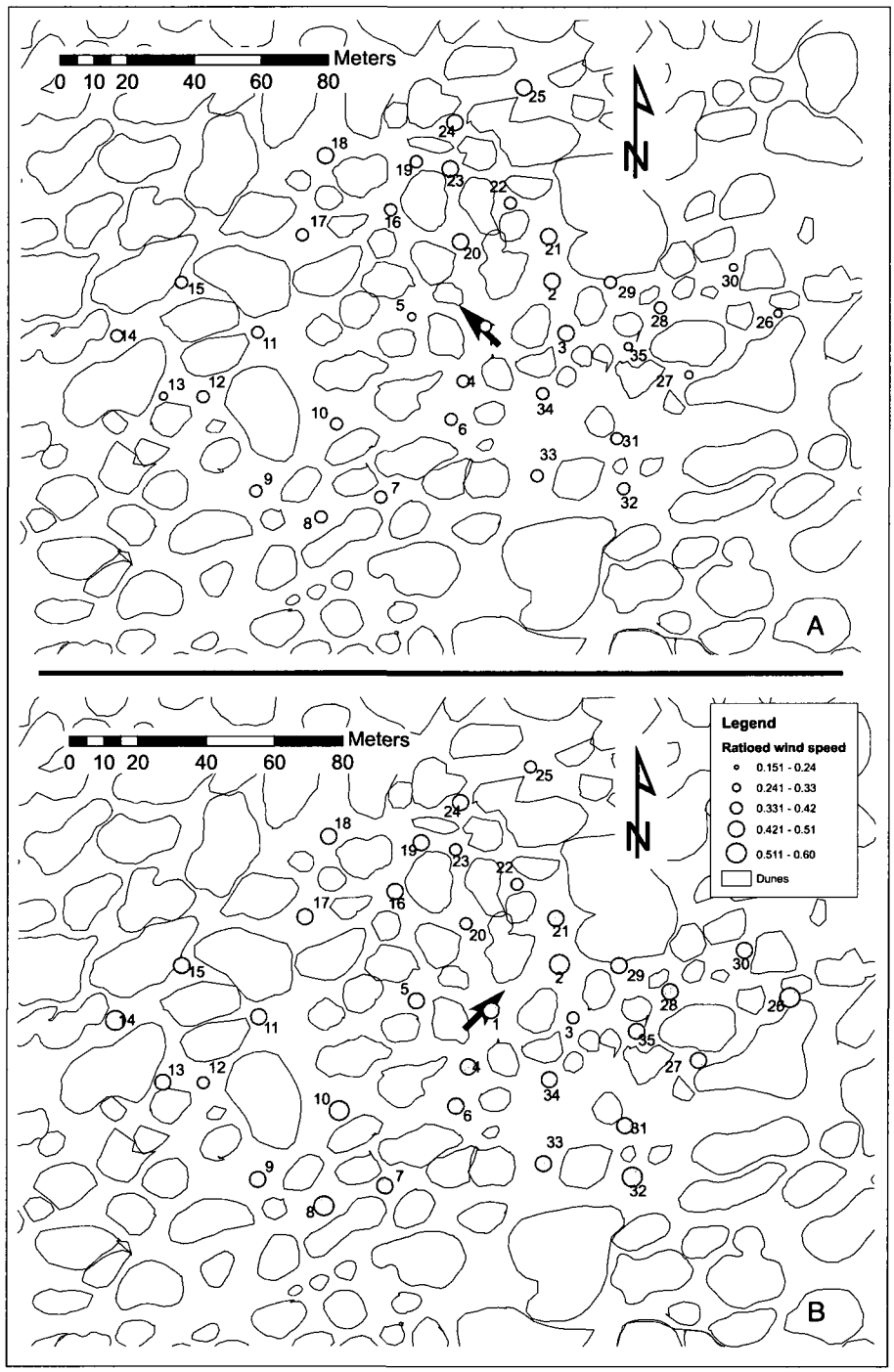

Figure 4.3 Ratioed near surface wind speed data for the SE(A) and for the SW(B). The size of the grey circles represents the magnitude of the ratioed wind speed, as outlined in the map legend. The black arrow in the center of the map indicates the direction the regional wind is flowing.

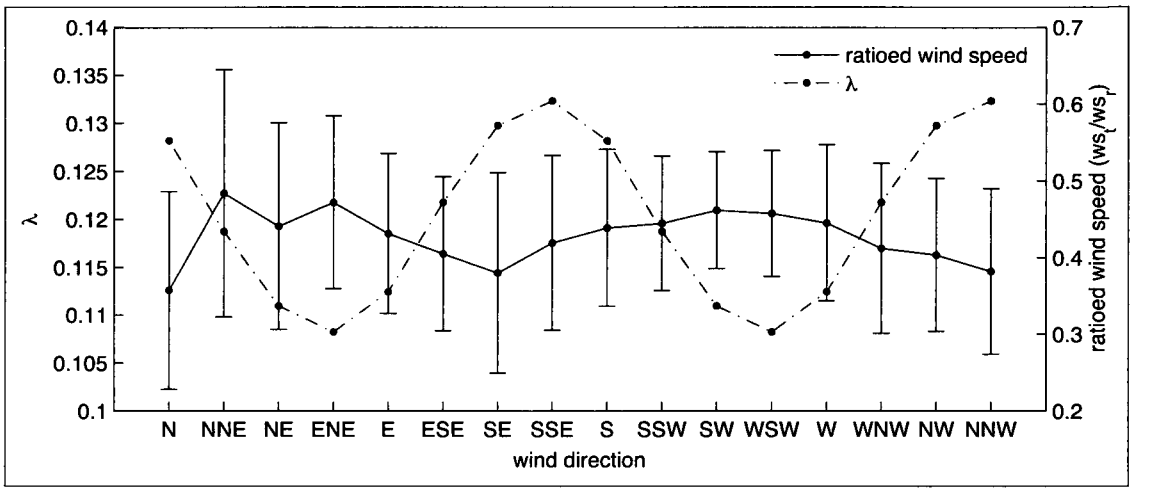

Figure 4.4 Ratioed wind speed, ws_t/ws_r, and site λ values by wind direction. As the λ value decreases (dashed line) there is an increase in the ratioed near surface wind speed values (solid line).

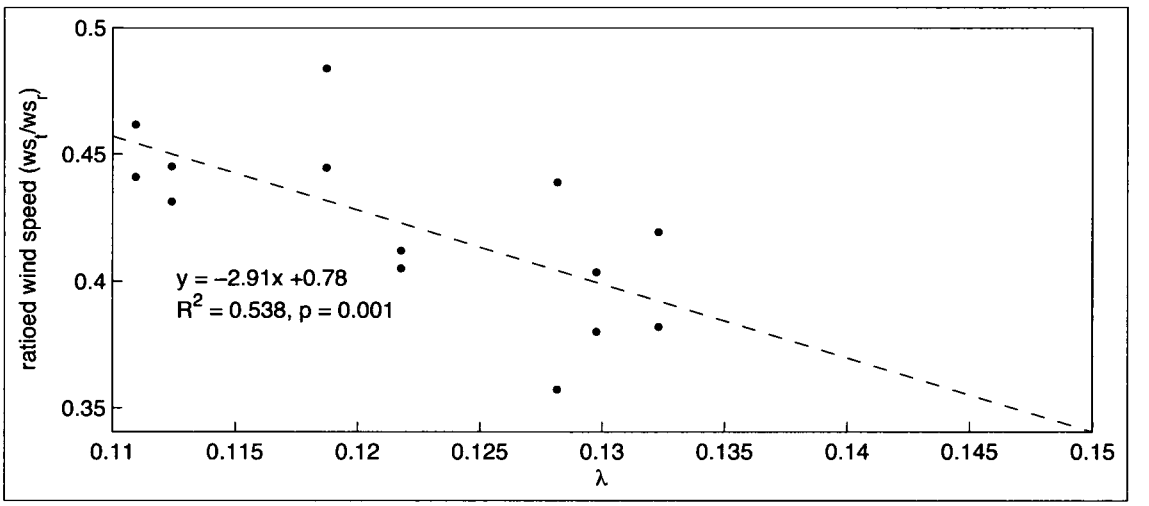

Figure 4.5 Ratioed near surface wind speed, ws_t/ws_r versus site λ values for the wind directions. This significant relationship, at the 99% confidence interval, shows that as the λ values associated with different wind directions increase the ratioed wind speed values decrease.

wind speed at 1 m above the surface. The highest value of RWS occurred when winds flowed from the NNE. Other high values of RWS occurred when winds flowed from the ENE. As well, winds from the SW had a high value of RWS. Low values of RWS occurred with winds from the N, SE, and NNW where λ values were the highest.

Table 4.4 P values for two-tailed t-tests performed on the mean RWS for each wind direction. The highlighted values indicate a insignificant difference between the means at the 95% confidence interval.

	N	NNE	NE	ENE	E	ESE	SE	SSE
NNE	1.00E-14							
NE	1.87E-21	3.30E-03						
ENE	6.86E-48	3.04E-01	1.17E-04					
E	1.09E-23	2.40E-04	2.17E-01	6.56E-10				
ESE	1.36E-12	8.60E-08	7.04E-07	1.22E-28	1.54E-06			
SE	1.83E-03	2.74E-11	2.38E-14	8.22E-41	8.64E-16	1.15E-05		
SSE	1.28E-22	6.92E-06	2.08E-03	3.95E-21	2.05E-02	2.29E-04	1.36E-14	
S	4.90E-38	1.00E-03	7.92E-01	1.96E-10	9.06E-02	2.33E-20	7.98E-33	5.15E-12
SSW	2.03E-43	3.41E-03	5.46E-01	5.38E-08	2.66E-03	2.68E-29	2.15E-40	9.25E-23
SW	1.27E-57	7.31E-02	1.35E-03	3.56E-02	1.73E-11	1.15E-55	1.12E-60	9.94E-63
WSW	5.81E-54	3.74E-02	1.07E-02	3.15E-03	6.81E-09	2.66E-48	2.86E-55	2.06E-50
W	4.36E-41	3.90E-03	5.37E-01	4.89E-07	4.91E-03	1.41E-23	4.96E-36	2.99E-15
WNW	1.99E-16	6.80E-07	3.91E-05	7.86E-25	2.15E-04	1.33E-01	9.33E-09	3.17E-02
NW	3.75E-13	4.51E-08	8.14E-08	3.25E-33	4.71E-08	7.57E-01	6.97E-06	2.45E-06
NNW	8.76E-05	2.32E-11	1.12E-16	5.13E-53	1.98E-21	6.48E-08	7.13E-01	4.14E-27

	S	SSW	SW	WSW	W	WNW	NW
NNE							
NE							
ENE							
E							
ESE							
SE.							
SSE							
S							
SSW	1.59E-03						
SW	3.81E-41	2.49E-48					
WSW	1.67E-26	2.90E-25	3.42E-05				
W	2.55E-02	9.10E-01	3.02E-13	8.04E-08			
WNW	7.89E-16	8.72E-25	9.08E-54	2.29E-45	4.80E-19		
NW	1.30E-32	7.77E-50	4.23E-96	5.93E-83	6.46E-35	4.18E-02	
NNW	4.10E-77	7.94E-105	2.91E-163	2.21E-147	3.73E-75	2.84E-02	2.93E-09

As a companion to Fig. 4.4, Fig. 4.5 displays the average RWS against λ. The points on this graph display a negative trend indicating that as λ increases there is a decrease in the RWS. The R^2 value for this relationship is 0.524; with 16 datum points this is significant at the 99% ($p = 0.002$) confidence interval. Overall, as surface protection decreased due to changing wind directions there was an increase in the RWS, indicating more wind energy reached the near surface, increasing the potential for sediment transport.

Two-tailed t-tests for unequal variances were proformed to evaluate if the means from each RWS were significantly different from each other (Table 4.4). The t-tests show that in approximately 90% of cases, RWS means are significantly different from each other, suggesting that as λ increases there is a significant decrease in RWS. In all the cases where there was an insignificant difference in the means of the RWS there was insignificant difference in the λ value, which would be expected because surfaces with similar λ values could be expected to have indistinguishable RWS values.

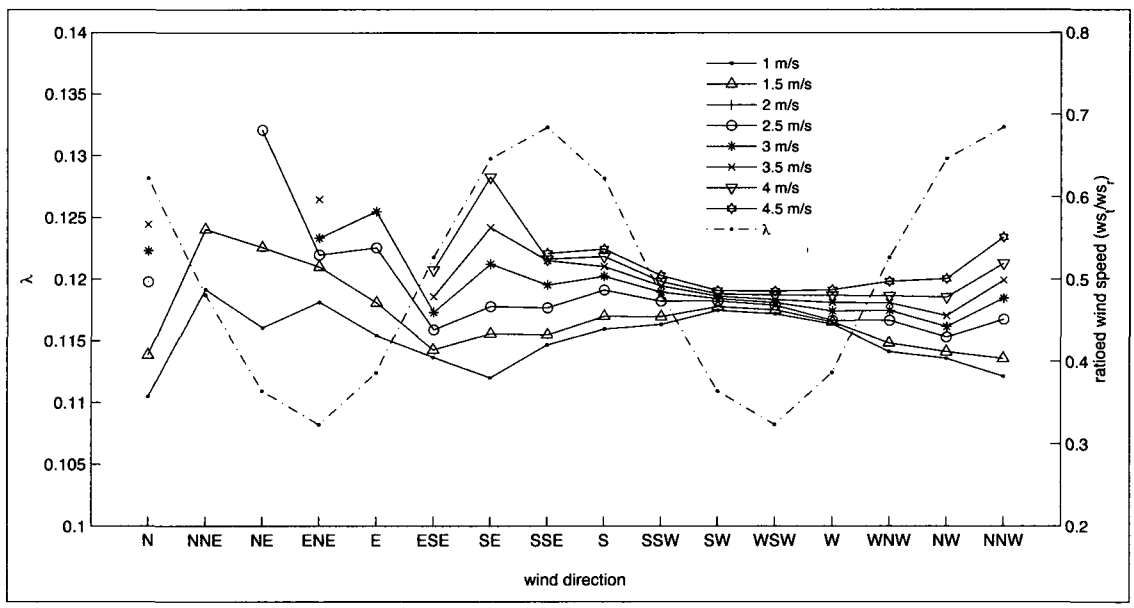

Figure 4.6 Calculated average RWS as the near surface wind speeds are increased by 0.5 m/s intervals. As near surface wind speeds increase there is also an increase in the RWS.

Figure 4.6 shows the RWS for the entire dataset as the near surface wind speed was

increased by 0.5 $m \cdot s^{-1}$ intervals. As the threshold for inclusion in the RWS dataset increased the RWS at the site increased. This indicates that increases in regional wind speed result in disproportional increases in near surface wind speed, suggesting that the roughness was less effective at surface protection. Figure 4.7 displays the RWS values versus the regional wind speed values as the threshold for inclusion in the RWS dataset increasd by 0.5 $m \cdot s^{-1}$ intervals. Figure 4.7 demonstrates that increases in the regional wind speeds result in a disproportionate increase in the RWS, meaning that the nabkhas were less effective at reducing sediment transport processes.

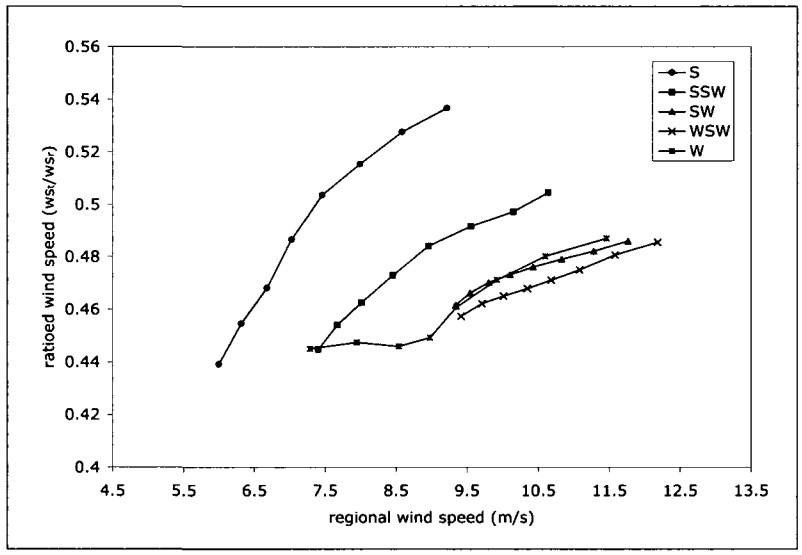

Figure 4.7 RWSs by direction plotted against the regional wind speed.

4.3 Threshold wind speed

Threshold wind speed for the site was estimated by plotting a histogram of the distribution of regional wind speeds for time periods when saltation activity was registered by the Safires. This method of establishing threshold is similar to that used by Gillette et al. (2006).The histogram (Fig. 4.8) shows that between 5 and 6 m/s there is a sharp increase in the amount of saltation recorded at the site, indicating that a threshold has been exceeded. These saltation data are presented later in §4.5. The greatest amount of saltation

was recorded between 10 and 11 m/s which is within the same range of mean wind speeds for the wind storm events observed at the site (shown in Table 4.5). Regional wind speeds between 10 and 11 $m \cdot s^{-1}$ were sufficient enough to create widespread saltation at the site. Figure 4.8 shows that the distribution of these data also has a positive skewness, which is expected and created by infrequent high wind speeds.

Table 4.5 Mean direction and wind speed for each storm event.

Storm #	1	2	3	4	5	6	7	8	9	10	11	12	13
Mean Dir	SW	WSW	W	SW	WSW	SW	SSW	SSE	SW	NW	SSW	SSW	SW
$\overline{u}$ (m/s)	9.7	10.3	11.2	11.2	11.8	11.2	7.9	7.0	9.7	9.3	8.7	10.9	10.3

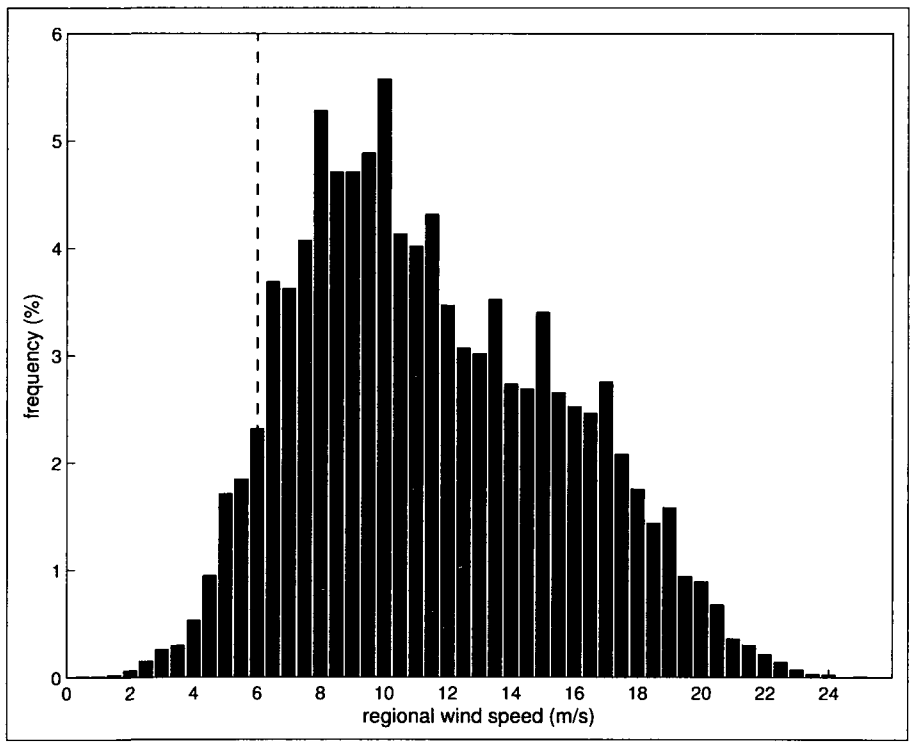

Figure 4.8 Distribution of the regional wind speeds when saltation activity was occurring at the study site.

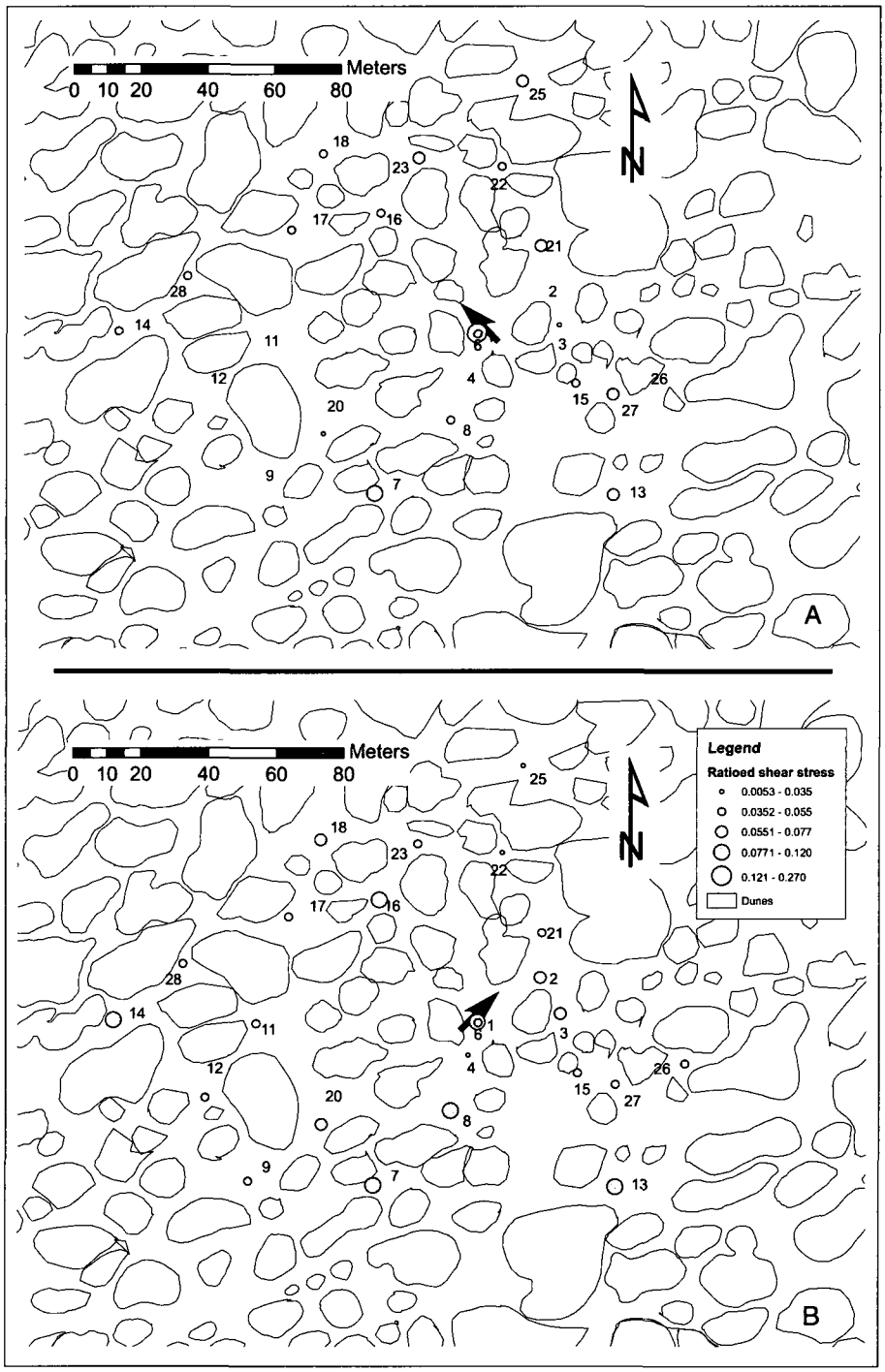

Figure 4.9 Ratioed surface shear stress data for SE (A) and SW (B). The size of the grey circles represents the magnitude of the ratioed shear stress, as outlined in the map legend. The black arrow in the center of the map indicates the regional wind direction flow.

4.4 RATIOED SHEAR STRESS

Ratioed shear stresses (RSS) were calculated to quantify the surface shear stress at the study site. The ratios were calculated as τ to regional wind speed squared (ws_r^2) because wind speed increases exponentially with height above the surface (Oke, 1987; Bowker et al., 2006). As well, wind speed squared is more appropriate for creating a ratio shear stress because in the calculation of τ values of u_* are squared as well (seen in Eq. 2.4). A and B in Fig. 4.9 show the RSS values for the SE and SW wind directions. The grey circles indicate the magnitude of the RSS values. Both of the maps show that there is an uneven distribution of RSS over the surface, where there are areas of high RSS and low RSS from both directions. The inhomogeneity in RSS is due to the inhomogeneity in the distribution of the roughness, where some locations are experiencing greater shear stresses than others. Comparing A and B in Fig 4.9 shows that there are a greater number of large RSS values in the SW than in the SE. High values of RSS seen in the SW are at sensors 7, 8, 13, 14, and 16. A fewer number of high RSS values can be seen in the SE at sensors 6, 7, 13, 21 and 27. The higher RSS values recorded at sensors 13, 21, and 27 can be explained by the exposure at these locations when the wind is blowing from the SE. For each of these sensors there is a long fetch upwind of them. Some of the high RSS values in the SW can also be explained by the degree of sensor exposure. Sensors 7, 8, 13, 14, 16 all have corridors of bare soil to the SW of them where the regional wind can mix deep into the roughness and create greater shear stresses at these locations.

Figure. 4.10 shows the mean RSS values for each wind direction plotted as a solid line. There was no RSS data for wind directions N to ENE because there were insufficient winds to activate the sensors in these wind directions. λ values for each wind direction were also plotted as a dashed line. Values of mean RSS were plotted against λ in Fig. 4.11 showing that there is no significant relationship within these data and the low R^2 indicates the presence of scatter in these data.

Two-tailed t-tests for independent samples assuming unequal variances were proformed

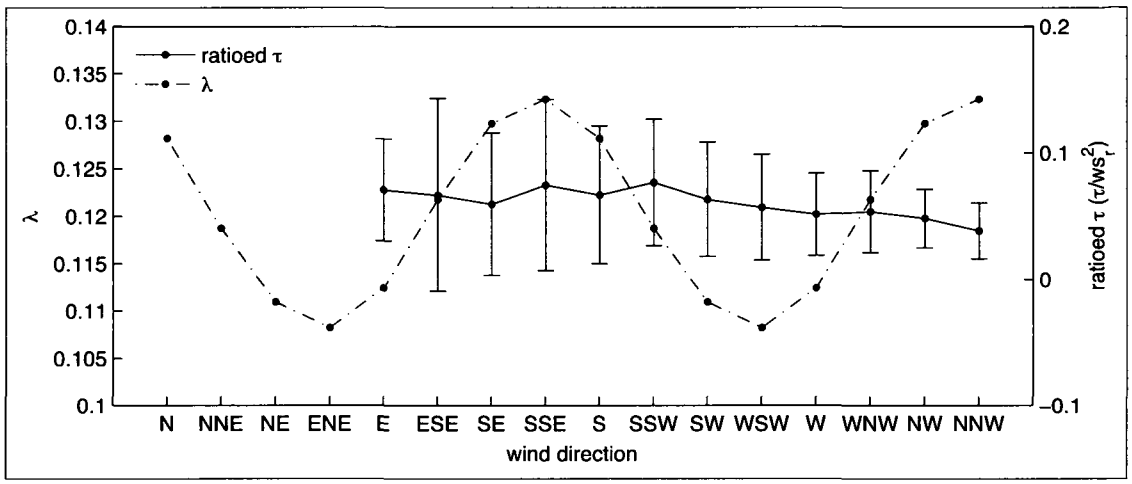

Figure 4.10 Ratioed shear stress, τ/ws_r^2, and site λ values by wind direction.

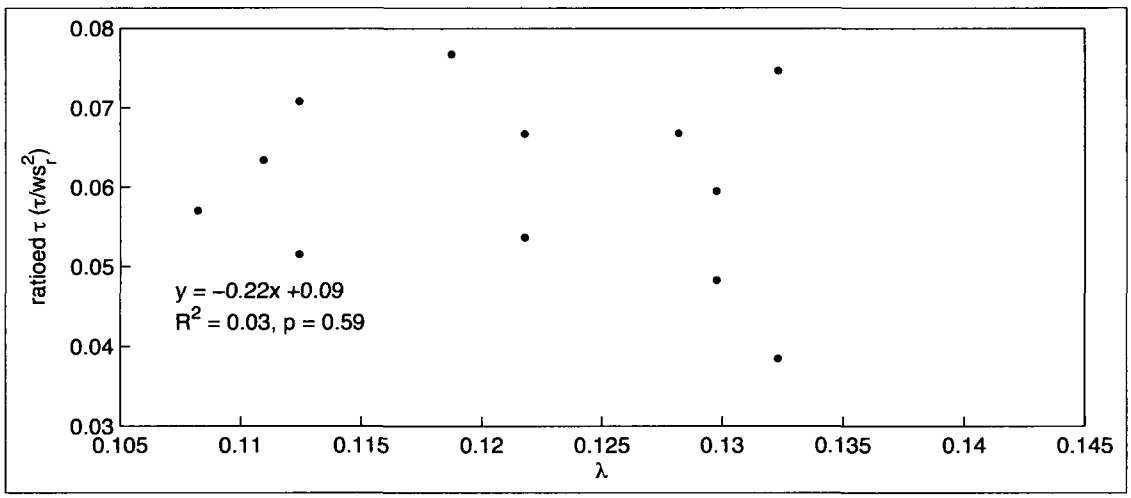

Figure 4.11 Ratioed shear stress, τ/ws_r^2 versus site λ values for the wind directions.

to evaluate if the means of each RSS were significantly different from each other (Table 4.6). t-tests show that in approximately 98% of cases, RSS means are insignificantly different from each other indicating that as λ changes, as a function of wind direction, the mean RSS values remain statistically similar. One significant difference in mean RSS values exists between the SSW and WSW where there is an unexpected decrease in RSS with a decrease in λ. The decrease in the RSS is between λ values that are not significantly different; this unexpected result could be explained by measurement error.

Table 4.6 P values for two-tailed t-tests preformed on the mean RSS for each wind direction. The highlighted value indicates a significant difference at the 95% the significant difference between the means of the SSW and the WSW.

	E	ESE	SE	SSE
ESE	4.41E-01			
SE	9.64E-01	5.02E-01		
SSE	4.41E-01	9.66E-01	5.04E-01	
S	3.69E-01	6.84E-01	4.30E-01	5.54E-01
SSW	4.23E-01	9.68E-01	4.87E-01	9.03E-01
SW	2.98E-01	3.17E-01	3.56E-01	1.30E-01
WSW	2.69E-01	2.09E-01	3.25E-01	6.07E-02
W	4.29E-01	9.14E-01	4.88E-01	8.80E-01
WNW	8.65E-01	5.68E-01	9.05E-01	5.71E-01
NW	4.34E-01	9.19E-01	4.92E-01	8.89E-01
NNW	6.77E-01	7.61E-01	7.24E-01	7.68E-01

	S	SSW	SW	WSW	W	WNW	NW
ESE							
SE							
SSE							
S							
SSW	5.10E-01						
SW	3.05E-01	1.04E-02					
WSW	1.34E-01	1.41E-03	1.64E-01				
W	8.64E-01	9.21E-01	5.78E-01	4.64E-01			
WNW	4.82E-01	5.50E-01	3.94E-01	3.57E-01	5.50E-01		
NW	8.74E-01	9.28E-01	6.12E-01	5.05E-01	1.00E+00	5.55E-01	
NNW	6.52E-01	7.43E-01	5.33E-01	4.82E-01	7.31E-01	8.10E-01	7.36E-01

Threshold RSS was estimated in a similar manner to the threshold regional wind speed. A distribution of the RSS values from the Irwin sensors when saltation activity was detected is displayed in Fig. 4.12. Figure 4.12 shows a sharp increase in RSS values at 0.03 and 0.04, indicating that there is a sharp increase in the amount of saltation that is occurring at the site. This range of values signifies the RSS threshold for the site.

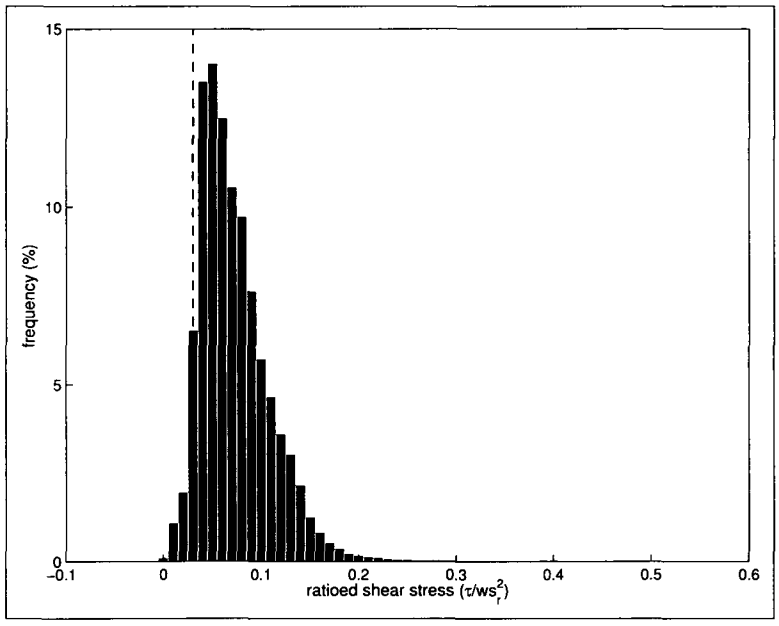

Figure 4.12 Distribution of the RSS values when saltation activity was occurring at the study site. The dashed line indicates the estimated saltation threshold.

The means of RSS were not distinguishable from each other and hence there is no observable trend in these data when plotted against λ. One factor that may be biasing the results is the number of malfunctioning sensors when wind was blowing from the southeasterly directions, as seen in Table 4.7. All the winds from the southeast and northwesterly directions had malfunctioning Irwin sensors that could be biasing the mean values for these directions. To aid in the interpretation of the RSS results histograms of these RSS data were created.

Histograms and maps of these RSS data show that there were differences in the frequency and locations of RSS when wind comes from different directions. Figures 4.13 and 4.14 show

Table 4.7 Number of Irwin sensors missing from the calculation of shear stress values by wind direction.

Direction	# of missing Irwin sensors
E	7
ESE	7
SE	7
SSE	7
S	1
SSW	0
SW	0
WSW	0
W	0
WNW	1
NW	3
NNW	7

histograms of these RSS data for each wind direction. Within each histogram the following values are displayed: mean, standard deviation, coefficient of variation, maximum, skewness, and kurtosis. Figure 4.9 indicates the magnitude of the near surface RSS by the size of the grey circles at each of the mini-tower locations for the SE and SW directions.

The histograms of RSS for each of the wind directions all exhibit a positive skewness that is expected because wind speed and hence shear stress values typically follow a Gumbel or Weibull distribution (Schönfeld, 2003). The RSS histograms show that the winds from the southeasterly directions had high values of skewness, which are attributed to the large number of missing Irwin sensors in these directions, shown in Table 4.7. Histograms in the ESE, SE, SSE, all have relatively high coefficients of variation indicating high variability within these data, which was due to some high values of RSS such as those seen at sensors 6 and 7 and 21 in Fig. 4.9. The high values of skewness in these directions were also driven by the few number of high RSS values from the identified high RSS locations.

RSS histograms for the SSW, SW and WSW also show positive skewness values, displayed in Figs. 4.13 and 4.14. However, the positive skewness in these directions can be

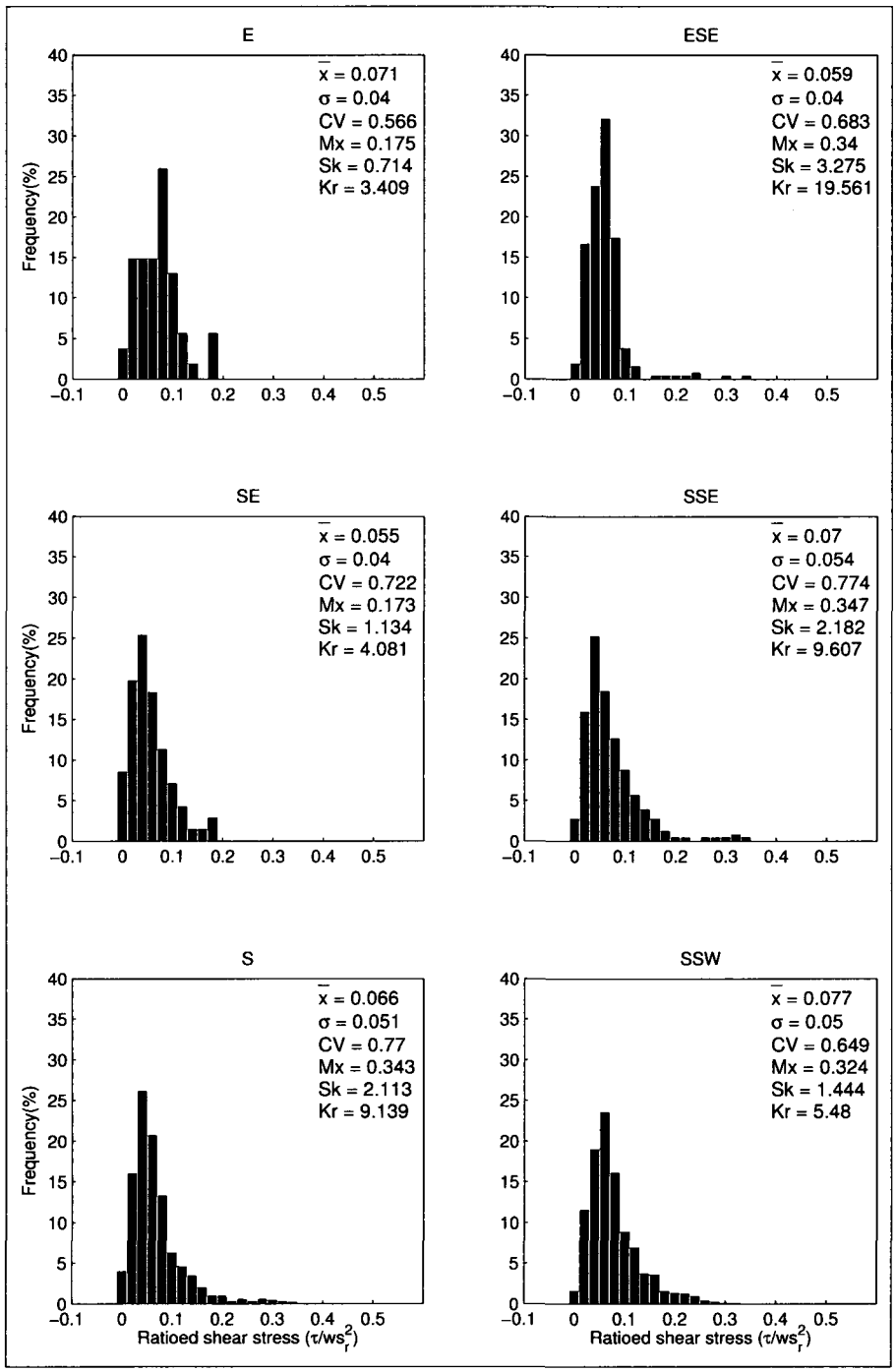

Figure 4.13 Histograms for ratioed surface shear stress for the E to SSW wind directions.

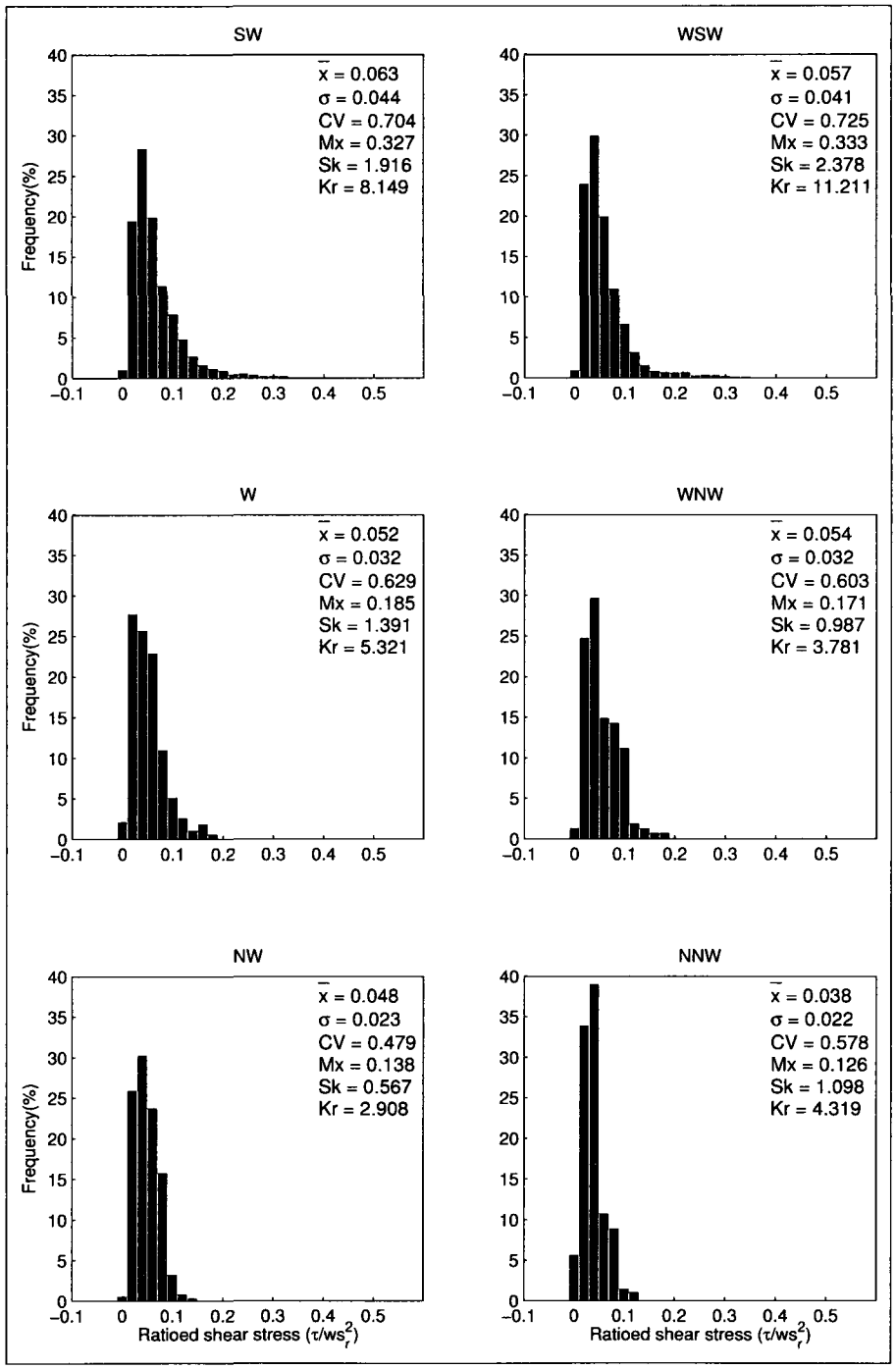

Figure 4.14 Histograms for ratioed surface shear stress for the SW to NNW wind directions.

attributed to very high RSS values at sensors 3, 6, 7, 21 and 28 in Fig 4.9B. The positive skewness in the histograms in the SW can be attributed to a larger number of sensors with greater shear stresses than in the SE, which is evident when comparing A and B of Fig. 4.9. King et al. (2006) argue that positive skewness is important for the initiation of sediment transport. In this study the skewness values in the southwesterly directions can be attributed to a more widespread distribution of sensors with high RSS values; whereas, the high skewness in the southeasterly directions can be attributed to just a small number of sensors with high RSS values. The greater distribution of sensors with high RSS values in the southwesterly directions is due to the the lower λ values in these directions, which are likely a result of mesquite street alignment (Gillette et al., 2006).

When analyzing the histograms with the aid of the RSS maps these data show that there is a greater frequency of locations with high RSS values from wind directions with low λs and that mean RSS values from directions with high λ values may not be representative of the stresses at the site because of the number of malfunctioning Irwin sensors.

4.4.1 The Raupach et al. (1993) shear stress partitioning model

These data from the Irwin sensors were used to evaluate how the Raupach et al. (1993) shear stress partition model fits within the context of the nabkha dunes. The value of R was calculated using Eq. 2.8 with average shear stress measurements over the nabkha site and shear stress measurements made a kilometre upwind of the site on an open playa. Displayed in Fig 4.15 is the value of R which was calculated by using Eq. 2.8 equalling 0.366, for the average λ of 0.122. There were a limited number of data points available to make calculations of R and hence one average value was calculated. The value of R is higher then expected, but still lies within the range of results from other shear stress partitioning experiments.

Table 4.8 BSNE data for each storm event over the study period.

Storm #	1	2	3	4	5	6	7	8	9	10	11	12	13	
Mean Dir	SW	WSW	W	SW	WSW	SW	SSW	SSE	SW	NW	SSW	SSW	SW	$\overline{Q}$
BSNE-Safire #														
1	6.47e-05	1.67e-04	1.85e-04	2.05e-04	1.80e-04	4.10e-04	-	2.29e-05	2.76e-05	1.05e-04	6.12e-05	3.01e-04	8.99e-05	1.52E-04
8	9.48e-05	6.11e-04	6.38e-04	3.24e-04	5.66e-04	1.00e-03	-	2.48e-05	8.89e-05	-	1.98e-04	3.04e-04	3.28e-04	3.80E-04
11	1.60e-05	1.98e-04	1.70e-04	6.94e-05	1.01e-04	2.42e-04	-	3.40e-06	2.03e-05	-	4.50e-05	6.99e-05	4.13e-05	8.88E-05
17	1.90e-05	1.43e-04	1.32e-04	5.68e-05	9.84e-05	2.44e-04	-	-	1.88e-05	-	4.17e-05	3.82e-05	4.92e-05	8.41E-05
21	9.38e-05	1.87e-04	2.45e-04	3.09e-04	1.87e-04	5.69e-04	-	7.78e-05	3.73e-05	3.65e-04	8.29e-05	5.85e-04	1.56e-04	2.41E-04
24	2.58e-05	1.14e-04	1.29e-04	1.20e-04	1.08e-04	2.49e-04	-	1.19e-05	1.60e-05	8.60e-06	3.56e-05	1.50e-04	6.81e-05	8.63E-05
23	4.04e-05	5.30e-04	7.69e-04	4.03e-04	7.79e-04	1.21e-03	-	8.03e-06	1.34e-04	2.40e-05	2.97e-04	2.76e-04	3.41e-04	4.01E-04
28	7.13e-05	3.38e-04	5.64e-04	5.22e-04	5.40e-04	9.76e-04	-	3.86e-05	7.87e-05	7.42e-06	1.75e-04	4.20e-04	2.17e-04	3.29E-04
31	1.28e-04	9.81e-04	1.49e-03	5.73e-04	1.51e-03	1.57e-03	-	9.69e-06	1.87e-04	4.21e-05	4.15e-04	3.08e-04	5.30e-04	6.45E-04
33	1.33e-04	2.76e-04	4.15e-04	4.60e-04	3.85e-04	9.02e-04	-	4.17e-05	9.19e-05	7.24e-06	2.04e-04	5.58e-04	2.59e-04	3.11E-04
$\overline{Q}$	6.86e-05	3.54e-04	4.73e-04	3.04e-04	4.45e-04	7.38e-04	-	2.66e-05	7.00e-05	7.99e-05	1.56e-04	3.01e-04	2.08e-04	2.69E-04
$\overline{u}$(m/s)	9.7	10.3	11.2	11.2	11.8	11.2	7.9	7.0	9.7	9.3	8.7	10.9	10.3	

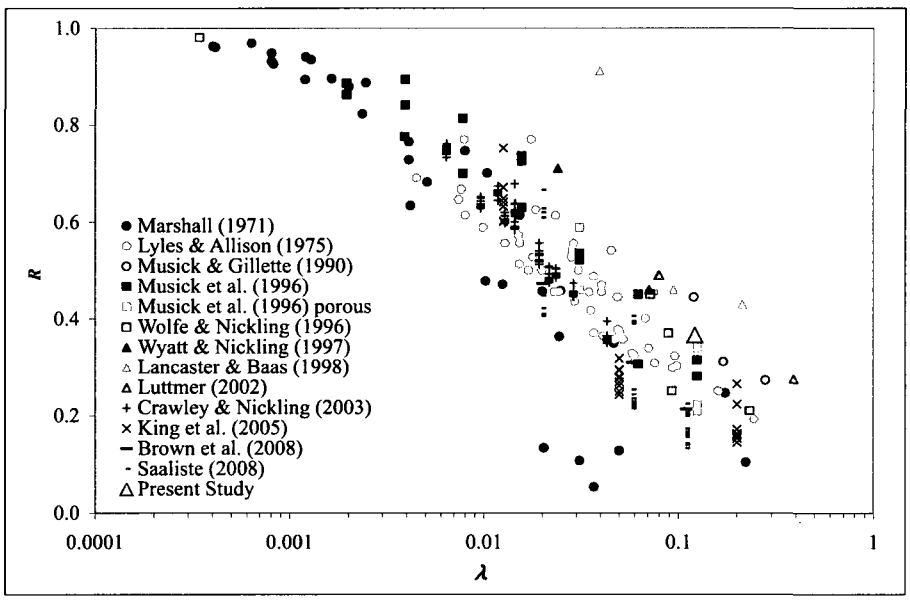

Figure 4.15 Shear stress partitioning ratio, R, versus roughness density, λ, for a number of shear stress partitioning studies, modified from Saaliste (2008).

4.5 SALTATION FLUX

Table 4.8 displays the mean flux values from each BSNE for each storm event. These data show that the three areas with the highest average flux are BSNE locations 31, 23 and 8, which are in the southern half of the study site. The areas of the lowest average flux are at BSNE locations 17, 24 and 11, which are in the northern half of the study site; this pattern is thought to relate to the availability of mobile sediment on the site. The southwestern half of the site had the most mobile sand available and the northern part of the study site had less mobile sand available because the surface was mostly crusted. Table 4.8 also displays the mean wind direction for each storm event and shows that most transport was from the southwesterly wind directions.

These BSNE data show how saltation flux can change as the wind direction changes. The BSNE at Safire 31 has the highest saltation flux values in 7 of the 13 storms, all when winds were from the southwesterly wind directions. These high flux values result from the BSNE being in an area with high availability of mobile sediment, and also being relatively

exposed at the end of a corridor seen in the maps of Fig. 4.16. This corridor created a long upwind fetch area that allowed for increased saltation activity to occur because the larger upwind area allows for greater sediment availability. During storm 8 when winds were flowing from the SSE this BSNE (number 31) measured the third lowest saltation flux value ($9.69e^{-06}$g·cm^{-1}·s^{-1}), shown in Table 4.8. This contrasts to the high flux values measured when winds are from the southwesterly winds directions. The low flux value at this location when the wind was from the SSE is due to upwind sheltering from a dune. Table 4.8 also shows that during storm 8 the BSNE at location 21 measured the highest value of saltation flux ($7.78e^{-05}$g·cm^{-1}·s^{-1}) because it was in line with a long fetch area associated with this wind direction, making it very exposed. At location 21, when winds were blowing from other directions this BSNE was relatively sheltered and experienced lower values of flux compared to the other BSNE locations, shown in Table 4.8. These two examples show how saltation flux can change at a location based on wind direction and sheltering.

The examples above demonstrate that fetch length plays a role in the flux at a given location. The BSNEs at safires 11 and 17 both have short fetches upwind of them when winds are from the southwesterly directions because of nabkha sheltering, seen in Fig. 4.16. Table 4.8 shows that in storms 1, 4, 5, 6, 12, 13 these two BSNEs have the lowest measured flux because of the upwind sheltering from nabkhs that decrease the fetch distance, which affects the sediment availability. These locations also have lower measured flux because of the development of a partial crust reducing the available sediment.

The values of saltation flux from the Safires give an indication of how much sediment is moving. The values generated for the analysis are supplementary to the values of wind speed and shear stress. The Safire data were only used as an indication of sediment movement trends, and not absolute values because the saltation activity recorded by the Safires was highly intermittent, with γ values ranging from 1.17e-2 in the W to 6.93e-6 in the E as shown in Fig 4.17. The comparisons between the BSNEs show that there is a positive relationship, with some agreement, between increasing saltation flux measured by the BSNEs and Safire output, seen in Fig. 3.9.

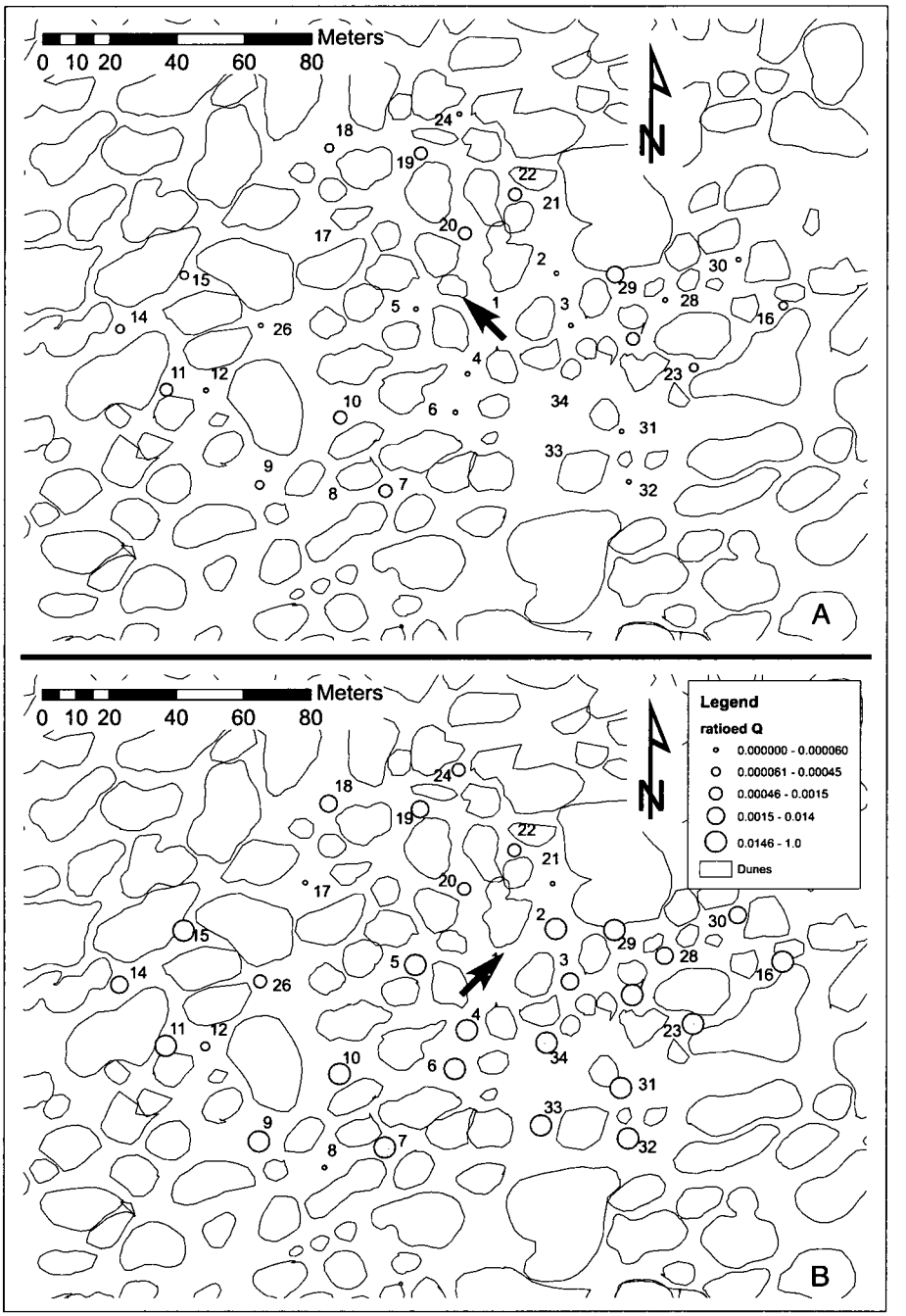

Figure 4.16 Ratioed saltation flux data, Q/Q_{mx}, for SE (A) and SW(B). The size of the grey circles represents the magnitude of the ratioed saltation flux, as outlined in the map legend. The black arrow in the center of the map indicates the regional wind flow direction.

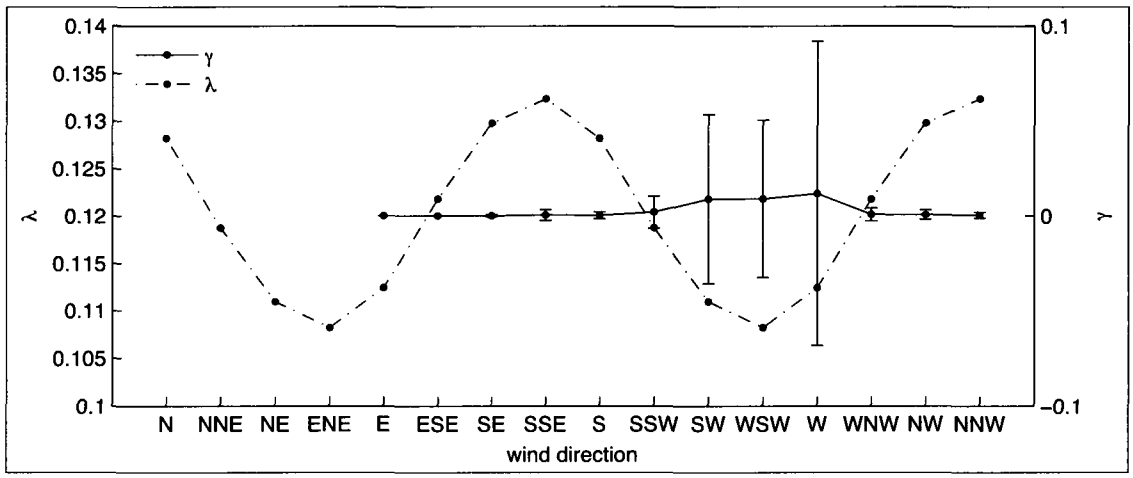

Figure 4.17 Saltation intermittency, γ, and site λ values by wind direction. Saltation data were only available for 11 of the wind directions, however as the λ values decreased there is an increase in the γ values, the solid line.

Ratioed saltation flux values, Q/Q_{mx}, from the Safires show how much saltation is occurring at each sensor for each wind direction. Saltation flux values were ratioed to the maximum saltation flux value recorded at the site over the study period. The ratio allows for comparison of values between wind direction. Figure 4.16 displays maps of the ratioed saltation flux values for the SE(A) and SW(B) wind directions; the size of the grey circles represents the magnitude of saltation flux. Figure 4.16 shows that regional wind from the SW has greater saltation flux at all of the sensors throughout the study site than wind from the SE. Greater saltation flux from the the SW winds can be attributed to a smaller λ and alignment with the streets. Sensors 11, 19, 20, 22 and 29 showed the highest values of saltation flux with winds from the SE (Fig. 4.16A). Sensors 20 and 29 have high saltation flux values because they are in line with small corridors that align with the southeasterly wind direction. The alignment with the corridors at these locations creates a longer fetch for the wind to generate greater saltation activity. When winds are from the SE, low flux values were measured at sensors 5, 27, and 35. Saltation flux values are low at these locations because they are sheltered by upwind roughness elements stopping sediment movement, seen in Fig 4.16A.

Similar trends of exposed Safires measuring high flux values and sheltered Safires measuring low flux values can also be observed when winds are from the SW. Sensors 8, 12, 17, 20, 21, and 22 show the least saltation flux when winds are from the SW (Fig. 4.16B). Sensors 12, 20, 22 and 24 are all in the lee of roughness elements and hence have lower saltation flux because these areas are sheltered. Figure 4.16B shows that Safires 2 and 10 generated higher saltation flux values because they are at the end of corridors which are very exposed to the SW winds. Higher saltation flux values occur at safires 2 and 10 because there is no sheltering from upwind elements and the corridors create long fetches for greater sediment movement.

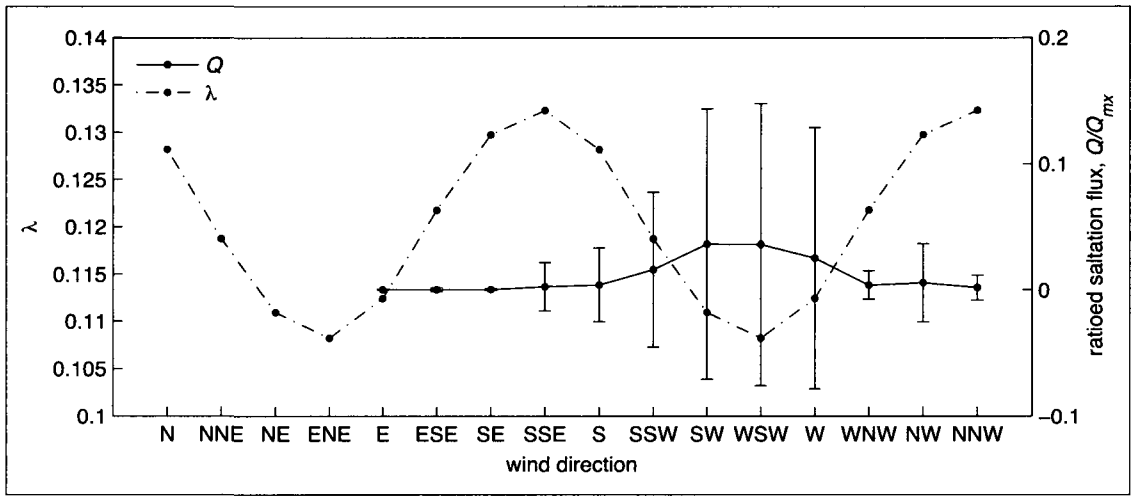

Figure 4.18 Ratioed saltation flux, Q/Q_{mx}, and site λ values by wind direction. Saltation data were only available for 11 of the wind directions; however, as the λ values decreased there is an increase in the saltation flux values, the solid line.

Figure 4.18 displays the mean ratioed saltation flux values for each wind direction on the right axis of the graph; the dashed line displays the λ's for each wind direction. Saltation information was only available for wind directions E to NNW because there was insufficient wind from the N to ENE to initiate saltation. This graph indicates that as λ decreases, there is an increase in the amount of saltation flux observed at the study site. Greater saltation flux was recorded for the winds from the southwesterly direction; whereas, the south, southeasterly, and northwesterly winds did not generate high flux values. Figure

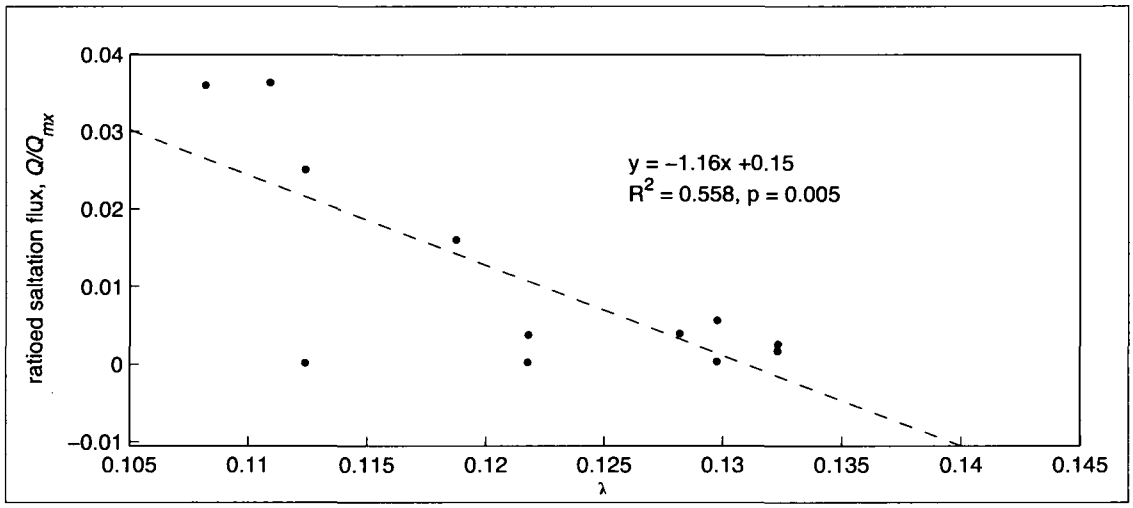

Figure 4.19 Ratioed saltation flux, Q/Q_{mx}, versus site λ values for the wind directions. This significant relationship shows that as the λ values increase the Q, values decrease.

4.19 shows that as λ increases there is a decrease in the Q/Q_{mx}. Although there is scatter in these data, which is evidenced by the low R^2 value, the relationship is significant at the 99% confidence interval. The one major outlier at $\lambda = 0.112$ is for the saltation activity from the E. The low saltation measured at the low λ value is due to relatively low wind speeds and few number of data points contributing to the average, shown in Table 5.1.

4.6 Wind Direction

A and B in Fig. 4.20 show near surface wind direction and standard deviation for the SE and SW wind directions, respectively, when wind speeds were greater then 1 $m{\cdot}s^{-1}$. The near surface standard deviations of wind directions show the variability of winds throughout the roughness elements. These wind direction data can be used to identify various flow patterns. Larger standard deviation of wind directions indicate gusty and variable wind flow. The mean wind direction displayed on the maps can be used to identify areas of steering and show how the nabkhas direct wind flow. These data show areas throughout the field site where wind direction was variable–inferring turbulence and mixing of wind flow. Mini-towers 27 and 35 in Fig. 4.20A are directly in the lee of large nabkhas. At these

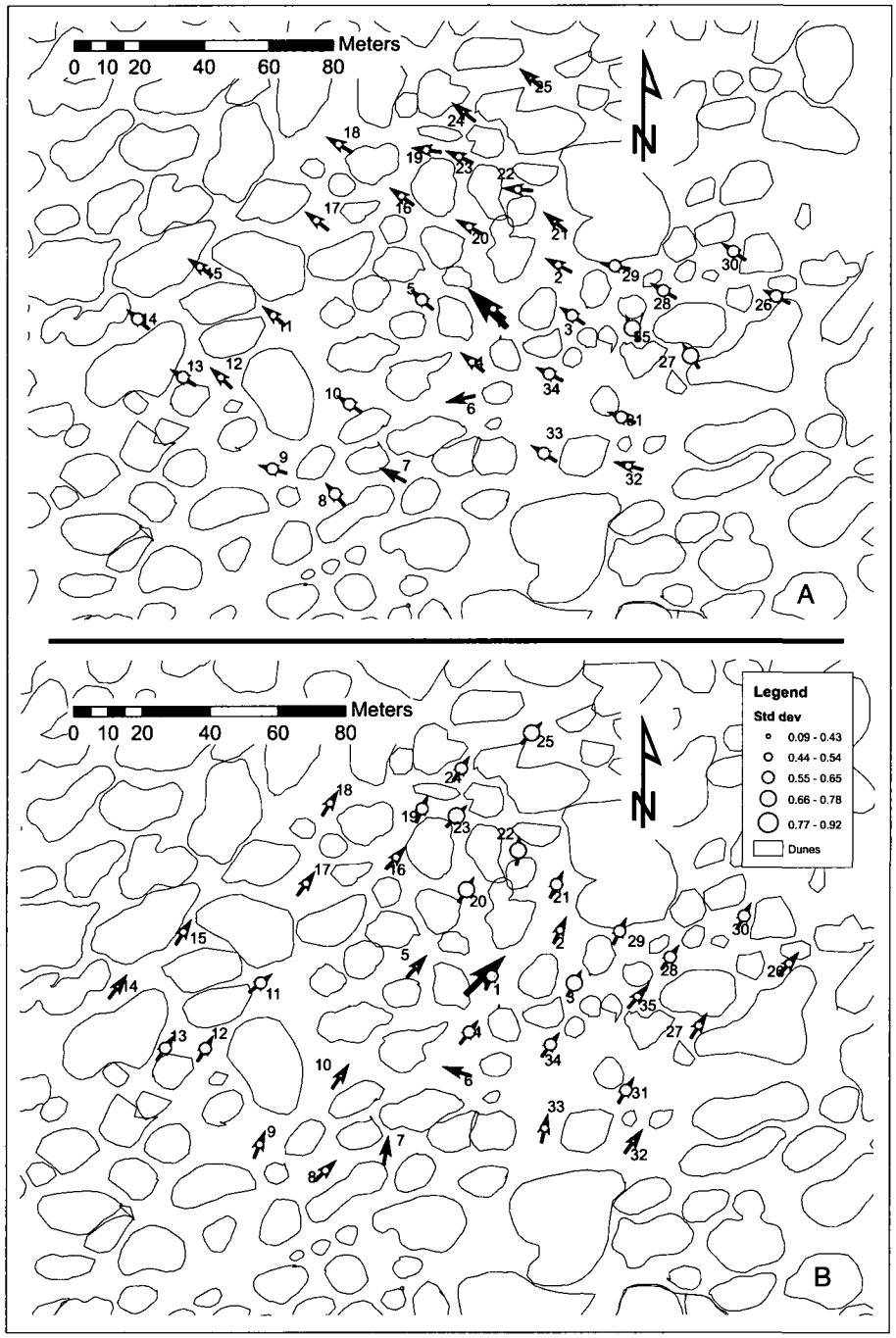

Figure 4.20 Ratioed mean standard deviation of near surface wind direction and mean direction data for the SE(A) and the SW(B). The size of the grey circles represents the magnitude of the standard deviation, as outlined in the map legend. The black arrow in the center of the map indicates the regional wind direction.

locations the standard deviation of the wind direction is high, suggesting that the wind flow in these areas was turbulent and had high variability of direction. Examples of the same type of wind flow can be found at mini-towers 20, 22, and 23 in Fig. 4.20B where the high standard deviation of wind direction suggests turbulence, mixing and variability of the wind flow. In these examples the high variability in wind flow in the lee of the roughness elements suggests dissipation of wind energy and inconsistent wind flow. At these locations RWSs are also low (A and B of Fig. 4.3), which suggests that these nabkhas are sheltering the surface in the lee of the roughness.

Map B in Fig. 4.20 shows examples of winds steering through corridors created by the nabkhas. A corridor that is aligned N-S from towers 2 to 21 shows that the winds from the SW started to veer north at mini-tower 2. At mini-tower 21 the wind direction was steered north, and a high standard deviation indicates variability in the wind direction as the wind veers northwards through this corridor. Figure 4.3B shows that wind speeds are high at mini-tower 2 and decrease at mini-tower 21 indicating that as the wind was steered northwards through this corridor there was a dissipation in the wind energy. The wind direction at mini-tower 16 was in alignment with the upwind corridor. This mini-tower had a low standard deviation implying that the wind was moving straight through this corridor. As the wind travels up this corridor it encounters mini-tower 19, which had some protection directly upwind of it. The arrow at this location shows that the wind flow was steered north but has a high standard deviation in wind direction indicating that the steering is slight and wind direction is changing frequently. Mini-tower 15 in Fig. 4.20B also demonstrates steering of the winds. The large nabkhas surrounding this location were steering the wind in a northerly direction as the wind was forced through a small corridor just north of this mini-tower.

4.7 INTER-NABKHA WIND FIELD

Wind flow, shear stress and sediment movement are complex in a nabkha dune field because of the heterogeneous distribution of the roughness elements. The distribution of these elements has a dynamic effect on the geomorphological forces at work, and hence it is important to understand the context in which these field measurements were made. The maps presented in the previous sections can be used for a detailed discussion of how the wind field behaves as winds encounter the roughness.

4.7.1 Wind direction steering

When wind flowed from the SE, a corridor was created by the dune alignment from mini-towers 3 to 2 to 21 where winds were steered northwards, as shown in in Fig. 4.3A. Figure 4.20A displays the mean wind direction for all the sensors in this direction. Wind direction at sensors 3, 2, and 21 show that the mean wind direction was steered north from the regional wind direction. This steering accounts for the greater RWS at these locations seen as in Fig. 4.3A. At the end of this elongated street there is greater RSS, as shown in Fig. 4.9A, indicating that more stress was reaching the surface as the length of the corridor increases. The RWS at tower 25 also shows a high value and had an uninterrupted stretch of soil directly to the SE where the force of the wind was penetrating down to the surface. Figure 4.20A shows that the mean wind direction for mini-tower 25 was in line with regional wind direction; it also had a very low standard deviation, indicating steady straight flow at this location. Also, at mini-tower 25, the accompanying Irwin sensor measured some of the greatest RSS for that wind direction (Fig. 4.9A). These data provide evidence for the steering of winds, channelization, and acceleration of flow at the near surface.

4.7.2 Sediment transport hot spots

Gillette (1999) describes hot spots as areas over a surface, on a large geographic scale, that are subject to greater sediment transport because of heterogeneous surface characteris-

tics. In this study, the surface displays hot spots, but on a smaller scale. The maps display that there is heterogeneity in the distribution of RSS, RWS and saltation flux when the wind encounters the roughness. The heterogeneity results in some areas being hot spots for sediment transport. A good example of a hot spot is at Irwin sensor 13 in Fig. 4.9B–winds from the SW created high RSS values that were also associated with high ratioed Q values (Fig. 4.16B) and high RWS values (Fig. 4.3B). Two other examples show high RWS at mini towers 2 and 10 in Fig 4.3B that were also associated with high values of saltation flux, shown at Safires 2 and 10 in Fig. 4.16B.

Irwin sensor 8 in Fig. 4.9B and Safire 6 and in Fig. 4.16B show a hot spot for sediment transport because this location had high values of RSS and saltation flux values. This location was very exposed when winds blow from the SW, which make it a hot spot. Irwin sensor 13 and Safire 32 also show a hot spot in the same maps. Again, this location is quite exposed when winds blow from the SW.

4.7.3 Sheltering

Generally, the maps show that areas with greater sheltering from upwind nabkhas experience lower RSS, saltation flux, and RWS values. Figure 4.9A shows that Irwin sensor 3 had low RSS because it is sheltered by the upwind nabkha. This location also experienced a high standard deviation in wind direction (Fig. 4.20A) suggesting that the wind direction is highly variable due to the shedding of eddies around upwind nabkhas. Figure 4.16B shows that at this same location the saltation flux was also very low due to sheltering. Figure 4.9B shows that Irwin sensors 22 and 23 are also sheltered by upwind nabkhas displaying low RSS values. Mini-towers 22 and 23, corresponding with Irwin sensors 22 and 23 in the SW (Fig. 4.3B) also show lower wind speeds and high standard deviations in wind direction (Fig. 4.20B). Saltation flux was only measured at location 22, and it was low at this location (Fig. 4.16B). The high standard deviation in wind direction, low RSS and low RWS demonstrate that locations in the lee of nabkhas experience upwind sheltering.

When wind encounterd the nabkhas from directions where the λ values are higher, there

was greater surface protection from the dunes sheltering the surface. Many of the mini-towers in Fig. 4.3A display very low values of RWS, including tower numbers 5, 8, 10, 26, 27, 30, and 35. All of these sensors illustrate that there is greater sheltering from the roughness when wind was coming from the SE. Figure 4.20A displays that the mean wind direction at these locations was in line with the regional wind flow. At these locations the wind directions were associated with high standard deviations, indicating that wind was flowing around the roughness elements disrupting the flow and potential for wind energy to reach the surface. The values of Q for this direction are all lower than what was measured in the other wind directions, shown in Fig. 4.16A suggesting that high λs result in reduced sediment transport.

Wind flow from the SW also has nabkhas sheltering the surface; however, the sheltering is not as widespread from this direction as it is from the SE because of the alignment of the nabkhas and the decreased frontal areas of the dunes. Sheltering existed at mini-tower locations 20, 23, and 25, displayed in Fig. 4.3B. These mini-towers experienced decreased RWS because they were in the lee of roughness elements; they also demonstrated high standard deviations of wind direction, seen in Fig. 4.20B and reduced RSS, seen in Fig. 4.9B.

4.7.4 Changing wind regimes

Contrasting the maps of SE to the maps of SW reveal that the near surface wind field changed as a result of changing regional wind directions. The mini-tower locations 5, 8, 10, 26, 27, 30, and 35 were used to explain the effects of roughness sheltering with SE winds. These locations show a decrease in sheltering when the winds changed direction and λ decreased. In Fig. 4.3B, when winds flow from the SW, mini-tower 5 had an increased RWS when compared to the SE winds at the same location (Fig. 4.3A). The change in the RWS at this location was due to the amount of sheltering from different wind directions. At mini-tower 5 wind from the SW traveled up a corridor; however, SE winds encounter roughness upwind of that location which sheltered that area. Mini-tower 10 is also in

the middle of a street and experienced an increase in RWS when comparing SW winds (Fig. 4.3B) to the SE winds (Fig. 4.3A). The increase in wind speed can be attributed to the wind direction being very steady and in line with the regional wind flow, seen in Fig. 4.20B. This location also experienced a large increase in Q, as the winds were aligning with the direction of this low λ value. Mini-tower locations 8, and 26 also experienced an increase in the RWS, when comparing winds from the SW to the SE. Figure 4.20B shows the alignment of the mean wind directions for these sensors is in line with the regional wind flow. This alignment is the same as the alignment of the corridors that lead up to these locations. The standard deviations of the wind directions were also low (Fig. 4.20B), showing that the winds travelled straight and steadily up these corridors when the wind was in alignment with them. The standard deviation of wind direction at these locations was much larger from the SE (Fig. 4.20A) because the wind was not in alignment with the corridors. The Q at these locations, as shown in Fig. 4.16, also increased considerably when comparing the SE and SW maps. The RSS, in Fig. 4.9B, at mini-tower 10 also increased compared against the RSS with winds from the SE (Fig. 4.9A). Mini-tower locations 27, 30, and 35 also experienced increases in RWS because there were longer open areas where the wind could penetrate down to the surface. Overall, These results demonstrate that street development and frontal area decrease contribute to increased sediment transport as wind direction changes and λ decreases.

4.8 Summary

Overall these data show that the near surface wind flow is affected by how the wind encounters the surface roughness elements. The near surface wind field indicates a highly significant relationship between decreasing values of λ and increasing values of RWS. These results are further substantiated by the measurements of Q/Q_{mx} and γ. The RSS results are more difficult to interpret and require sensor-by-sensor analysis that suggest heterogeneous distributions of stresses on the surface result from the distribution of the surface roughness.

The large number of sensors on the surface and complexity of the interactions between the nabkhas and aeolian processes requires detailed inspection of these data. There are a number of trends that can be observed from these data:

1. The frontal area of the nabkhas is larger in the southeasterly directions and smaller in the southwesterly directions, which changes the amount of surface protection and affects the near surface wind regimes.

2. As λ decreases with changing wind directions there is a significant increase in the average near surface wind speed.

3. Saltation activity is the greatest for wind directions where λ is the lowest.

4. There is greater sheltering of bare surface from wind directions with the highest λ values.

5. As the regional wind speed increases the vegetation becomes less effective at protecting the surface.

6. Careful inspection of the wind direction maps suggests that there is some steering of the winds through corridors created by the distribution of the nabkhas.

A detailed discussion of these results within the context of the literature on the subject is presented in the next chapter.

CHAPTER 5

DISCUSSION

5.1 Inter-nabkha wind field

Examples from the maps provide evidence for the steering of winds, channelization, and acceleration of flow at the near surface within the nabkha field as suggested by Gillette and Pitchford (2004). The steering and channelization of wind flow has been attributed as one of the major drivers for sediment movement in the mesquite nabkhas (Gillette and Pitchford, 2004; Okin, 2005; Li et al., 2007).

Hot spots for wind erosion have been described by Gillette (1999) as small areas (relative to the size of deserts) that contribute to dust emissions globally. The hot spots arise as a result of surface heterogeneity over a large area, such as areas with low surface roughness, a lack of crust development, or low soil moisture. Hot spots have been used in wind erosion modelling on regional and global scales (Gillette and Pitchford, 2004; Okin, 2005). Work by Saaliste (2008) presents results to suggest that hot spots can exist on a small scale throughout heterogeneous distributions of roughness. Throughout the nabkha dunes hot spots can be identified as areas that experience high shear stress, high wind speeds and increased sediment transport. The hot spots at Irwin sensors 13 and 8 showed high flux (Fig. 4.16B) and high RWS values (Fig. 4.3B). These areas were more exposed when in a street that is aligned with the regional wind direction. The results from this study agree with Gillette (1999) who originally proposed that hot spots will exist in areas with long fetches encountering little interference from surface roughness.

Most wind erosion models assume that the distribution of the surface roughness is homogeneous (Okin and Gillette, 2001; Okin, 2008), therefore assuming equal distribution of the wind forces. The results of this study show that the patterns of near surface wind flow are heterogeneous and dependent on the surrounding nabkhas. For example, Fig. 4.3B

shows that as the wind blows from the SW, RWSs were lower at locations 20, 22 and 25 than other areas on the surface because these areas were less exposed. The accompanying Irwin sensors 22 and 25 (Fig. 4.9) showed very low RSSs as well. In the same maps the RWS and RSS at location 7 was very high because this area was in a corridor aligned with the wind direction. The heterogeneity in the surface roughness allows for some areas to be more exposed than others. These observations demonstrate that nabkhas with heterogeneous distribution of roughness also display heterogeneity in near surface stresses. The hot spot areas all seem to be in locations that are exposed or were in elongated mesquite streets with no roughness interfering with the wind flow upwind of measurement areas. Winds will create uneven erosion patterns at a scale of a few metres in large heterogeneous roughness distributions. Gillette (1999) and Okin (2005) describe hot spot areas on a scale of 10s of meters; however, detailed measurements throughout the nabkha dune field in this study show that hot spots may exist on even smaller scales.

The hot spots identified in this study agree with findings of shear stress partitioning experiments that have demonstrated heterogeneity in the near surface wind field (Mulhern and Finnigan, 1978; Raupach et al., 1993; Crawley and Nickling, 2003; King et al., 2006; Saaliste, 2008). This study and previous ones (e.g., Brown et al., 2008; Saaliste, 2008) have not found there to be a significant difference in the surface shear stress when results are averaged over an entire surface. Previous research examining the long-term sediment movement patterns (Gillette and Pitchford, 2004; Li et al., 2007) in mesquite nabkhas is supported with the results of this study where hot spots are important sources of sediment movement.

The maps and accompanying results show that there were a number of highly sheltered areas. Sheltering by roughness has long been attributed as a dominant mechanism for reducing wind shear stress and sediment transport of the surface (Marshall, 1971; Raupach et al., 1993; Okin, 2008). The degree of sheltering is related directly to λ. The results in this study show that RWS values decrease with increasing λ, which can be attributed to an increase in sheltering. Winds from the SE created heavily sheltered areas, supported by

these data from mini-tower locations 5, 8, 10, 26, 27, 30, and 35 in Fig. 4.3A, as opposed to wind from the SW, because of the high λ values. Fewer sheltered areas exist for the SW winds (e.g., mini tower locations 20, 22 and 25 in Fig. 4.3B), associated with a low λ value, suggesting that there is greater sheltering of the surface when λ values are higher.

Sheltered regions within the dune field were associated with high standard deviation in wind direction (e.g., mini towers 5, 8, 10, 26, 27, 30 and 35 in Fig. 4.20A and 20, 22, and 25 in Fig. 4.20B), low RSS (e.g., Irwin sensors 20 in Fig. 4.9A and 20, and 25 in Fig. 4.9B) and low RWS (e.g., mini towers 5, 8, 10, 26, 27, 30 and 35 in Fig. 4.20A and 20, 22, and 25 in Fig. 4.20B), which suggests that the variation in wind direction was associated with dissipation of the wind energy. The high standard deviations of wind direction indicate that sensors were in an area of flow separation associated with variations in wind direction and a dissipation of wind energy. The measurements made at the sheltered locations support similar measurements made by Gillette et al. (2006) showing that areas in the lee of the large nabkhas experience lower wind speeds, associated with the steering of winds around the dunes, which create sheltered zones. The high standard deviations of wind direction likely result from the shedding of eddies behind the roughness elements that have been conceptualized by Wolfe and Nickling (1993) (Fig. 2.5) and observed by Sutton and McKenna Neuman (2008).

The sheltered and hot spots described in the results were exposed to the same regional winds, but the results show how near surface wind flow can be heterogeneous throughout roughness. Irwin sensor 7 in Fig. 4.9B has a high RSS value, an accompanying high RWS value (Fig. 4.3B) and high saltation flux (Fig. 4.16B) because it is in alignment with a corridor created by the nabkhas. Irwin sensor 22 in Fig. 4.9B shows low RSS and the accompanying RWS (Fig. 4.3b) and flux (Fig. 4.16B) values were also low when compared to other areas on the map. This area was very sheltered by the nabkhas. These results show that over this heterogeneous surface there were areas that experience greater sediment transport processes because of the roughness distribution.

The results also demonstrate that as the wind direction changes, the decreases in λ, as-

sociated with street development and decreases in frontal area, are contributing to increased sediment transport. The RWSs at mini-tower locations 5, 8, 10, 26, 27, 30, and 35 were used to explain the effects of roughness sheltering with SE winds (Fig. 4.3A). When winds blew from SW all these locations experienced increases in RWS because of the alignment of the nabkha dunes with the winds, as seen in Fig. 4.3B. King et al. (2006) found that over a mature nabkha dune field the aerodynamic roughness length (Z_0) increased as the wind direction diverged from the alignment with the streets, suggesting greater sheltering of the surface and an upward displacement of the vertical wind profile. The results of this study agree with King et al.'s (2006) measurements demonstrating that sheltering changes as wind direction changes. These results also agree with the modelled results of Bowker et al. (2007) who showed that wind flow in alignment with streets resulted in increased sediment flux and higher near surface winds. The results also agree with Gillette et al. (2006) showing that areas in the lee of dunes have reduced near surface wind speeds and sediment transport.

5.2 Vegetation and surface roughness

In this study λ was calculated for each of the 16 cardinal wind directions, to quantify the surface roughness along a given wind direction. Within the context of wind erosion, research in the past has focused on calculating *one* value of λ for a surface, because the research has been conducted with unidirectional winds or has been in conducted wind tunnels (Marshall, 1971; Raupach et al., 1980, 1993; Musick et al., 1996; Wolfe and Nickling, 1996; Lancaster and Baas, 1998; Wyatt and Nickling, 1997; Al-Awadhi and Willetts, 1999; Crawley and Nickling, 2003; King et al., 2006; Brown et al., 2008; Saaliste, 2008). In this study λ values varied with the average basal width of the dunes that ranged from 11.43 m in the ENE and WSW to 15.43 m in the SSE and NNW. The associated values of λ vary from 0.10 to 0.13. This range of λ is quite small and is at the high end of the values found within the literature that range from 0.00034 to 0.39 (Marshall, 1971; Musick and Gillette, 1990;

Musick et al., 1996; Wolfe and Nickling, 1996; Wyatt and Nickling, 1997; Lancaster and Baas, 1998; Crawley and Nickling, 2003; King et al., 2006; Brown et al., 2008; Saaliste, 2008).

Typically, surface roughness research uses one type of surface roughness element in any given experiment. Wind tunnel roughness elements that have been used are symmetrical and may be: cylinders (e.g., Brown et al., 2008), cubes (e.g., Crawley and Nickling, 2003), simulated cylindrical vegetation (e.g., Musick et al., 1996) or small gravel (e.g., Al-Awadhi and Willetts, 1999). All these elements found within the literature, except for cubes, do not have changing basal widths; they are exactly the same width from every direction. Calculations of λ, in this study, have demonstrated that for a given surface the variation in basal width changes λ based on how the wind encounters the heterogeneous roughness.

Results of this study show that changing basal width of the surface roughness changes the near surface wind flow. Some research has focused on arrangement of roughness elements on the surface (Marshall, 1971; Raupach et al., 2006; Brown et al., 2008; Saaliste, 2008), and have found that arrangement of surface roughness has little effect changing the surface protection. Within the natural environment roughness varies in size and shape. A surface with a heterogeneous arrangement of homogeneous roughness elements may not experience significantly different stresses (Saaliste, 2008). However, the surface in this study has a heterogeneous arrangement of heterogeneous roughness elements and exhibits changing values of λ depending on how the wind encounters the nabkhas. These changes in λ ultimately result in changes in near surface wind flow exemplified by the significant variations in RWS, changes in RSS, and near surface wind direction at each of the mini-towers.

There are a few obvious streets that are identified in Fig. 4.2. Streets can be identified in a number of directions, but generally the streets are all in the SW-NE direction. The lower values of λ in the SW and NE directions reflect the presence of streets. These visual interpretations, and calculations of λ agree with the results of Okin and Gillette (2001). Okin and Gillette (2001) demonstrated that streets exist along these same azimuth directions; however, a variety of methods used to determine the azimuth direction in their

study showed different results, with general agreement that the streets align in a SW-NE direction.

A vegetative optical porosity component was used in this study for the calculation of the λ. The values of porosity give some indication of the structure of the plant. Porous elements have greater drag coefficients and are capable of extracting more momentum from the air than non-porous elements (Gillies et al., 2002). The value of optical porosity in this study (0.171) is less than what is reported in a studies by Grant and Nickling (1998) (values of 0.19-0.40) by Gillies et al. (2002)(values of 0.42 - 0.53) and Wyatt and Nickling (1997) (values 0.41 and 0.56). However, the value of optical porosity in this study is within the range of those reported for greasewood shrubs by Gillies et al. (2000) (0.15 - 0.30). The low values of optical porosity found in this experiment are due to the large size of the vegetation. The girth of the plants and the thickness of the growth do not allow much light to penetrate through the plant structure. The field measurements of optical porosity were taken while the vegetation was still dormant, and buds were just beginning to show at the very end of the field season. When in full leaf the mesquite would have much lower optical porosity. This may result in more momentum extraction because porous elements have greater momentum extraction than non-porous ones (Taylor, 1988; Wyatt and Nickling, 1997; Grant and Nickling, 1998; Gillies et al., 2000, 2002).

5.3 Ratioed wind speed

Although scatter is evident in the relationship between RWS and λ it shows that as λ increases there is a predictable decrease in the near surface wind speed. In all but one case when the λ values are significantly different there are significant differences in RWS that are expected; that is, lower λ values have higher RWSs and higher λ values have lower RWSs. The one exception is an unexpected increase in RWS with a significant decrease in λ between the N and the WSW. This may result from the relatively few number of data points for the RWSs from the North (Table 5.1). The decrease in RWS with the

increase in λ is likely due to increased sheltering over the surface. The flow regime may be a combination of wake interference and skimming flow, with very little isolated roughness flow. This is similar to observations made by Saaliste (2008) in wind tunnel tests with complex heterogeneous distributions of roughness. The increased RWSs with decreased λ are due to the development of streets that decrease the amount of sheltering the roughness can create on the surface.

Table 5.1 Number of data points used in the calculation of RWS, RSS, Q, γ, and wind direction

Direction	RWS	RSS	Q and γ	wind direction
N	512	0	0	512
NNE	132	0	0	132
NE	442	0	0	442
ENE	542	0	0	542
E	569	54	96	569
ESE	908	270	480	908
SE	829	72	128	829
SSE	2364	522	928	2364
S	4515	773	1344	4515
SSW	8805	1324	3147	8805
SW	12858	4133	7957	12858
WSW	11198	3837	7600	11198
W	2211	394	765	2211
WNW	1320	162	261	1320
NW	1547	414	705	1547
NNW	1761	216	348	1761

Wolfe and Nickling (1996) found that over a mesquite-dominated surface increasing regional wind speeds resulted in a decrease in surface protection, and an associated increase in the Raupach et al. (1993) shear stress ratio. This indicates that as the wind speeds increased over the surface the same roughness became less effective at protecting it. Figures 4.6 and 4.7 show that as the threshold for inclusion in the RWS dataset increases the RWSs at the site also increase meaning that there was a disproportionate increase in the RWS relative to the regional winds. This demonstrates that as the regional winds increase the

nabkhas are less effective at reducing sediment transport processes. As the regional wind speeds increase, the bare surface does not change, so the properties of the nabkhas must be changing resulting in the increase of RWSs. The nabkhas are likely experiencing a reduction in their drag coefficients. Gillies et al. (2002) showed that with increasing Reynolds numbers the drag coefficients decreased for some plant types, suggesting that the with increasing wind speeds there was a decrease in the drag created by the plants.

The results of this study support Gillies et al. (2002) observations that showed that increases in wind speed result in changes in the plant's properties. In this study, the increase in RWS with increases in regional wind speed demonstrate that the nabkhas are less effective at protecting the surface, which implies that the drag of the plants is decreasing. The increase in RWS, as regional wind speed increases, could also be due to greater turbulence and shedding of eddies behind and around the nabkhas, reducing the shelter area, which has been shown by Sutton and McKenna Neuman (2008) with solid roughness elements.

5.4 Ratioed shear stress

In §4.7 Irwin sensors 22 and 23 were used to explain sheltered areas and Irwin sensors 13 and 8 to explain exposed areas throughout the nabkhas. These observations support the notion of Gillette's (1999) hot spots for dust emissions. Maps of RSS display hot spot areas that are typically more exposed when in a street that is aligned with the wind direction. The maps also show that areas more sheltered from upwind nabkhas experience lower RSS values. These observed sheltered and exposed areas agree with the work of Saaliste (2008) who suggests that areas of greater stress can exist throughout heterogeneous distributions of roughness because of the distribution of roughness.

Figures 4.13 and 4.14 show that the distribution of the RSS values for the site are all positively skewed, showing that many of RSS values are much greater than the mean; the positive skewness can be attributed to sediment transport. This positive skewness is expected and in agreement with the measurements made by King et al. (2006) and Saaliste

(2008). The positive skewness is a result of shear stresses deviating positively from the mean, which can be attributed to wake and shedding effects from the roughness accelerating turbulent flow around and behind the nabkhas, which results in sediment transport. In a study throughout nabkha dunes King et al. (2006) showed that shear stress values had the highest values of skewness when winds were encountering surfaces with streets. These high values of skewness were attributed to hot spots for sediment transport through the streets that would generate higher emissions of dust and have increased saltation. The highest values of RSS skewness were not observed in directions that had the most streets. When wind was encountering the roughness from directions where there were fewer streets there were higher values of skewness. These unexpectedly high RSS skewness values, presented in Figs. 4.13 and 4.14, for the southeasterly directions result from a small number of sensors with high RSS values (discussed in §4.4). These southeasterly winds only account for a small percentage of the time that wind is blowing, and likely cause very little sediment transport at the site.

Figure 5.1 shows that the distribution of all the RSS values for the site follow a Gumbel distribution, where a small frequency of large events gives a positive skew to the distribution. The dashed line in 5.1 shows the threshold RSS; most of the RSS values used in the analysis were over the threshold RSS, meaning geomorphological processes are occurring. Wolman and Miller (1960) argue that, on average, the high magnitude low frequency events do not drive long-term geomorphological processes because they are so infrequent. These events may cause a lot of geomorphological change when they happen, but because they are so infrequent they are not large contributors to long-term geomorphological change.They also argue that high frequency low magnitude events, such as frequent low wind speeds, do not drive long-term geomorphological change because they do not have the power to do so. It is widely accepted that wind speed distributions follow a Gumbel or Weibull distribution as seen in line 'b' in Fig. 5.2 (Schönfeld, 2003), which is similar to the distribution of these RSS data in this study, seen in Fig. 5.1. Wolman and Miller (1960) explain that large stresses have the capacity to move sediment very quickly, seen in line 'a' of Fig. 5.2.

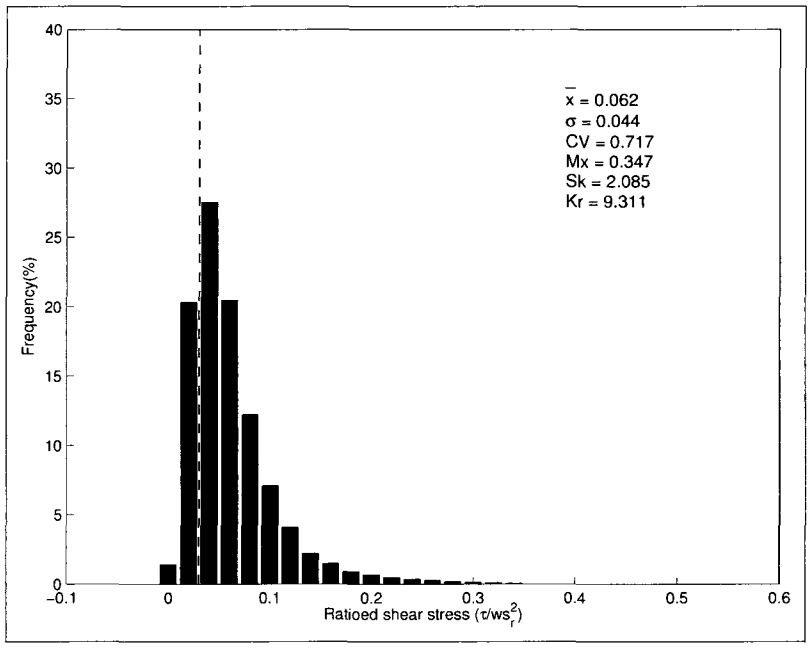

Figure 5.1 Histogram of all the Irwin sensor data from each wind direction bin.

However the product of the frequency of the events and the rate of movement reaches a maximum with stress values slightly larger then the mean. This means that the most work to change the system is done by values that are larger than the mean but not extremely low in frequency. Using the logic presented by Wolman and Miller (1960), most of the work done to drive geomorphological change in this study would be by RSS values slightly larger then the mean, but not at the high extreme.

Careful review of the histograms for each wind direction, in Figs. 4.13 and 4.14, shows that there is a greater frequency of these intermediate RSS values with the wind from the S to WSW. These directions also have lower values of λ associated with them. Although the southwesterly wind directions do not experience the very high and infrequent values of RSS, that create large skewness values, the shear stress from the southwesterly winds is more effective at initiating more consistent sediment transport. The wind directions that exhibit very high values of RSS demonstrate that there may be short bursts of saltation activity, shown in Fig. 4.17; however, the low frequency of these events means that they are not large contributors to sediment transport processes. With lower λ there is more

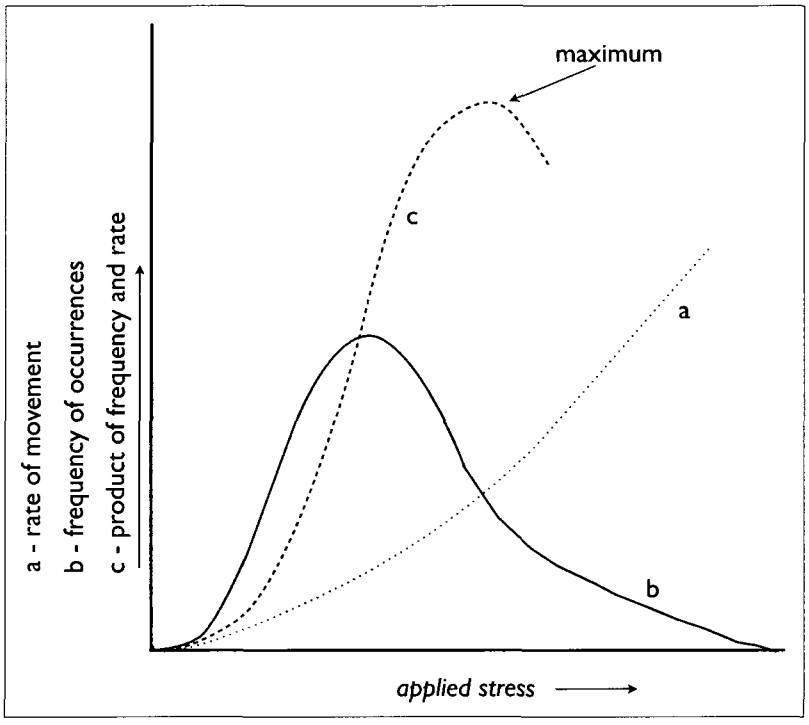

Figure 5.2 Relationship between applied stress, rate of transport, and frequency of stress application, from Wolman and Miller (1960).

consistent shear stress acting on the surface acting to drive sediment transport.

There were some problems with the Irwin sensors in the field, including responses to environmental changes, such as temperature and ambient pressure. The response to environmental conditions was periodic and inconsistent from sensor to sensor and from day to day. These types of problems are not uncommon for these sensors in the field setting; both King et al. (2006) and Gillies et al. (2007) mentioned malfunction of the devices. An example of poor responses from the Irwin sensors are at the base of the regional tower. Irwin sensors 1 and 6 were placed next to each other and should have similar values of RSS; however, they always differ giving some evidence that the values of RSS are unreliable. The sensors seemed to produce better output when the wind speeds where higher, e.g., during wind storm events, and had consistent relative responses when compared against themselves. Hence values from the Irwin sensors were only used when the wind speeds were high enough to output a reliable response.

5.5 THRESHOLD

The threshold wind speed for this site was determined to be between 5 and 6 m/s at 18 m, shown in Fig. 4.8. This threshold range was chosen based on the frequency of Safire counts over the site. The threshold value for this site is low compared to preliminary measurements made by Bowker et al. (2007) who suggested that threshold windspeed at 0.75 m is larger than 5 m/s.

Figs. 4.8 and 4.12 show the threshold wind speed at 18 m and the RSS threshold, respectively. The distribution of Safire counts in both of these figures shows that the saltation is occurring over a range of wind speeds, including very low wind speeds. The results of this study agree with Nickling (1988) and Zhen-shan et al. (2008) who both suggest that saltation threshold will exist over a range of wind speeds and not at a finite value. The range of saltation counts at the lower wind speeds show that saltation activity is still happening over a range of wind speeds. If the threshold for sediment movement was a finite value, Figs. 4.8 and 4.12 would have a very sharp increase in Safire counts at a specific value.

This site has a transport threshold that exists over a range of wind speeds because of surface heterogeneity in the distribution of roughness and the availability of mobile sediment. The heterogeneous distribution of roughness contributes to variations in the threshold depending on how exposed a location is on the surface (Bowker et al., 2007). For instance, wind from the SW, shown in Fig. 4.3B will have a lower threshold at mini-towers 1 and 2 than at mini-tower 20 because mini-tower 20 is much more sheltered. As wind changes direction, regional threshold wind speeds will change at specific locations such as mini-towers 5, 8, 10, 26, 27, 30, and 35 in Fig.4.3. Winds from the SE shelter all of these locations, meaning that the regional wind speed would have to be much higher to initiate sediment movement. However, these locations are exposed when winds blow from the SW and therefore initiation of sediment movement will happen at much lower regional wind speeds. As a consequence of nabkha distribution the threshold wind speeds are immediately tied to

airflow patterns in the near surface.

The range of threshold values is also attributed to the distribution of mobile sediment at the site. The northern half of the site has less mobile sediment available because of desert soil crusting. This is reflected in the BSNE results presented in Table 4.8 where BSNEs at Safires 17, 24, and 11 (shown in Fig. 4.16) consistently have the lowest sediment fluxes. The heterogeneity in the availability of mobile sediment over the surface at the site will contribute to a range of threshold values because areas in the north had surface crusts that increased the sediment threshold (Rice and McEwan, 2001) higher than the threshold in the southern part of the site where sediment was more easily mobilized.

5.6 Saltation flux

Results of these BSNE data showed that the southern half of the study site had much more mobile sediment and higher saltation flux values than the northern half. The results of the BSNEs also showed that there was greater flux of sand in exposed locations that were aligned with streets. However, when winds blew from directions where BSNEs were less exposed there was a decrease in the saltation flux. The BSNE measurements in this study agree well with those of Gillette et al. (2006) and Bowker et al. (2006) showing that the greatest accumulation of sediment occurred at locations that were at the end of long streets, when winds were aligned with them. These results also agree with results of Gillette et al. (2006) and Bowker et al. (2006) who showed that BSNEs in the lee of larger roughness have the least amount of sediment flux because of upwind sheltering.

The results showed that ratioed saltation flux was higher when winds are aligned with streets, which are associated with low λ values. Okin and Gillette (2001) found that the nabkha dunes at the JER align themselves with the dominant SW winds creating mesquite streets. These streets lead to increased sediment transport in the area, particularly when winds are blowing in the southwesterly direction. The channelization of winds through these corridors and the reduction in shelter area are contributing to the increased saltation

flux. Several authors have indicated that the mesquite nabkhas are the most important areas for active sediment movement in the southern part of New Mexico and attribute it to the development of mesquite streets (Okin and Gillette, 2001; Gillette and Pitchford, 2004; Bowker et al., 2006; Li et al., 2007). These RWS and Q/Q_{mx} data in this study help support this, showing that there are faster winds from the southwest that are contributing to greater sediment movement.

The values of γ calculated in this study are low compared to visual observations made during storm events in the field season. The vast majority of saltation intermittency values were less than 0.01, which indicates that saltation was only occurring for 1% of the time during the storm events. These values of saltation intermittency are very low compared to the limited number of studies that have used this parameter. Stout and Zobeck (1997) report values of 0.01 at the lowest range of saltation activity during a storm event. Stout (2004) reports values of intermittency from 0.02 - 0.9 in his field study. Both studies were conducted in a sandy dune field with moderate vegetation cover, allowing for greater sediment movement than what was experienced at this site.

It is assumed that areas of high RWS would also have high RSS values and that these areas would also exhibit higher values of saltation flux and intermittency. This is not always the case, and areas of high RWS may not exhibit high values of flux. In the maps displaying data from the SE, mini-tower 35 has a low RWS, but displays a relatively high value of saltation flux. These discrepancies are not uncommon when reviewing the maps of the near surface activity throughout the site and could be due to a number of issues. The availability of mobile sediment throughout the site was not even, areas to the northwest had a strong crust development, with very little loose sediment. Areas in the eastern part of the study site had loose sediment on the surface that was more easily mobilized. The eastern side of the study site could potentially generate higher saltation flux values more easily than the areas in the northwest with similar shearing forces applied. These discrepancies between the measured saltation flux values and the wind speeds could also be attributed to differences in the sensitivity of the safires themselves, where one Safire may not be activated

as easily by the grains on this site compared to another Safire. Problems of this nature are not uncommon and are discussed in detail by Baas (2003). The discrepancies between the RWS values and the safires could also be attributed to complex interactions between the nabkha dunes and shear stresses, and the distribution of mobile sediment throughout the study site.

5.7 Wind direction

The values of near surface wind direction from this study show how winds move throughout the nabkha dune site. The wind direction standard deviation demonstrates how much the wind directions vary at each location for each wind direction. The results here, coupled with the results of the RWS demonstrate that there is some steering and channelization of the winds through the mesquite streets. Examples from the wind direction maps presented in the results demonstrate that near surface wind directions are influenced by the presence of nabkhas. The maps show that near surface winds do not always flow in the same direction as the regional wind. The maps presented in this study agree with Gillette and Pichford's (2004) argument that as winds encounter roughness they are channelized and steered through the streets. Gillette and Pitchford (2004) demonstrate that saltation activity is increased in street areas as a result of winds being steered and channelized through them, and the saltation flux maps in this study also show this.

5.8 Evaluation of the Raupach shear stress partitioning model

It is well understood that the value of λ for a surface can be used to predict the effects that roughness has on surface shear stresses and sediment flux, because λ is a measure of the roughness on the surface (Gillies et al., 2006). As the size and the density of surface roughness increase there is a decrease in surface shear stress and sediment movement. The range of λ values calculated for this surface were 0.11 - 0.13 and some research would suggest that there would be no sediment movement throughout these dunes based on their shear

stress portioning calculations λ (Wyatt and Nickling, 1997; Lancaster and Baas, 1998). However, sediment movement has been observed and measured in this study and many others conducted at the JER nabkhas (Okin and Gillette, 2001; Gillette and Pitchford, 2004; Li et al., 2007). Okin (2008) would suggest that current predictions for reduction in shear stresses and sediment transport offered by shear stress partitioning models, as in Raupach et al. (1993), overestimate the protective role of mesquite nabkha dunes. Figure 4.15 displays the value of R calculated for this site, equalling 0.366, for an average λ of 0.122.

The value of R calculated for this surface is higher than expected but within the range of calculated values for surfaces with similar λ's. This value is high because it is temporally averaged and is not calculated for the shear stresses at the high tail shear stress distributions. The Raupach et al. (1993) model suggests that R should be calculated for the instantaneous value at the high tail of the shear stress distribution. The value of R may also be high because of error in the measurement devices. A small error in the pressures recorded from the instruments in the field could account for the unexpectedly high value of R. The calculation of R is a ratio of the stresses within the site to the stresses on an open surface a kilometre upwind of the site. The distance between the bare surface and the study site could have resulted in variation in regional wind conditions that may also account for some error in the calculation of R.

Shear stress partitioning results from Musick and Gillette (1990) and Lancaster and Baas (1998) are higher than what is predicted by the Raupach et al. (1993) shear stress partitioning model, suggesting that this model is perhaps not well suited to vegetated environments. Gillies et al. (2000) calculated, using the Raupach et al. (1993) model, that a surface with greasewood vegetative cover would be completely protected from wind forces with a value of λ = 0.032 - 0.06. Lancaster and Baas (1998) suggest that 15% cover is sufficient to completely protect a surface with saltgrass on it. The nabkha dune in this study had 50% roughness cover and λ values ranging 0.11 - 0.13; this site did not see a complete reduction in surface shear stress or saltation activity. Al-Awadhi and Willetts

(1999) showed in a wind tunnel study, with high values of λ (up to 0.36), that saltation activity never stopped when there was a constant upwind supply of sediment. The calculated value of R for this study, in conjunction with these data from the safires, agree with Al-Awadhi and Willetts (1999), showing that at high values of λ there is still the potential for sediment transport.

CHAPTER 6

CONCLUSIONS

The shear stress partitioning approach, championed by the Raupach et al. (1993) model, provides an excellent springboard for generally understanding and describing the effects of surface roughness on surface protection. However, more detailed information is needed to more fully understand and quantify aeolian processes in complex arrays of heterogeneous roughness. This study has aimed to quantify and describe wind flow and sediment transport throughout a nabkha dune field. These nabkha dune fields represent large complex heterogeneous roughness that has been of interest to researchers for a number of years (Okin and Gillette, 2001; Gillette and Pitchford, 2004; King et al., 2006; Bowker et al., 2006, 2007; King et al., 2008). The nabkha dune communities are under investigation because they have developed rapidly over the last century and are attributed to desertification processes (Langford, 2000; Peters et al., 2006). Furthermore they have high vegetative surface coverage that aligns itself with the dominant wind directions contributing to sediment transport processes (Okin and Gillette, 2001; Gillette and Pitchford, 2004). This study generated a high resolution description of aeolian processes throughout these areas. A number of conclusions can be drawn from the research:

1. A surface covered in a complex distribution of heterogeneous roughness in natural settings will have different λ's depending on what direction the wind is encountering the roughness. The change in λ is driven by the changing basal width of the roughness, and if the wind encounters the wide side of roughness elements the λ will be higher, but if it encounters the narrow side of roughness the λ will be lower.

2. On this surface, as the wind direction changed there were differences in the near surface wind field. As λ decreased, associated with different wind directions (for the same surface), there were increases in RWSs. This demonstrates that the near surface wind

field behaves differently when wind encounters the roughness from different directions, which has not been examined before.

3. The maps of these RWS data, RSS, and saltation flux all support the concept that when winds are aligned with mesquite streets there are increased stresses and winds at the surface. Increases in sediment movement can be attributed to these stresses, supporting the findings of Okin and Gillette (2001) and Gillette and Pitchford (2004).

4. When winds are aligned with the mesquite streets increases in sediment transport can be attributed to decreased sheltering by the elements. When winds are encountering the roughness from wind directions with high λ's there is more sheltering of the surface. When wind encounters the roughness from wind directions with low λ's there is less surface sheltering associated with the alignment of the mesquite streets.

5. There is some evidence from the RWS maps and the wind direction maps to suggest that winds are steered through the mesquite streets as wind flows are channelized.

This approach to studying wind flow and sediment transport has shed some light on the near surface aeolian processes throughout complex arrays of heterogeneous roughness elements. The results of this study are largely qualitative; however, they do indicate that complex arrays of surface roughness require more study to better quantify the sediment transport so that wind erosion models can improve and better incorporate surfaces such as nabkha dune fields.

BIBLIOGRAPHY

Al-Awadhi, J. S., Willetts, B. B., 1999. Sand transport and deposition within arrays of non-erodible cylindrical elements. Earth Surface Processes and Landforms 24, 423–435.

Baas, A., 2003. Evaluation of saltation flux impact responders (Safires) for measuring instantaneous aeolian sand transport rates. Geomorphology 59(1-4), 99–118.

Bagnold, R. A., 1941. The physics of blown sand and desert dunes. Dover Publications Inc. Mineola New York.

Bowker, G. E., Gillette, D. A., Bergametti, G., Marticorena, B., 2006. Using QUIC (Quick Urban and Industrial Complex) to model flow patterns in a small area in the northern Chihuahuan desert. Environmental Fluid Mechanics 6 (4), 359–384.

Bowker, G. E., Gillette, D. A., Bergametti, G., Marticorena, B., Heist, D. K., 2007. Sand flux similation at a small scale over heterogeneous mesquite area of the northern Chihuahuan desert. Journal of Applied Meterology and Climatology 46, 1410–1422.

Brown, S., Nickling, W. G., Gillies, J. A., 2008. A wind tunnel examination of shear stress partitioning for an assortment of surface roughness distributions. Journal of Geophysical Research 113 (F02S06), doi:10.1029/2007JF000790.

Chepil, W. S., 1959. Equilibrium of soil grains at the threshold of movement. Soil Science Society Proceedings, 422–428.

Crawley, D. M., Nickling, W. G., 2003. Drag partition for regularly-arrayed rough surfaces. Boundary-Layer Meteorology 107, 445–468.

Davidson-Arnott, R. G. D., Yang, Y., Ollerhead, J., Hesp, P. A., Walker, I. J., 2008. The effects of surface moisture on aeolian sediment transport threshold and mass flux on a beach. Earth Surface Processes and Landforms 33, 55–74.

Deichmann, U., Eklundh, L., 1991. Global digital datasets for land degradation studies: a gis approach. GRID Case Studies Series 4.

Dentener, J. F., Carmichael, G. R., Zhang, Y., Lelieveld, J., Crutzen, P. J., 1996. Role of mineral aerosol as a reactive surface in the global troposphere. Journal of Geophysical Research 101(D17) (22), 22 869–22 890.

Dong, Z., Gao, S., Fryrear, D. W., 2001. Drag coefficients, roughness length and zero-plane displacement height and disturbed by artificial standing vegetation. Journal of Arid Environments 49, 485–505.

Dong, Z., Liu, X., Wang, X., 2002. Wind initiation thresholds of the moistened sands. Geophysical Research Letters 29 (12), 10.1029/2001GL013128.

Fryrear, D. W., Sutherland, P. L., Davis, G., Hardee, G., Dollar, M., 2001. Wind eroison estimates with RWEQ and WEQ. In: Scott, D., Mohtar, R., Steinhardt, G. (Eds.), Sustaining the Global Farm. Purdue University, pp. 760–765.

Gillette, D. A., 1997. Large-scale variability of wind erosion mass flux rates at Owens Lake 2. Role of roughness change, particle limitation, change of threshold friction velocity, and the Owen effect. Journal of Geophysical Research 102 (D22), 25989–25998.

Gillette, D. A., 1999. A qualitative geophysical explanation for "hot spot" dust emitting source regions. Contr. Armos. Phys. 72 (1), 67–77.

Gillette, D. A., Adams, J., Muhs, D., Kihl, R., 1982. Threshold friction velocities and rupture moduli for crusted desert soils for the input of soil particles into air. Journal of Geophysical Research 87 (C11), 9003–9016.

Gillette, D. A., Herbert, G., Stockton, P. H., Owen, P. R., 1996. Causes of the fetch effect in wind erosion. Earth Surface Processes and Landforms 21, 641–659.

Gillette, D. A., Herrick, J. E., Herbert, G. A., 2006. Wind characteristics of mesquite streets in the northern Chihuahan Desert, New Mexico, USA. Environmental Fluid Mechanics 6, 241–275.

Gillette, D. A., Pitchford, A. M., 2004. Sand flux in the northern Chihuahuan Desert, New Mexico, USA, and the infuence of mesquite-dominated landscpes. Journal of Geophysical Research 109 (F04003), doi:10.1029/2003JF000031.

Gillies, J. A., Lancaster, N., Nickling, W. G., Crawley, D. M., 2000. Field determination of drag forces and shear stress partitioning effects for a desert shrub(*Sarcobatus vermiculatus*, greasewood). Journal of Geophysical Research 105 (D20), 24 871– 24 880.

Gillies, J. A., Nickling, W. G., King, J., 2002. Drag coefficients and plant form responce to wind speed in three plant species: Burning bush (*Euonymus alatus*), colorado blue spruce (*Picea pungens* glauca.), and fountain grass (*Pennisetum setaceum*). Journal of Geophysical Research 107 (D24), doi:10.1029/2001JD001259,.

Gillies, J. A., Nickling, W. G., King, J., 2006. Aeolian sediment transport through large patches of roughness in the atmospheric inertial sublayer. Journal of Geophysical Research, Earth Surfaces 111, doi: 10.1029/2005JF000434.

Gillies, J. A., Nickling, W. G., King, J., 2007. Shear stress partitioning in large patches of roughness in the atmospheric intertial sublayer. Boundary Layer Meteorology 122, 367–396.

Grant, P. F., Nickling, 1998. Direct field measurement of the wind drag on vegetation for application to windbreak design adn modelling. Land Degradation and Development 9, 57–66.

Irwin, H. P. A. H., 1981. A simple omnidirectional sensor for wind-tunnel studies of pedestrian-level winds. Journal of Wind Engineering and Industrial Aerodynamics 7 (3), 219 – 239.

Iversen, J. D., Greeley, R., Marshall, J. R., Pollack, J. B., 1987. Aeolian saltation threshold: the effect of density ratio. Sedimentology 34, 699–706.

Jia, Y., Sill, B. L., Reinhold, T. A., 1998. Effects of surface roughness element spacing on boundary-layer velocity profile parameters. Journal of Wind Engineering and Industrial Aerodynamics 73, 215–230.

Johnson, P. R. S., Graham, J. J., 2005. Fine particulate matter national ambient air quality standards: public health impact on populations in the northeastern United States. Environmental Health Perspectives 113 (9), 1140–1147.

King, J., Nickling, W. G., Gillies, J. A., 2005. Representation of vegetation and other nonerodible elements in aeolian shear stress partitioning models for predicting transport threshold. Journal of Geophysical Research 110 (F04015), doi:10.1029/2004JF000281.

King, J., Nickling, W. G., Gillies, J. A., 2006. Aeolian shear stres ratio measurements within mesquite-dominated landscapes of the Chihuahuan Desert, New Mexico, USA. Geomorphology 82, 229–244.

King, J., Nickling, W. G., Gillies, J. A., 2008. Investigations of the law-of-the-wall over sparce roughness elements. Journal of Geophysical Research 113 (F02S07), doi:10.1029/2007JF000804.

Kuylenstierna, J. C. I., Hicks, W. K., Chadwick, M. J., 2002. A perspective on global air pollution problems. Issues in Environmental Science and Technology 17, 21–56.

Lancaster, N., Baas, A., 1998. Influence of vegetation cover on sand transport by wind: field studies at Owens Lake, California. Earth Surface Processes and Landforms 23, 69–82.

Langford, R. P., 2000. Nabkha (coppice dune) fields of south-central New Mexico, USA. Journal of Arid Environments 46, 25–41.

Lee, B. E., Soliman, B. F., 1977. An investigation of the forces on three dimentional bluff bodies in rough wall turbulent boundary layers. Transactions of ASME, Journal of Fluids Engineering, 503–510.

Li, J., Okin, G. S., Alvarez, L., 2007. Quantitative effects of vegetation cover on wind erosion and soil nutrient loss in a desert grassland of southern New Mexico, USA. Biogeochemistry 85, 317–332.

Logie, M., 1982. Influence of roughness elements and soil moisture on the resistance of sand to wind erosion. Catena Suppliment 1, 161–173.

Marshall, J. K., 1971. Drag measurements in roughness arrays of varying density and distribution. Agricultural Meteorology 8, 269–292.

McEwen, I. K., 1993. Bagnold's kink: a physical feature of a wind velocity profile modified by blown sand? Earth Surface Processes and Landforms 18, 145–156.

McKenna Neuman, C., 1998. Particle transport and adjustments of the boundary layer over rough surfaces with an unrestricted, upwind supply of sediment. Geomorphology 25, 1–17.

McKenna Neuman, C., Maxwell, C., 1999. A wind tunnel study of the resilience of three fungal crusts to particle abrasion during aeolian sediment transport. Catena 38, 151–173.

McKenna Neuman, C., Nickling, W. G., 1989. A theoretical wind tunnel investigation on the effect of capillary water on the entrainment of sediment by wind. Canadian Journal of Soil Science 69, 79–96.

Mori, Y., 1986. Evaluation of several 'single-pass' estimators of the mean and standerd deviation of wind direction. Journal of Applied Meteorology 25 (10), 1387–1397.

Morris, H. M., 1955. Flow in rough conduits. Transactions of ASME 120, 373–398.

Mulhern, P. J., Finnigan, J. J., 1978. Turbulent flow over a very rough, random surface. Boundary-Layer Meteorology 15, 109–132.

Musick, H. B., Gillette, D. A., 1990. Field evaluation of relationshipts between vegetation structural parameter and sheltering against wind erosion. Land Degradation and Development 2 (2), 87–94.

Musick, H. B., Trujillo, S. M., Truman, R., 1996. Wind-tunnel modelling of the influence of vegetation structure on saltation threshold. Earth Surface Processes and Landforms 21, 589–605.

Nickling, W. G., 1988. The initiation of particle movement by wind. Sedimentology 35, 499–511.

Nickling, W. G., Ecclestone, M., 1981. The effects of souble salts on the threshold shear velocity of fine sand. Sedimentology 28, 505–510.

Nickling, W. G., McKenna Neuman, C., 1995. Development of deflation lag surfaces. Sedimentology 42, 403–414.

Oke, T., 1987. Boundary Layer Climates. Methuen and Co Ltd Cambridge.

Okin, G. S., 2005. Dependance of wind erosion and dust emission on surface heterogeneity: stochastic modelling. Journal of Geophysical Research 110 (D11208), doi:10.1029/2004JD005288.

Okin, G. S., 2008. A new model of wind eriosion in the presence of vegetation. Journal of Geophysical Research 113 (F02S10), doi:10.1029/2007JF000758.

Okin, G. S., Gillette, D. A., 2001. Distribution of vegetation in wind-dominated landscapes: implications for wind erosion modeling and landscape precesses. Journal of Geophysical Research 106 (D9), 9673–9683.

Okin, G. S., Mahowald, N., Chadwick, O. A., Artaxo, P., 2004. Impact of desert dust on the biogeochemistry of phosphorus in terrestrial ecosystems. Global Biogeochemistry 18 (GB2005), doi:10.1029/2003GB002145.

Peters, D. P. C., Besttelmeyer, B. T., Herrick, J. E., Fedrickson, E. L., Monger, H., Havstad, K., 2006. Disentlangling complex landscapes: new insights into arid and semiarid system dynamics. BioScience 56 (6), 491–501.

Piketh, S. J., Tyson, P. D., Steffen, W., 2000. Aeolian transport from southern Africa and iron fertilization of marine biota in the South Indian Ocean. South African Journal of Science 96 (5), 244–246.

Raupach, M. R., 1989. Applying lagrangan fluid mechanics to infer scalar source distributions from concentration profiles in plant canopies. Agricultural and Forest Meteorology 47, 85–108.

Raupach, M. R., 1992. Drag and drag partition on rough surfaces. Boundary-Layer Meteorology 60(4), 375–395.

Raupach, M. R., Gillette, D. A., Leys, J. F., 1993. The effect of roughness elements on wind erosion threshold. Journal of Geophysical Research 98(D2), 3023–3029.

Raupach, M. R., Huges, D. E., Cleugh, H. A., 2006. Momentum absorption in rough-wall boundary layers with sparse roughness elements in random and clustered distributions. Boundary-Layer Meteorology 120, 201–218.

Raupach, M. R., Thom, A. S., Edwards, I., 1980. A wind-tunnel study of turbulent flow close to regularly arrayed rough surfaces. Boundary-Layer Meteorology 18, 373–397.

Reynolds, J. F., Stafford-Smith, D. M., 2002. Do humans caues deserts? In: Reynolds, J., Stafford-Smith, D. (Eds.), Global Desertification: Do Humans Cause Deserts? Dahlem University Press, pp. 1–21.

Rice, M. A., McEwan, I. K., 2001. Crust strength: a wind tunnel study of the effect of impact by saltating particles on cohesive soil surfaces. Earth Surface Processes and Landforms 26, 721–733.

Saaliste, M., 2008. Spatial variability of surface shear stress on complex, rough surfaces. Master's thesis, University of Guelph.

Schlichting, H., 1936. Experimentelle unterschungn zum rauhigkeitsprolem. Ingr. Arch. 7 (1), 1–34.

Schönfeld, H. J., 2003. Remarks on the definition and the estimation of the aeolian erosion threshold friction velocity. Meteorologische Zeitschrift 12 (3), 137–142.

Stout, J. E., 2004. A method for establishing the critical threshold for aeolian transport in the field. Earth Surface Processes and Landforms 29, 1195–1207.

Stout, J. E., Zobeck, T. M., 1997. Intermittent saltation. Sedimentology 44, 959–970.

Sutton, S. L. F., McKenna Neuman, C., 2008. Sediment entrainment to the lee of roughness elements: effects of vortical structures. Journal of Geophysical Research 113 (F02S09).

Taylor, P. A., 1988. Flow and Transport in the Natural Environment. Springer-Verlag, New York, Ch. Turblent wakes in the atomspheric boundary layer, pp. 270–292.

Véron, S. R., Paruelo, J. M., Oesterheld, M., 2006. Assessing desertification. Journal of Arid Environments 66, 751–763.

Walker, I. J., 2005. Physical and logistical considerations of using ultrasonic anemometers in aeolian sediment transport research. Geomorphology 68, 57–76.

Wolfe, S. A., Nickling, W. G., 1993. The protective role of sparse vegetation in wind erosion. Progress in Physical Geography 17(1), 50–68.

Wolfe, S. A., Nickling, W. G., 1996. Shear stress partitioning in sparsely vegetated desert canopies. Earth Surface Processes and Landforms 21, 607–619.

Wolman, M. G., Miller, J. P., 1960. Magnitude and frequency of forces in geomorphic processses. Journal of Geology 68 (1), 54–74.

Wyatt, V. E., Nickling, W. G., 1997. Drag and shear stress partitioning in sparse desert creosote communities. Canadian Journal of Earth Sciences 34, 1486–1498.

Zhen-shan, L., Xiao-hu, Z., Wen, H., 2008. A stochastic model for initial movement of sand grains by wind. Earth Surface Processes and Landforms 10.1002/esp.1638.